

**A Panel Method Analysis of Flow Past a
Semi-Span Hydrofoil**

by

Christopher Matthew Waaler

B.S., University of Illinois (1987)

Submitted to the Department of Ocean Engineering
in partial fulfillment of the requirements for the degree of

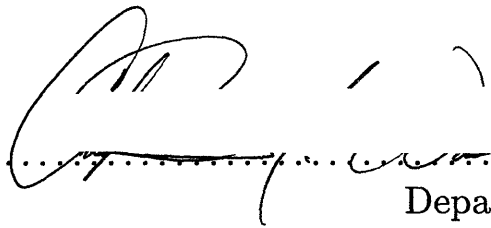
Master of Naval Architecture and Marine Engineering

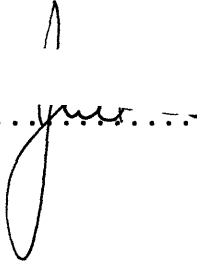
at the

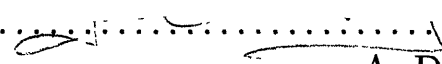
MASSACHUSETTS INSTITUTE OF TECHNOLOGY

February 1995

© Massachusetts Institute of Technology 1995. All rights reserved.

Author 
Department of Ocean Engineering
January 13, 1995

Certified by 
Justin E. Kerwin
Professor of Naval Architecture
Thesis Supervisor

Accepted by 
A. Douglas Carmichael
Chairman, Departmental Committee on Graduate Students

Barber Eng

FEB 13 1995

A Panel Method Analysis of Flow Past a Semi-Span Hydrofoil

by

Christopher Matthew Waaler

Submitted to the Department of Ocean Engineering
on January 13, 1995, in partial fulfillment of the
requirements for the degree of
Master of Naval Architecture and Marine Engineering

Abstract

A low order, perturbation-potential based panel model is modified and applied to the analysis of a semi-span hydrofoil attached to a half body enclosed in a water tunnel. Effects of the body and tunnel walls are included by distributing panels on their surfaces. An iterative wake alignment routine is employed which converges to the steady state wake geometry. The angle of attack of the semi-span hydrofoil and the length of the tunnel walls may be adjusted for comparative studies.

Results from measurements of the tip vortices from a physical model of the same semi-span hydrofoil operating in a uniform flow field are presented. The techniques of laser doppler velocimetry are used to map the vortex structures.

Numerical results of the panel method are shown to be convergent. Comparison is made between the first order approximation produced by the code and the experimental results with favorable agreement.

Thesis Supervisor: Justin E. Kerwin
Title: Professor of Naval Architecture

Acknowledgments

The results of the experiment and the numerical code presented in this thesis are only possible through the diligent efforts of a group of exceptionally talented people with whom I have had the great pleasure to work. Professor Justin Kerwin's knowledgeable and friendly support throughout my graduate studies is very much appreciated. Dr. Spyros Kinnas and Dr. Charles Mazel provided valuable insight to the various difficulties encountered throughout my research. A very warm thank you must go also to all the students of the Propeller Nuts group for their critical, yet encouraging critique of my work throughout the various stages of its completion.

My greatest thanks, however, must go to Dr. David Keenan, who believed in me throughout the numerous highs and lows. Our countless discussions heightened my understanding of fluid dynamics and writing code. Without his constant vigilance and guidance, the final product might never have been attained.

I extend my sincere appreciation to the staff of the Naval ROTC program at MIT. Their flexibility and support made this goal a reality. Thanks also to Professors Alan Brown and Jeff Reed for their constant guidance and support throughout.

Finally, I must express my deepest gratitude to my family, Jack, Virginia, Luke, and Grant, for their continuous support throughout my education and to my fiancée, Elizabeth, for her unceasing encouragement and support during my stay at MIT.

Support for this project was provided by the Office of Naval Research, contract number N00014-89-J-3194, under the supervision of Dr. Arthur M. Reed and with enthusiastic assistance from Ms. Toby J. Ratcliffe.

Contents

1	Introduction	13
2	Mathematical Background	15
2.1	Green's 2 nd Identity and perturbation flow	16
2.1.1	Single Domain	16
2.1.2	Multiple domains	20
2.2	Application to a water tunnel	24
3	Numerical Formulation	26
3.1	Discretization of the Boundary Integral Equation	26
3.2	Foil geometry	30
3.3	Body geometry	31
3.4	Wall geometry	32
3.5	Wake geometry	32
4	Experimentation	38
4.1	Apparatus	39
4.1.1	The water tunnel	39
4.1.2	Laser Doppler Velocimeter	39
4.1.3	Model description	41
4.2	Experimental Procedure	43
4.2.1	Test Conditions	43
4.2.2	Coordinate system	43

4.2.3	Velocity Measurements	44
4.3	Experimental Results	45
5	Calculations	65
5.1	Convergence Studies	65
5.2	Comparison to experimental data	69
6	Conclusions	89
7	Appendix	91

List of Figures

2-1	Basic geometrical relationships for Green's 2 nd Identity	17
2-2	Geometrical relationships for Multi-domain case	21
3-1	Panel arrangement for hydrofoil, $M_r = 6, N_c = 12$	30
3-2	Panel arrangement on foil and body. $N_u = 8, N_b = 8, N_d = 8, M_t = 8,$ $\alpha=10$ degrees	31
3-3	Interpolation scheme for aligning the wake panels	35
3-4	Plan view of wake panelling showing contraction ratio of 30 degrees .	36
4-1	Schematic of tip-vortex experiment data flow	39
4-2	Percent turbulence for LDV and hot-wire measurements in water tunnel	41
4-3	Velocity measurement grids for hydroplane in side configuration . . .	44
4-4	Streamwise velocity of inflow at $\mathbf{X}/\text{Span} = +1.06$. (coarse grid). . . .	46
4-5	Vertical velocity of inflow at $\mathbf{X}/\text{Span} = +1.06$. (coarse grid).	46
4-6	Standard deviation of streamwise velocity of inflow at $\mathbf{X}/\text{Span} = +1.06$. (coarse grid).	47
4-7	Standard deviation of vertical velocity of inflow at $\mathbf{X}/\text{Span} = +1.06$. (coarse grid).	47
4-8	Velocities from vertical traverse of test section at $\mathbf{X}/\text{Span} = +1.06$. (coarse grid).	48
4-9	Velocities from spanwise traverse of test section at $\mathbf{X}/\text{Span} = +1.06$. (coarse grid).	49
4-10	Standard deviations of velocities of vertical traverse of test section at $\mathbf{X}/\text{Span} = +1.06$ mm. (coarse grid).	49

4-11 Streamwise velocity at $X/\text{Span} = -0.044$. Angle of attack is $+5.36$ degrees (side orientation/coarse grid).	50
4-12 Streamwise velocity at $X/\text{Span} = -0.34$. Angle of attack is $+5.36$ degrees (side orientation/coarse grid).	50
4-13 Streamwise velocity at $X/\text{Span} = -0.66$. Angle of attack is $+5.36$ degrees (side orientation/coarse grid).	51
4-14 Streamwise velocity at $X/\text{Span} = -1.28$. Angle of attack is $+5.36$ degrees (side orientation/coarse grid).	51
4-15 Streamwise velocity at $X/\text{Span} = -1.67$. Angle of attack is $+5.36$ degrees (side orientation/coarse grid).	52
4-16 Vertical velocity at $X/\text{Span} = -0.044$. Angle of attack is $+5.36$ degrees (side orientation/coarse grid).	53
4-17 Vertical velocity at $X/\text{Span} = -0.34$. Angle of attack is $+5.36$ degrees (side orientation/coarse grid).	53
4-18 Vertical velocity at $X/\text{Span} = -0.66$. Angle of attack is $+5.36$ degrees (side orientation/coarse grid).	54
4-19 Vertical velocity at $X/\text{Span} = -1.28$. Angle of attack is $+5.36$ degrees (side orientation/coarse grid).	54
4-20 Vertical velocity at $X/\text{Span} = -1.67$. Angle of attack is $+5.36$ degrees (side orientation/coarse grid).	55
4-21 Spanwise velocity at $X/\text{Span} = -0.34$. Angle of attack is $+5.36$ degrees (top orientation/coarse grid).	55
4-22 Spanwise velocity at $X/\text{Span} = -0.66$. Angle of attack is $+5.36$ degrees (top orientation/coarse grid).	56
4-23 Spanwise velocity at $X/\text{Span} = -1.28$. Angle of attack is $+5.36$ degrees (top orientation/coarse grid).	56
4-24 Axial vorticity at $X/\text{Span} = -0.044$. Angle of attack is $+5.36$ degrees (coarse grid).	57
4-25 Axial vorticity at $X/\text{Span} = -0.66$. Angle of attack is $+5.36$ degrees (coarse grid).	57

4-26	Streamwise velocity at $X/\text{Span} = -0.044$. Angle of attack is -5.36 degrees (side orientation/coarse grid).	59
4-27	Streamwise velocity at $X/\text{Span} = -1.67$. Angle of attack is -5.36 degrees (side orientation/coarse grid).	59
4-28	Vertical velocity at $X/\text{Span} = -0.044$. Angle of attack is -5.36 degrees (side orientation/coarse grid).	60
4-29	Vertical velocity at $X/\text{Span} = -1.67$. Angle of attack is -5.36 degrees (side orientation/coarse grid).	60
4-30	Streamwise velocity at $X/\text{Span} = -0.044$. Angle of attack is $+5.36$ degrees (side orientation/fine grid).	61
4-31	Streamwise velocity at $X/\text{Span} = -0.34$. Angle of attack is $+5.36$ degrees (side orientation/fine grid).	61
4-32	Streamwise velocity at $X/\text{Span} = -0.66$. Angle of attack is $+5.36$ degrees (side orientation/fine grid).	62
4-33	Vertical velocity at $X/\text{Span} = -0.044$. Angle of attack is $+5.36$ degrees (side orientation/fine grid).	62
4-34	Vertical velocity at $X/\text{Span} = -0.34$. Angle of attack is $+5.36$ degrees (side orientation/fine grid).	63
4-35	Vertical velocity at $X/\text{Span} = -0.66$. Angle of attack is $+5.36$ degrees (side orientation/fine grid).	63
4-36	Spanwise velocity at $X/\text{Span} = -0.34$. Angle of attack is $+5.36$ degrees (top orientation/fine grid).	64
4-37	Spanwise velocity at $X/\text{Span} = -0.66$. Angle of attack is $+5.36$ degrees (top orientation/fine grid).	64
5-1	Comparison of spanwise circulation distribution by increasing the number of spanwise panels	66
5-2	Comparison of vertical position of wake sheet by increasing the number of spanwise panels	67

5-3	Comparison of vertical position of wake sheet by increasing the number of spanwise panels	67
5-4	Comparison of vertical position of wake sheet by increasing the number of spanwise panels	68
5-5	Complete panelling scheme for 16 spanwise panels. (Downstream looking forward.)	69
5-6	Comparison of spanwise circulation distribution by increasing downstream tunnel length	70
5-7	Comparison of spanwise wake shape by increasing downstream tunnel length	70
5-8	Comparison of spanwise wake shape by increasing downstream tunnel length	71
5-9	Comparison of spanwise wake shape by increasing downstream tunnel length	71
5-10	Comparison of tip vortex position by increasing downstream tunnel length	72
5-11	Comparison of root vortex position by increasing downstream tunnel length	72
5-12	Calculated lift and drag coefficients	73
5-13	Computed streamwise velocity at $X/\text{Span}=-0.044$. Angle of attack is +5.36 degrees (coarse grid).	75
5-14	Computed spanwise velocity at $X/\text{Span}=-0.044$. Angle of attack is +5.36 degrees (coarse grid).	75
5-15	Computed vertical velocity at $X/\text{Span}=-0.044$. Angle of attack is +5.36 degrees (coarse grid).	76
5-16	Computed streamwise velocity at $X/\text{Span}=-0.34$. Angle of attack is +5.36 degrees (coarse grid).	76
5-17	Computed spanwise velocity at $X/\text{Span}=-0.34$. Angle of attack is +5.36 degrees (coarse grid).	77

5-18	Computed vertical velocity at $X/Span=-0.34$. Angle of attack is +5.36 degrees (coarse grid).	77
5-19	Computed streamwise velocity at $X/Span=-0.66$. Angle of attack is +5.36 degrees (coarse grid).	78
5-20	Computed spanwise velocity at $X/Span=-0.66$. Angle of attack is +5.36 degrees (coarse grid).	79
5-21	Computed vertical velocity at $X/Span=-0.66$. Angle of attack is +5.36 degrees (coarse grid).	79
5-22	Computed streamwise velocity at $X/Span=-1.28$. Angle of attack is +5.36 degrees (coarse grid).	80
5-23	Computed spanwise velocity at $X/Span=-1.28$. Angle of attack is +5.36 degrees (coarse grid).	80
5-24	Computed vertical velocity at $X/Span=-1.28$. Angle of attack is +5.36 degrees (coarse grid).	81
5-25	Computed streamwise velocity at $X/Span=-1.67$. Angle of attack is +5.36 degrees (coarse grid).	81
5-26	Computed spanwise velocity at $X/Span=-1.67$. Angle of attack is +5.36 degrees (coarse grid).	82
5-27	Computed vertical velocity at $X/Span=-1.67$. Angle of attack is +5.36 degrees (coarse grid).	82
5-28	Comparison of streamwise velocities across the surface of the hydrofoil at 0 degree angle of attack	83
5-29	Comparison of spanwise velocities across the surface of the hydrofoil at 0 degree angle of attack	83
5-30	Comparison of vertical velocities across the surface of the hydrofoil at 0 degree angle of attack	84
5-31	Comparison of streamwise velocities across the surface of the hydrofoil at 0 degree angle of attack	84
5-32	Experimental wake shape with panel code predicted wake shape superimposed. ($X/Span=-0.044$)	85

5-33	Experimental wake shape with panel code predicted wake shape superimposed. ($\mathbf{X}/\text{Span}=-0.34$)	86
5-34	Experimental wake shape with panel code predicted wake shape superimposed. ($\mathbf{X}/\text{Span}=-0.66$)	86
5-35	Experimental wake shape with panel code predicted wake shape superimposed. ($\mathbf{X}/\text{Span}=-1.28$)	87
5-36	Experimental wake shape with panel code predicted wake shape superimposed. ($\mathbf{X}/\text{Span}=-1.67$)	87
7-1	Standard deviation of streamwise velocity at $\mathbf{X}/\text{Span} =-0.044$. Angle of attack is +5.36 degrees (side orientation/coarse grid).	92
7-2	Standard deviation of streamwise velocity at $\mathbf{X}/\text{Span} =-0.34$. Angle of attack is +5.36 degrees (side orientation/coarse grid).	92
7-3	Standard deviation of streamwise velocity at $\mathbf{X}/\text{Span} =-0.66$. Angle of attack is +5.36 degrees (side orientation/coarse grid).	93
7-4	Standard deviation of streamwise velocity at $\mathbf{X}/\text{Span} =-1.28$. Angle of attack is +5.36 degrees (side orientation/coarse grid).	93
7-5	Standard deviation of streamwise velocity at $\mathbf{X}/\text{Span} =-1.67$. Angle of attack is +5.36 degrees (side orientation/coarse grid).	94
7-6	Standard deviation of spanwise velocity at $\mathbf{X}/\text{Span} =-0.34$. Angle of attack is +5.36 degrees (top orientation/coarse grid).	94
7-7	Standard deviation of spanwise velocity at $\mathbf{X}/\text{Span} =-0.66$. Angle of attack is +5.36 degrees (top orientation/coarse grid).	95
7-8	Standard deviation of spanwise velocity at $\mathbf{X}/\text{Span} =-1.28$. Angle of attack is +5.36 degrees (top orientation/coarse grid).	95
7-9	Standard deviation of vertical velocity at $\mathbf{X}/\text{Span} =-0.044$. Angle of attack is +5.36 degrees (side orientation/coarse grid).	96
7-10	Standard deviation of vertical velocity at $\mathbf{X}/\text{Span} =-0.34$. Angle of attack is +5.36 degrees (side orientation/coarse grid).	96

7-11 Standard deviation of vertical velocity at $X/\text{Span} = -0.66$. Angle of attack is +5.36 degrees (side orientation/coarse grid). 97

7-12 Standard deviation of vertical velocity at $X/\text{Span} = -1.28$. Angle of attack is +5.36 degrees (side orientation/coarse grid). 97

7-13 Standard deviation of vertical velocity at $X/\text{Span} = -1.67$. Angle of attack is +5.36 degrees (side orientation/coarse grid). 98

7-14 Standard deviation of streamwise velocity at $X/\text{Span} = -0.66$. Angle of attack is +5.36 degrees (side orientation/fine grid). 98

7-15 Standard deviation of vertical velocity at $X/\text{Span} = -0.044$. Angle of attack is +5.36 degrees (side orientation/fine grid). 99

7-16 Standard deviation of vertical velocity at $X/\text{Span} = -0.34$. Angle of attack is +5.36 degrees (side orientation/fine grid). 99

7-17 Standard deviation of vertical velocity at $X/\text{Span} = -0.66$. Angle of attack is +5.36 degrees (side orientation/fine grid). 100

7-18 Standard deviation of spanwise velocity at $X/\text{Span} = -0.66$. Angle of attack is +5.36 degrees (top orientation/fine grid). 100

Chapter 1

Introduction

Fluid behavior around hydrofoils and airfoils has interested naval architects and aerodynamicists for some time. Understanding and modelling the flow around a simple hydrofoil has established fundamental principles which can then be applied to marine propellers and helicopter rotors. The examination of flow past the single hydrofoil has led to improved design of aircraft wings and surface ship and submarine control surfaces.

In particular, the flow around the tip of a foil has been studied by engineers of virtually all of these major industries. A concentrated tip vortex is created as a byproduct of the lift and the three dimensionality of a lifting surface geometry. It is the tip vortex which generates the very powerful, spiraling horizontal columns of air in the wake of large jet aircraft, inducing a dangerous roll moment on any trailing aircraft. This problem becomes especially acute when, in the interest of efficiency, numerous aircraft closely follow one another both landing and taking off from major metropolitan airports, generally only minutes apart.

The rotor blades on a helicopter are also foils which closely follow one another on the same flight path. Tip vortices generated from the individual blades create a turbulent and swirling inflow for the subsequent blade which leads to unwanted noise and vibration. Control of the tip vortices of helicopter blades would extend the life of the entire rotor assembly.

Marine propellers suffer from the same problem and propeller designs are often

based upon eliminating blade tip cavitation. Cavitation develops from the same conditions which create tip vortices and leads to both propeller vibration and noise. Cavitation also causes pitting and corrosion of the blade surface. All of these factors contribute to a reduction of propeller efficiency and desirability.

Control surfaces used to stabilize surface ships in roll and used to control the submerged submarine also have specific design criteria. A submerged control surface must be designed to minimize the debilitating effects of cavitation similar to a marine propeller, but must also be efficient and functionally similar to the aircraft wing.

In the aeronautics industry, there have been two approaches developed to tackle the problem of wing tip vortices. One method is simply to detect the vortices in airport environments. Numerous sensors such as hot-wire anemometers, acoustic sensors and laser-radar (LIDAR) have been installed in aircraft to detect and warn pilots of impending danger. The other approach has been to add various configurations to the wing tips in an attempt to eliminate or at least weaken the strength of the tip vortices.

In this work, the tip vortices from a submerged control surface are detected by a laser doppler velocimeter (LDV) and modelled by a code developed to predict the effects of different tip geometries on the trailing tip vortices.

Chapter 2

Mathematical Background

In the last few decades, as the full potential of computers in this application has been realized, there is increasing reliance on finite element analysis of complex flow behavior. For large Reynold's numbers (on the order of one million), the theory of potential flow establishes a basic description of flow patterns and finite element analyses, specifically panel methods, are extremely well suited to model the potential flow behavior. There are many variations of panel methods which have been developed and some are more successful than others in each of the various aerodynamic and hydrodynamic applications. Kerwin et al. [10], Lee [13] and Hsin [6] have developed robust and versatile perturbation potential panel methods which have been used in the analysis of marine propellers. They have been shown to accurately predict fluid behavior for highly skewed propellers, ducted propellers, and propellers encountering unsteady inflow. In this work, Hsin's code has been adapted to analyze the flow around a semi-span hydrofoil attached to a half body. The associated theory, based on Lamb [12], is discussed below.

2.1 Green's 2nd Identity and perturbation flow

2.1.1 Single Domain

The foundation of panel methods is Green's 2nd Identity. However, to understand the usefulness of the theorem, one must begin with the fundamental principles of potential flow theory. Using this theory, flow is defined to be incompressible, inviscid, and irrotational. This allows the continuity equation for conservation of mass to be represented by the familiar differential equation of Laplace:

$$\nabla^2\Phi = 0 \quad (2.1)$$

where

$$\mathbf{V} = \nabla\Phi, \quad (2.2)$$

\mathbf{V} being the velocity vector of the fluid and Φ is the total velocity potential of the fluid.

Green's 2nd Identity states that for two arbitrary harmonic functions ϕ and \mathcal{G} defined inside a volume \mathcal{V} which satisfy the Laplace equation (2.1) then

$$\int \int (\phi \frac{\partial \mathcal{G}}{\partial n} - \mathcal{G} \frac{\partial \phi}{\partial n}) d\mathcal{S} = 0 \quad (2.3)$$

or

$$\int \int \phi \frac{\partial \mathcal{G}}{\partial n} d\mathcal{S} = \int \int \mathcal{G} \frac{\partial \phi}{\partial n} d\mathcal{S} \quad (2.4)$$

where \mathbf{n} is the unit vector normal to the surface \mathcal{S} at point q and pointing into the fluid domain \mathcal{V} (See Figure 2-1). \mathcal{S} is the surface which encloses the volume \mathcal{V} . Green's 2nd Identity can easily be proved by invoking the divergence theorem.

Let ϕ represent the velocity potential of the fluid throughout the volume \mathcal{V} and make $\mathcal{G} = 1/r$ where r is the distance between a control point q in the fluid domain, either on the surface \mathcal{S} or within its boundaries, and p a fixed point located anywhere.

Examine the situation which arises if the point p is located in the fluid domain.

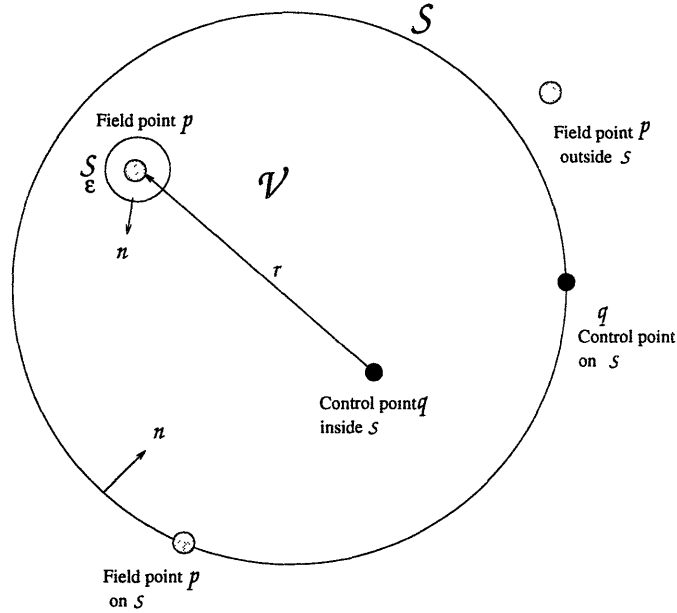


Figure 2-1: Basic geometrical relationships for Green's 2nd Identity

It is possible for the variable point q and the fixed point p to be collocated causing r to become zero and \mathcal{G} to be unbounded. To avoid this, Gauss' law is employed. Consider a small sphere \mathcal{S}_ϵ surrounding the point, with p at its center. Let the total surface area be $\mathcal{S}_\epsilon + \mathcal{S}$. Equation (2.4) may be rewritten

$$\iint \phi(q) \frac{\partial}{\partial n} \left(\frac{1}{r} \right) d\mathcal{S}_\epsilon + \iint \phi(q) \frac{\partial}{\partial n} \left(\frac{1}{r} \right) d\mathcal{S} = \iint \frac{1}{r} \frac{\partial \phi(q)}{\partial n} d\mathcal{S}_\epsilon + \iint \frac{1}{r} \frac{\partial \phi(q)}{\partial n} d\mathcal{S}. \quad (2.5)$$

Gauss' law states

$$\iint \mathbf{u} \cdot \mathbf{n} d\mathcal{S}_\epsilon = 4\pi m(p) \quad (2.6)$$

or to be consistent

$$\iint \frac{\partial \phi(q)}{\partial n} d\mathcal{S}_\epsilon = 4\pi m(p) \quad (2.7)$$

where $m(p)$ is the strength of a source placed at the point p and \mathbf{u} is the velocity vector due to the potential at point p . Rather than considering the potential on the surface \mathcal{S}_ϵ due to the potential at p , consider at the potential at point p due to a distributed potential on the surface \mathcal{S}_ϵ .

Examination of Figure 2-1 shows that the normal vector to this surface \mathcal{S}_ϵ is

identically opposite in direction to the radius vector thus

$$\frac{\partial\phi(q)}{\partial n} = -\frac{\partial\phi(q)}{\partial r}. \quad (2.8)$$

Substituting the above into Equation (2.7),

$$\int \int \frac{\partial\phi(q)}{\partial r} d\mathcal{S}_\epsilon = -4\pi m(p). \quad (2.9)$$

Presuming that this sphere \mathcal{S}_ϵ is hollow with a constant radius R and all the potential $\phi(q)$ located on its surface, the $\partial/\partial r$ term may be moved out of the integral and

$$\frac{\partial}{\partial r} \int \int \phi(q) d\mathcal{S}_\epsilon = -4\pi m(p). \quad (2.10)$$

The potential in three dimensions of a source is given by

$$\phi(R) = \frac{m}{4\pi R} = \phi_p. \quad (2.11)$$

Substituting this into Equation (2.10) for m gives

$$\frac{\partial}{\partial r} \int \int \phi(q) d\mathcal{S}_\epsilon = -(4\pi)^2 R \phi_p \quad (2.12)$$

and taking the integral of both sides from 0 to R results in

$$\int \int \phi(q) d\mathcal{S}_\epsilon = -(4\pi)^2 R^2 \phi_p. \quad (2.13)$$

Substituting this into the first term of Equation (2.5) and noting that

$$\frac{\partial}{\partial n} \left(\frac{1}{r} \right) = -\frac{1}{r^2},$$

the term becomes

$$\int \int \phi(q) \frac{\partial}{\partial n} \left(\frac{1}{r} \right) d\mathcal{S}_\epsilon = 4\pi \phi_p \quad (2.14)$$

which is independent of the radius of the small sphere \mathcal{S}_ϵ .

Evaluating the first term on the right hand side of Equation (2.5) for a sphere of a specified radius R ,

$$\int \int \frac{1}{r} \frac{\partial \phi(q)}{\partial n} d\mathcal{S}_\epsilon = 4\pi R \phi(q). \quad (2.15)$$

When $R \rightarrow 0$, the term will vanish, leaving Equation (2.5) as

$$\phi_p = -\frac{1}{4\pi} \int \int \frac{1}{r} \frac{\partial \phi(q)}{\partial n} d\mathcal{S} + \frac{1}{4\pi} \int \int \phi(q) \frac{\partial}{\partial n} \left(\frac{1}{r} \right) d\mathcal{S}. \quad (2.16)$$

If the field point p is located external to the surface \mathcal{S} , the function \mathcal{G} is now finite everywhere and no modification of Equation 2.3 is required. Thus

$$0 = -\frac{1}{4\pi} \int \int \frac{1}{r} \frac{\partial \phi(q)}{\partial n} d\mathcal{S} + \frac{1}{4\pi} \int \int \phi(q) \frac{\partial}{\partial n} \left(\frac{1}{r} \right) d\mathcal{S}. \quad (2.17)$$

This leaves the final possibility, that the fixed point p is located on the surface \mathcal{S} and again p and q could be collocated. In this case, \mathcal{S} is indented by a small hemisphere. Using the same logic as above with the small sphere, Equation 2.4 is modified to give

$$\frac{1}{2} \phi_p = -\frac{1}{4\pi} \int \int \frac{1}{r} \frac{\partial \phi(q)}{\partial n} d\mathcal{S} + \frac{1}{4\pi} \int \int \phi(q) \frac{\partial}{\partial n} \left(\frac{1}{r} \right) d\mathcal{S}. \quad (2.18)$$

The $1/2$ results from the surface area of a hemisphere being half that of a complete sphere.

The three equations, (2.16), (2.17), and (2.18), allow the value of the potential ϕ to be calculated at any point p in or out of the fluid domain. It is determined by the values of the potential $\phi(q)$ and $\partial \phi(q)/\partial n$ at the boundary of surface \mathcal{S} . Closer inspection reveals that the first term appears very similar to Equation (2.11). Thus the first term represents the summation of source singularities on the surface \mathcal{S} with a strength of $-\partial \phi(q)/\partial n$ per unit area. The second term is similar to

$$\phi = \frac{\mu}{4\pi} \left(\frac{1}{r^2} \right) \quad (2.19)$$

which is the equation for a dipole in three dimensions with μ equal to the strength of

the dipole. In this case μ is equated to $\phi(q)$, the dipole strength per unit area.

Equations (2.16), (2.17), and (2.18) may be combined into a general form

$$T4\pi\phi_p = \int \int -\frac{1}{r} \frac{\partial\phi(q)}{\partial n} d\mathcal{S} + \int \int \phi(q) \frac{\partial}{\partial n} \left(\frac{1}{r}\right) d\mathcal{S} \quad (2.20)$$

where when

$T=1$ p lies within the fluid domain \mathcal{V} , but not on \mathcal{S} ; when

$T=0$ p lies outside of the fluid domain \mathcal{V} , but not on \mathcal{S} ; and when

$T=\frac{1}{2}$ p lies on either face of the surface \mathcal{S} .

The significance of Equation (2.20) is that if one of the two surface functions, ϕ or $\partial\phi/\partial n$ is known at all points q on \mathcal{S} , then using Equation (2.20) with $T=1/2$ for both p and q located on the surface \mathcal{S} , the complementary surface function may be obtained because essentially there is only one unknown; ϕ_p and $\phi(q)$ are the same. Once both surface functions are defined, the potential at any point p in the fluid domain may be deduced. In other words, the Laplace differential equation has been restructured through the use of Green's 2^{nd} Identity to give a very useful integral equation.

2.1.2 Multiple domains

Equation (2.20) must be further refined to apply it to the problem of a semi-span hydrofoil attached to a half body within a water tunnel because there are multiple domains. Consider the situation depicted in Figure 2-2. There are two surfaces, \mathcal{S}_B and \mathcal{S}_∞ . The two surfaces may be thought of as parts of a larger surface \mathcal{S} which bounds the fluid domain labelled \mathcal{V} . The single valued potential distributed in the domain \mathcal{V} , external to surface \mathcal{S}_B is defined as ϕ . The single valued potential distributed in the domain \mathcal{V}_i , enclosed by \mathcal{S}_B is defined as φ . The potential at point p , which is arbitrarily located in the fluid domain \mathcal{V} , is a combination of the contributions from all of the distributed single valued potential functions. The influence of the

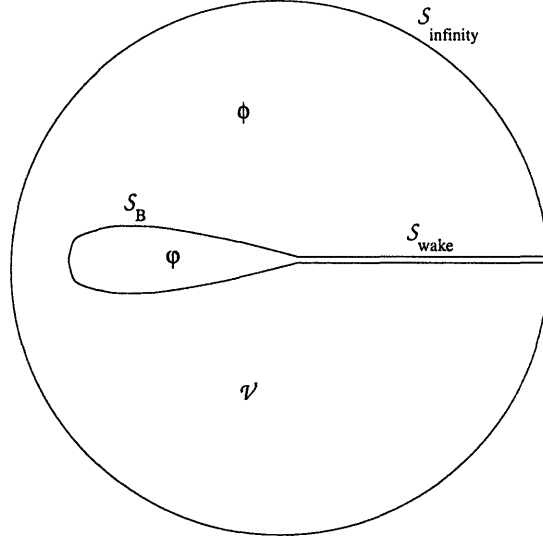


Figure 2-2: Geometrical relationships for Multi-domain case

potential, ϕ , comes directly from Equation (2.20) setting $\Gamma=1$

$$4\pi\phi_p = \iint -\frac{1}{r} \frac{\partial\phi}{\partial n_{B_o}} d\mathcal{S}_B + \iint \phi \frac{\partial}{\partial n_{B_o}} \left(\frac{1}{r}\right) d\mathcal{S}_B. \quad (2.21)$$

Similarly, setting $\Gamma=0$, the contribution due to the inner surface φ is

$$0 = \iint -\frac{1}{r} \frac{\partial\varphi}{\partial n_{B_i}} d\mathcal{S}_B + \iint \varphi \frac{\partial}{\partial n_{B_i}} \left(\frac{1}{r}\right) d\mathcal{S}_B. \quad (2.22)$$

Because the potential is a scalar, the Equations (2.21) and (2.22) may be added, carefully noting that the derivatives of the normal vectors for each face are in opposite directions, $\partial/\partial n_{B_o} = -\partial/\partial n_{B_i}$. Therefore the sum is

$$4\pi\phi_p = \iint -\frac{1}{r} \left(\frac{\partial\phi}{\partial n_{B_o}} - \frac{\partial\varphi}{\partial n_{B_o}} \right) d\mathcal{S}_B + \iint (\phi - \varphi) \frac{\partial}{\partial n_{B_o}} \left(\frac{1}{r}\right) d\mathcal{S}_B. \quad (2.23)$$

As the distance between a point q on \mathcal{S}_∞ and a point p near \mathcal{S}_B becomes infinite, the function \mathcal{G} goes to zero, leaving only the second integral from Equation (2.16). If the surface of the infinite boundary is represented as $4\pi r^2$, then Equation (2.16)

becomes simply

$$\phi_p = \phi_\infty. \quad (2.24)$$

Since the surface \mathcal{S}_∞ is such a great distance away from \mathcal{S}_B , ϕ_∞ is considered to be the potential of the fluid, undisturbed by the presence of the body. In the present formulation only the perturbation potential is determined; ϕ_∞ is set to zero.

Equation (2.23) may be rewritten

$$4\pi\phi_p = \iint K_1 \left(\frac{\partial\phi}{\partial n_{B_o}} - \frac{\partial\varphi}{\partial n_{B_o}} \right) d\mathcal{S}_B + \iint K_2 (\phi - \varphi) d\mathcal{S}_B \quad (2.25)$$

where

$$K_1 = -\frac{1}{r} \quad (2.26)$$

and

$$K_2 = \frac{\partial}{\partial n_{B_o}} \left(\frac{1}{r} \right) \quad (2.27)$$

are scalar “kernel” functions which are only dependent on the geometric relationship between the surface potential point q and the field point p .

Only one of the two distributions of potential φ or ϕ will have physical significance. In this analysis φ is considered fictitious and is set to zero; Equation (2.25) becomes

$$4\pi\phi_p = \iint K_1 \left(\frac{\partial\phi}{\partial n_{B_o}} \right) d\mathcal{S}_B + \iint K_2 \phi d\mathcal{S}_B \quad (2.28)$$

for a point not on the surface \mathcal{S}_B .

Presuming that this general surface \mathcal{S}_B is a physical body which might develop a trailing wake, Equation (2.28) must be modified to take the wake surface into account. The wake may be considered an infinitesimally thin closed surface. The wake characteristically defines a discontinuity in potential from one face to the other and the direction of the velocity vector will endure an instantaneous change. The component of velocity normal to the wake surface is considered continuous, but equal to zero

$$\left(\frac{\partial\phi}{\partial n} \right)_{upper} - \left(\frac{\partial\phi}{\partial n} \right)_{lower} = 0. \quad (2.29)$$

If

$$\Delta\phi = \phi_{upper} - \phi_{lower}, \quad (2.30)$$

then applying Equation (2.20) to the wake with $\Gamma=0$ results in

$$0 = \int \int K_2 \Delta\phi d\mathcal{S}_{wake}. \quad (2.31)$$

Including the contributions from the wake, the potential at any point p in the fluid domain \mathcal{V} may be determined from

$$4\pi\phi_p = \int \int K_1 \left(\frac{\partial\phi}{\partial n_{B_0}} \right) d\mathcal{S}_B + \int \int K_2 \phi d\mathcal{S}_B + \int \int K_2 \Delta\phi d\mathcal{S}_{wake}. \quad (2.32)$$

If the point p is on the surface of \mathcal{S}_B , $\Gamma=1/2$ and

$$2\pi\phi_p = \int \int K_1 \left(\frac{\partial\phi}{\partial n_{B_0}} \right) d\mathcal{S}_B + \int \int K_2 \phi d\mathcal{S}_B + \int \int K_2 \Delta\phi d\mathcal{S}_{wake}. \quad (2.33)$$

It is Equation (2.33) which is the basis of the numerical formulation of the solution. However, the solution of Equation (2.33) is not unique without the implementation of some boundary conditions on the surface and the trailing edge.

The kinematic or external Neumann boundary condition dictates the value of the velocity at the body surface. It is this relation which uniquely relates the perturbation potential to the total potential. The kinematic boundary condition for a solid surface may be written

$$\frac{\partial\Phi}{\partial n} = 0 \quad (2.34)$$

where Φ is the total potential of the fluid and is equal to ϕ_p found from Equation (2.33) added to ϕ_∞

$$\frac{\partial\phi_p}{\partial n} = -\mathbf{U} \cdot \mathbf{n}. \quad (2.35)$$

In addition, the Kutta condition, which requires flow around the trailing edge to be finite, must be imposed. Kerwin et al. [10] present an explicit non-linear pressure Kutta condition. For the numerical formulation of the Kutta condition, the potential jump in the wake is set equal to the total potential values at the trailing edge of the

hydrofoil giving:

$$\Delta\phi_{wake} = \Phi_{t.e.upper} - \Phi_{t.e.lower} = \phi_{t.e.upper} - \phi_{t.e.lower} + \mathbf{U}_\infty \cdot \mathbf{r}_{t.e.} \quad (2.36)$$

where $\mathbf{r}_{t.e.}$ is the unit vector which bisects the hydrofoil angle of attack.

Thus Equation (2.33) becomes a Fredholm integral equation of the second kind [13]. This leaves ϕ as the sole remaining unknown. Converting the surface integrals into summations, discussed in the next chapter, Equation (2.33) may be solved for ϕ by solving a linear system of equations.

2.2 Application to a water tunnel

The modelling of a body within an air or water tunnel is more complicated than simply modelling a body travelling in an infinite domain. Specifically, the decision arises whether to apply the boundary integral equations to the confines of the tunnel or to apply them to the tunnel and the infinite boundary. In the latter case, the entire tunnel assembly acts like a body moving through an infinite domain.

If the tunnel walls enclose the fluid domain, then the kinematic boundary condition must be applied to the four longitudinal surfaces and the flow through the upstream “endcap” is forced to equal the undisturbed inflow, \mathbf{U} . The difficult task lies in defining the correct boundary condition for the downstream endcap, specifically where it intersects the wake sheet. For a tunnel of finite length, panelling the downstream cap adds another layer of difficulty as the panels must reflect the shape of the wake and the associated tip vortex roll-up.

An alternative approach is to model the entire tunnel assembly as if it were placed in a uniform stream. The infinite boundary, \mathcal{S}_∞ , remains as it was for the general case as described in section 2.1.2. Near this infinite boundary the perturbation potential becomes zero, as before, leaving the total fluid potential equal to that of the uniform stream

$$\frac{\partial\phi_{\infty p}}{\partial n} = \mathbf{U}$$

where the inflow velocity, \mathbf{U} , is given an arbitrary magnitude, but the direction of \mathbf{U} has been aligned with the longitudinal axis of the water tunnel.

Green's 2nd Identity must be applied to all surfaces, including both sides of the tunnel walls. Similar to the wake sheet, the walls may be considered to be a very thin closed surface, allowing the entire tunnel assembly to be a multi-component closed surface, $\mathcal{S}_{\mathcal{B}}$. Within the region of interest, inside the walls of the tunnel, the contributions of the half body, the hydrofoil, and the inside surface of the tunnel walls are summed as before using the kinematic boundary condition to specify the source distribution. The same boundary condition is applied to the outer surface of the tunnel walls, but the inflow runs parallel to these surfaces and the perturbation flow is zero.

Specifying the inflow velocity in this manner satisfies not only the mathematical dilemma of finding a non-singular solution, but it also satisfies a physical quandary of preventing the flow velocity at the trailing edge of the tunnel walls from becoming unbounded through the use of continuity. The fixed inflow vector ensures the criterion for the Kutta condition is met.

The wake sheet also extends infinitely downstream, in reality rolling up into a concentrated tip vortex. The wake's influence on the hydrofoil beyond several chordlengths becomes minimal and is ignored in this treatment of the near field effects.

Equation (2.33) may therefore be used to solve the potential flow problem of flow past the semi-span hydrofoil and half body configuration within the confines of a water tunnel.

Chapter 3

Numerical Formulation

There are numerous panel-based formulations which have been developed over the years to address complex flow modelling. Although they differ in the placement and the category of the distributed singularities, they all rely on a discretization of the various integral equations. Some methods are more adept at particular flow patterns than others. In the case of the semi-span problem presented here, a low-order perturbation potential method is utilized.

3.1 Discretization of the Boundary Integral Equation

Both Lee [13] and Hsin [6] elaborate on some of the advantages of using the perturbation potential method. Some of these advantages include:

- The accuracy of potential based methods have been found to be more accurate than velocity based methods.
- Potential based methods are less affected by irregular panelling.
- Scalars such as potentials require one third the allocated memory of vectors.
- $\mathbf{n} \cdot \nabla \phi_\infty$ is easily specified.

Hunt [7] gives some background on the process of discretization of integral equations such as Fredholm's Integral Equation of the 2nd Kind (Equation 2.33). According to Hunt, there are essentially three basic discretization errors which occur when forming the numerical solution and all contribute in some way to the deviation from the analytical solution:

- Approximation of the physical surfaces
- Discretization of the boundary conditions
- Discretization of the singularity distributions

The most intuitive source of error in the finite element modelling is derived from the coarse approximation of a body's surface. Although it is possible to develop higher order geometric shapes to cope with highly skewed and curved surfaces, planar rectangular panels are used in this work on the semi-span hydrofoil and its surrounding geometry.

There are two major sources of error due to the panelled approximation of the solid surface, both of them relating to the imposed kinematic boundary condition. First, the calculation of the unit vector normal to a panel surface, particularly in regions of high curvature, does not reflect the direction normal to the true surface at all points. Secondly, the kinematic boundary condition should be satisfied everywhere on a solid surface. However, in the panel approximation, the boundary condition may only be feasibly satisfied, in the interest of computer time and memory, at one point on each panel, commonly the centroid of each panel. As the number of panels is increased, these errors are diminished.

The selection of this singular point to satisfy the boundary condition leads to two errors in the finite element solution. Because the point may not actually lie on the surface being modelled due to the approximation of the surface with panels, the true boundary condition for the exact shape in the problem may not be realized. Additionally, because the boundary condition is only satisfied at one point on the panel, there will develop a small amount of leakage past the panel into the "solid"

surface. These errors also may be minimized by increasing the number of panels and carefully selecting the distribution of surface functions.

The surface functions attributed to individual panels may be represented by functions of any order, from piecewise constant to bicubic splines. In the present analysis, the unknown surface function of Equation (2.33) is piecewise constant over the panel. The function is made up of two parts: a function of unit strength, $g(\xi, \eta)$, where ξ and η are the local two dimensional coordinates on the panel, and a weighing factor, w , which is of unknown magnitude such that

$$\sum_{j=1}^N w_j \int \int_{\mathcal{S}_j} g_j(\xi, \eta) K(p, q) d\mathcal{S}_j = b(p) \quad (3.1)$$

with \mathcal{S}_j denoting the surface area of the individual panel and N representing the total number of panels. The right hand side $b(p)$ forms the boundary condition at a particular point p on the surface \mathcal{S} .

In the semi-span case, the unknown surface function is $\phi(q)$. For each panel, combining the kernel function K with the unit strength function $g(\xi, \eta)$ gives a new variable, D_{ij} on the body or W_{ij} on the wake. Intuitively, D_{ij} and W_{ij} represent the induced potential at a field point p_i due to a panel with a unit strength potential function distributed uniformly across its surface, \mathcal{S}_j . Specifically for the perturbation potential method used here, both D_{ij} and W_{ij} represent unit dipole distributions. The source strengths are derived from the kinematic boundary condition.

Let N indicate the number of panels on the surface \mathcal{S}_B and N_W panels on the wake surface \mathcal{S}_{wake} . Denote the weighting factor w as ϕ for the body and $\Delta\phi$ for the wake. Substituting these new variables into Equation (3.1), the boundary integral equation (2.33) may be discretized as

$$\int \int K_2 \phi d\mathcal{S}_B + \int \int K_2 \Delta\phi d\mathcal{S}_{wake} \approx \sum_{j=1}^N D_{ij} \phi + \sum_{j=1}^{N_W} W_{ij} \Delta\phi \quad (3.2)$$

where the $2\pi\phi_P$ term of Equation (2.33) is incorporated into the first summation on the right hand side.

The remaining term from Equation (2.33) becomes the boundary condition $b(p)$

$$b(p) = \int \int K_1 \left(\frac{\partial \phi}{\partial n_{Bo}} \right) d\mathcal{S}_B = \sum_{j=1}^N S_{ij} \left(\frac{\partial \phi}{\partial n_{Bo}} \right)_j. \quad (3.3)$$

$$i = 1, 2, 3, \dots, N$$

This is the link between the total potential of the system and the perturbation potential. Recall the kinematic boundary condition (Equation 2.35) specifies $\partial\phi/\partial n_{Bo}$. S_{ij} is the induced potential at p_i due to a unit source strength distributed on panel \mathcal{S}_j .

Equations (3.2) and (3.3) may be represented by the following matrix equation

$$[A]\{\phi\} = [B] - [W]\{\Delta\phi\} \quad (3.4)$$

where the matrices $[A]$, $[B]$ and $[W]$ are known as “influence coefficient” matrices. The method used to calculate the influence coefficients was derived by Newman [15] who determines the exact forms of

$$\int \int_S K_2 d\mathcal{S}_j$$

for field points p near the panel and develops multipole expansions used when the field points are at distances much greater than the panel dimensions. A similar approach is used to calculate

$$\int \int_S K_1 d\mathcal{S}_j.$$

for the source terms. Because these influence coefficient matrices are quite large ($N \times N$), an iterative block solver routine developed by Clark [3] is used to solve the system of equations. With the influence coefficients now defined, the geometry of the problem must be developed.

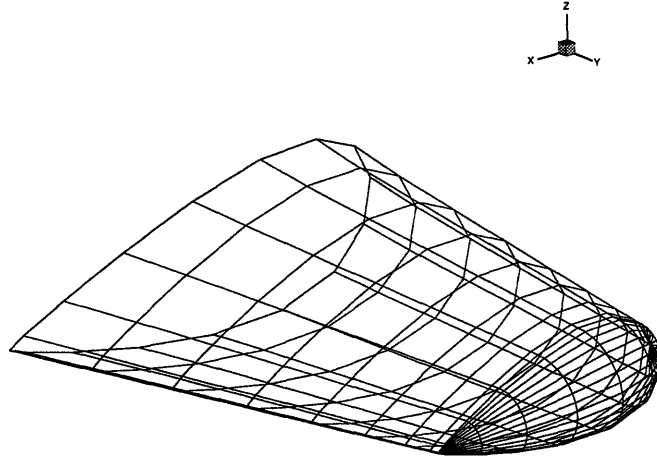


Figure 3-1: Panel arrangement for hydrofoil, $M_r = 6$, $N_c = 12$

3.2 Foil geometry

The cartesian coordinate system for the computer model originates at the midpoint of the root chord of the foil. The x -axis is aligned with the inflow velocity and the y -axis is directed outboard. Since the starboard half of the configuration is modelled, the resulting z -axis, by the right hand convention, points upward. The span of the hydrofoil is chosen to be the fundamental length for the entire model.

The semi-span foil is generated by dividing the unit spanlength into M_r spanwise panels. A half-cosine spacing scheme is used to concentrate panels at the tip for better definition of the flow in that region.

The planform of the foil, unlike the physical model, is symmetric about the mid-chord line with the leading and trailing edge slopes equal to the ratio between the tip and root chords. Also unlike the physical model which has a NACA 0012 shape at the tip, the computer model uses a NACA 0018 chordwise profile throughout. The chordwise panels have full cosine spacing with the total number of panels, N_c , equal to the sum of panels on the upper and lower surface of the foil (See Figure 3 – 1). The foil’s spanwise thickness distribution is linear and based on the ratio of the tip

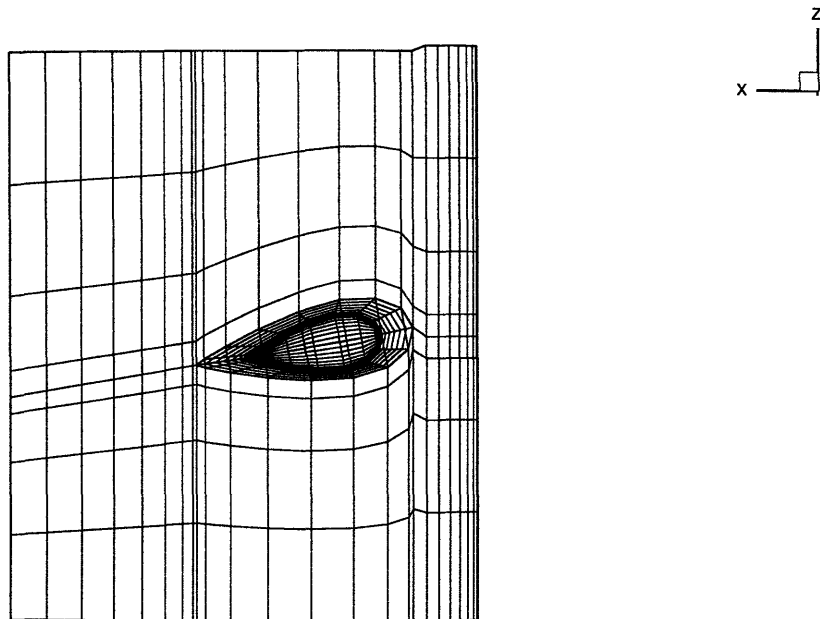


Figure 3-2: Panel arrangement on foil and body. $N_u = 8, N_b = 8, N_d = 8, M_t = 8,$
 $\alpha=10$ degrees

and root chords. From these parameters, the coordinates of each panel node can be determined uniquely.

The tip of the foil is a revolved section of a radius equal to the thickness of the foil at its outermost point. Figure 3-1 shows the tip panelling scheme.

3.3 Body geometry

The body geometry is dependent upon the foil and wake geometries. Measurements from the experimental model position the hydrofoil on the body and determine the body dimensions relative to the span of the hydrofoil. The thickness distribution is that of a NACA four digit airfoil [1] with the trailing edge thickness value set to zero to create a symmetric surface about its centerline. The top and bottom of the body are not modelled as rounded sections like the physical model, rather the body spans the height of the tunnel.

Body panelling is shown in Figure 3-2. It is critical that the panel boundaries of the foil exactly match those of the body, therefore the full cosine chordwise panel spacing of the foil is reflected in the body's mid-chord section. The panel spacing

forward of the foil is half-cosine spaced to better represent the increased curvature of the leading edge of the body. The panelling aft of the foil is driven by the half-cosine streamwise panel spacing of the wake. In addition, the panels aft of the foil adjust vertically as the wake sheet is iterated to align with the local flow velocity.

The body's spanwise panelling follows the contours of the foil and wake near midspan, but gradually straighten to become parallel to the floor and ceiling of the tunnel (See Figure 3-2). As the foil is positioned to various angles of attack, the panels on the body must reflect the change. This code presumes that the foil is rotated on an axis located at the $1/4$ chord of the foil. As the foil rotates, a gap would appear at the base of the foil due to the curvature of the body's thickness profile. The fairing associated with the experimental model is not simulated in the computer code. It is acknowledged that the gap that develops and the discontinuity which then occurs at the root of the trailing edge of the foil is not given proper consideration in this first approximation panel code. In this model, the root of the semi-span foil is adjusted such that it always matches the four-digit contour of the body. Further modelling of the gap and the resulting root vortex which develops is reserved for future work.

3.4 Wall geometry

The panelling on the walls is derived from the foil, wake, and body panelling schemes. The tunnel height is dictated by the span of the body and the tunnel test section is square, but the remaining length dimensions may be entered by the user. This allows flexibility to vary the length of the downstream section to observe the model's limitations due to the finite tunnel walls.

3.5 Wake geometry

Unlike the preceding geometries, the wake sheet panels only consists of dipoles. Since this work addresses the steady state problem, the wake sheet is modelled as semi-

infinite. To accomplish this, the panels of interest extend the length of the downstream tunnel wall at which point an additional set of panels, set to be ten span lengths long, are added to the wake sheet streamwise to simulate the effects of the starting vortex. The panelling nearest the foil is half-cosine spaced to ensure that a panel size mismatch does not occur at the foil's trailing edge where the foil panels are small. The panels are distributed spanwise identically to those on the foil.

The position of the simulated wake sheet affects the wake's influence on the foil's potential. If its position is altered, the circulation distribution on the foil will reflect the change. The dipole strength in the wake is directly dependent upon the circulation of the foil. Revising the wake's dipole strength alters its geometry as it must be aligned with the local velocity vector to enforce no flow through the wake sheet stipulation. Aligning the wake thus becomes an iterative process.

As described in Chapter 2, the Kutta condition is applied numerically as

$$\Delta\phi = \phi_{upper} - \phi_{lower} + \mathbf{U} \cdot \mathbf{r}_{te}.$$

The strength of the wake sheet dipoles are adjusted iteratively until the pressures along the upper trailing edge panels match those along the lower trailing edge. The above equation becomes the initial guess at the potential difference between the trailing edge panels. Lee [13] then adds another term, $K(\Delta C_p)_{te}$. K is a coefficient which is determined by the iteration described below and $(\Delta C_p)_{te}$ is the non-dimensional pressure coefficient at the trailing edge panels. Adding this term results in the following equation for a single streamwise strip of wake panels.

$$(\Delta\phi)_m^k = (\phi_m^{upper} - \phi_m^{lower})^k + (\mathbf{U} \cdot \mathbf{r}_{te})_m^k + K(\Delta C_p)_m^{(k-1)}, \quad (3.5)$$

where

$$K^n = K^{(n-1)} \frac{(\Delta C_p)^n}{(\Delta C_p)^{(n-1)} - (\Delta C_p)^n} \quad (3.6)$$

is iterated using the Newton-Raphson method until an equal pressure condition results at the foil's trailing edge.

Kerwin and Greeley [5] developed a fast, yet simple method of wake alignment which is employed in this code. Initially, the wake sheet is positioned such that it bisects the angle of attack of the hydrofoil and extends downstream without curvature. The velocities tend to be more singular when calculated directly at the panel edges, so the local velocities in the streamwise and vertical directions are calculated for the centroids of each interior wake panel. The influence of the foil, half body, and walls is obtained using the technique developed by Newman [15] (See Figure 3-3).

The influence of the wake sheet upon itself is more difficult to compute. Although Newman's technique might be employed, there are some hazards to applying it to the singular region about the tip vortex. Newman's method can calculate the velocities induced by a sheet of dipoles at the edges of the panels because an artificial, analytically obtained value is substituted in the subroutine for this otherwise unbounded point. However, unless the field point is positioned precisely on the panel's edge, an erroneously high magnitude of the velocity normal to the plane of the panel will result. Determining the exact position of the panel boundaries when wake contraction and wake alignment schemes are involved is particularly difficult. A constant dipole distribution over a panel surface is equivalent, mathematically, to placing discrete vortices on the four sides of the panel [13]. Since the wake sheet contains no source singularities, the difficulty of calculating the velocity at a panel's edge is alleviated by employing a vortex lattice velocity computation.

The lattice of the wake may be separated into three types of vortices. The first vortex filament is located at the trailing edge of the foil and is oriented in the same direction as the bound circulation on the foil, opposite of the starting vortex. Its strength is equal to and counters the difference in potential between the upper and lower trailing edge panels. It decreases in magnitude from the root to the tip of the foil, consistent with the spanwise circulation distribution.

The second portion of the lattice is formed by the discrete trailing vortices. Each trailing vortex is located at the streamwise edges of two adjacent strips of wake panels. Its strength is equated to the difference in vorticity of these two panel strips, considered constant in the streamwise direction of potential flow. In the limit of in-

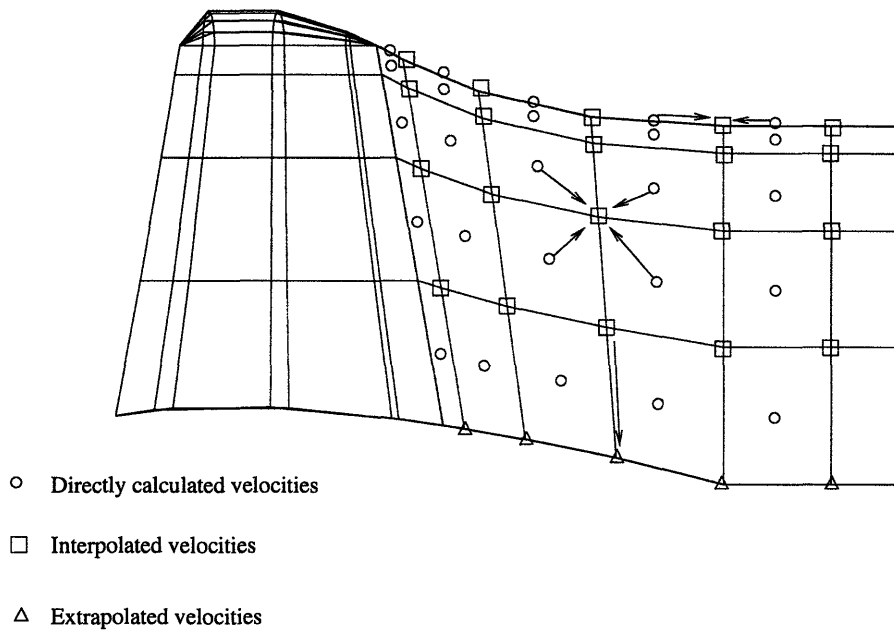


Figure 3-3: Interpolation scheme for aligning the wake panels

finite spanwise panelling, the strength of the trailing vortices becomes the derivative of the spanwise circulation distribution. By this methodology, the vortex associated with the inboard edge of the wake sheet is cancelled by the equal and opposite vortex on the other side of the half body centerline. The derivative of the circulation distribution should be zero at this midspan point.

The third vortex or tip vortex is a special case of the trailing vortices. Since it does not lie between two panels, its strength is given by the magnitude of vorticity of the panel located on the outboard edge of the wake only. Physically, it has the greatest strength, however, numerically, sometimes it is matched in size by the adjacent, inboard vortex, particularly in the limit of spanwise panels.

The magnitude of these velocities are interpolated bilinearly to determine the interior panels' nodal velocities (See Figure 3-3). The velocities associated with the inboard edge of the wake sheet, in contact with the tunnel wall, are linearly extrapolated from the adjacent two interior nodal points. The velocities induced on the tip vortex line are calculated directly, as discussed above, and merged with the previously calculated velocities of the interior panels.

Once the velocities at each of the wake panel nodes have been established, the ratio of the local downwash velocity w to the local streamwise velocity u plus the

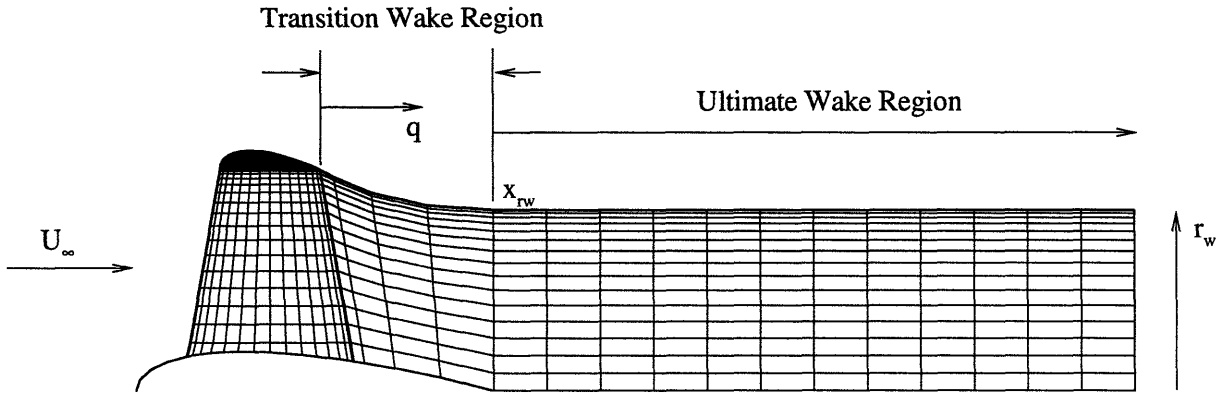


Figure 3-4: Plan view of wake panelling showing contraction ratio of 30 degrees

undisturbed inflow U , is compared to the existing pitch angle of that particular panel. If the two values differ, the pitch angle of the panel is adjusted to match that of the local flow velocity. After all the wake panels have been adjusted in this manner, the entire process of determining the influence coefficients of the geometry is repeated and again the local velocities at the wake are compared to the pitch angle of the individual panels. This iteration continues until the wake panels are aligned, within tolerance, with the local velocity vector.

Experimentation has shown that the tip vortex tends to sweep inboard slightly as it travels downstream (See Figure 3-4). Kerwin and Greeley [5] also developed an empirical estimate at the tip vortex contraction angle. They define the area downstream of the trailing edge of the foil where the wake is contracting as the transition wake region. Further downstream, where the spanwise width of the wake is constant, is defined as the ultimate wake region. Kerwin and Greeley developed an empirical equation which relates the ultimate wake spanwise position, r_w and the streamwise length of the transition region, x_{rw}

$$x_{rw} = \frac{3(r_t - r_w)}{\tan \delta_c} \quad (3.7)$$

where r_t is the spanwise origin of the tip vortex on the hydrofoil and δ_c is the contraction angle which is estimated or obtained from experimental data. In this case,

the length of the transition region is estimated to be the distance to the furthest point measured downstream by the LDV and r_w is also be obtained directly from the experimental results. The resulting contraction angle δ_c for a 5.36 degree angle of attack is approximately 12.4 degrees.

With these parameters defined, the shape of the tip vortex contraction may be estimated as a cubic polynomial, defining q as the fractional distance between the foil trailing edge and x_{r_w} and $r(q)$ as the spanwise position of the tip vortex in the transition region

$$r(q) = r_t + (r_t - r_w)(-3q + 3q^2 - q^3) \quad (3.8)$$

$$0 \leq q \leq 1$$

and

$$r = r_w$$

$$q > 1.$$

The discrete trailing vortices associated with the interior wake panel edges are uniformly distributed between the tip vortex and the half body profile as shown in Figure 3-4. Note that the half-cosine spacing of the semi-span hydrofoil tends to concentrate the wake panels near the tip, aiding in the simulation of the tip vortex roll-up process.

With the discretization of the basic integral equation of Chapter 2 and the geometry developed here, a potential flow estimation of the fluid behavior around a semi-span hydrofoil attached to a half body may be computed. Upon comparison with the experimental results, the model may undergo further revision to more accurately predict the flow patterns.

An important limitation of this code is that the wake panels are constrained to movement only in the vertical direction. They are not permitted to move spanwise, thereby preventing the panels from rolling up. This was done purely for simplicity. The detailed geometry of the tip vortex core is not modelled in this code, but future subroutines which can predict the vortex roll up may easily be appended.

Chapter 4

Experimentation

As described in Chapter 1, there is much interest in the generation of tip vortices and there have been numerous experiments conducted to study tip vortex behavior. Some recent studies of tip vortices associated with a single hydrofoil include Takahashi and McAlister [16], who used laser velocimetry to measure the airflow past a large, vertically oriented, NACA 0015 airfoil [1]. Lezius [14] implemented an alternative approach by using a water towing tank and 16-mm cameras to record the tip vortex behavior of a NACA 0015 foil at several angles of attack. Still other experimenters, such as Corsiglia [2], have used hot-wire anemometry to measure the flow field behind a NACA foil.

The present study used a semi-span NACA 0018/0012 foil affixed to a half body four digit NACA foil. A 3 Watt TSI argon-ion laser doppler velocimeter (LDV) measured the fluid behavior within the variable pressure water tunnel at the Marine Hydrodynamics Laboratory of the Massachusetts Institute of Technology (MIT). The objective of the experiment was to map the tip vortex behavior behind the semi-span hydrofoil.

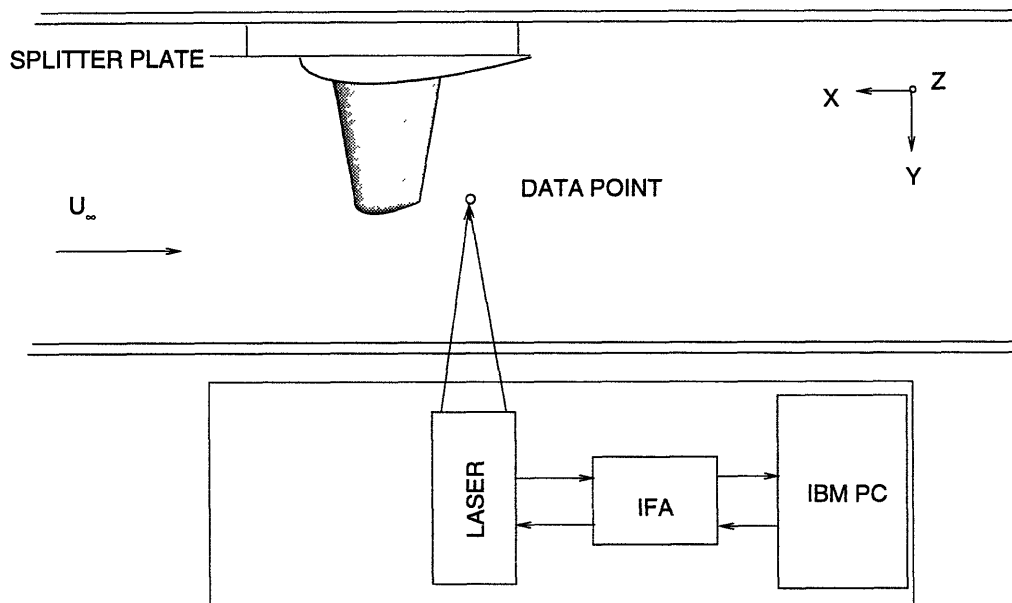


Figure 4-1: Schematic of tip-vortex experiment data flow

4.1 Apparatus

4.1.1 The water tunnel

The MIT water tunnel is a fresh water, closed-loop system which uses a 75 hp motor-driven impeller to produce steady flow of up to 30 feet per second through a 53-inch long, square test section. A honeycomb mesh is placed inside the 5:1 contraction section just upstream of the test section to regulate and condition the flow.

Each side of the test section is 20 inches in width and has four two-inch thick plexiglass windows which may be removed for installation of various models and equipment. The laser beams from the LDV penetrate one of these highly polished windows to extract velocity data (See Figure 4-1).

4.1.2 Laser Doppler Velocimeter

The LDV uses a pair of blue and a pair of green beams which are oriented in the horizontal and vertical planes with respect to the tunnel test section. The four separate beams are focused to a common point where the fluid velocity is measured. The

intersection of the beams creates a pattern of alternating intensities of laser light. Particles naturally present in the tunnel water augmented by 1 μm diameter silicon carbide particles entrained in the fluid scatters the light at a frequency which is proportional to its velocity in the direction normal to the fringes, in this case, the vertical and streamwise directions. The scattered light is collected by photo-multipliers associated with each pair of laser beams. The MIT system is a “back-scatter” system, meaning that the light is reflected back towards the source of the beams.

Digital Intelligent Flow Analyzers (IFA’s) receive data from the photomultipliers and process them so that they can be read by the 20 MHz 386 PC. The IFA’s analyze the flow and discard data which are invalid. Errors may arise due to spurious signals in the processing system. The PC’s data-reduction software keeps the laser focused at a single point until the prescribed number of samples has been obtained, generally on the order of 250-300. The ensemble is averaged and the standard deviations are calculated. The output consists of average velocities and a relative measurement of turbulence intensity for the given field point. A 1992 study of the MIT water tunnel compared LDV turbulence data to that measured by hot wire anemometry for various Reynold’s numbers. The results are shown in Figure 4-2. The hot film probe data were taken with a TSI conical hot film probe, model 1231W. Vertical and horizontal lines of data were taken across the test section intersecting at the center, approximately five cm downstream of where the trailing edge of the hydrofoil would be located. Turbulence intensity in Figure 4-2 is defined as

$$TI = \frac{100}{U_0} \left[\frac{1}{N-1} \sum_i^N (u_i - \bar{u})^2 \right]^{\frac{1}{2}} \quad (4.1)$$

where U_0 is the freestream velocity, U_i is the instantaneous measured streamwise velocity, \bar{u} is the mean streamwise velocity, and N is the number of sampled points. The current experiment operated at a Reynold’s number of approximately 1.5×10^6 .

The LDV is mounted on a computer-controlled three-axis table. The table may be positioned within five microns, however, the control system is only accurate to within 0.01 mm. The data collection system of the LDV is linked to the same computer

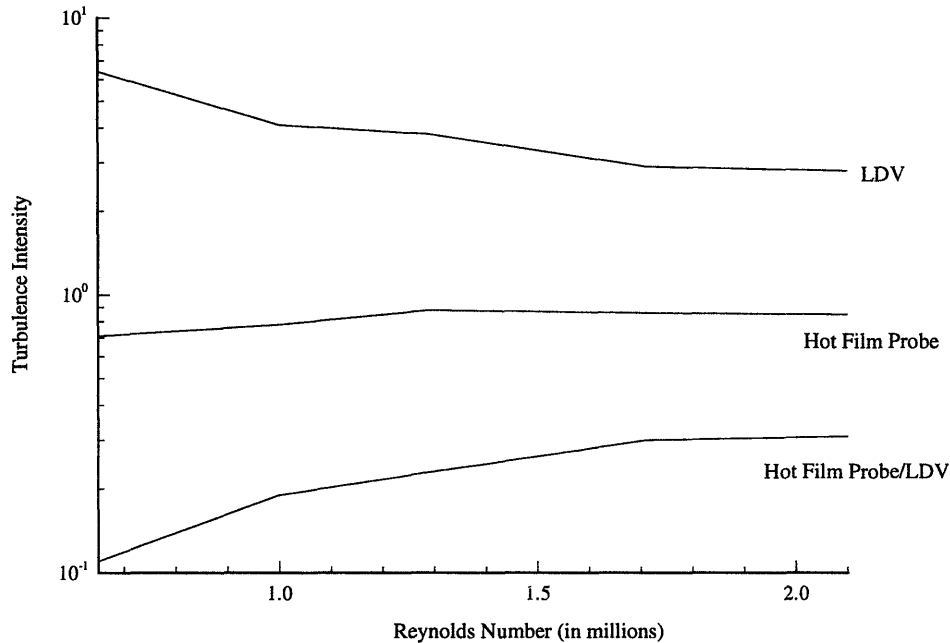


Figure 4-2: Percent turbulence for LDV and hot-wire measurements in water tunnel

as the table thus allowing the flow measurements to be automated. The range of the laser is limited due to laser-beam blockage, either by the edge of the plexiglass windows or by of the semi-span foil itself.

To non-dimensionalize the LDV output, a differential pressure (DP) transducer is located in the contraction section of the water tunnel. The DP cell tracks the mean velocity through the test section and allows variation in the flow rate to be eliminated from the LDV results.

Both the water tunnel and the LDV are described by Kerwin [9] and Coney [4] in greater detail.

4.1.3 Model description

The half body and semi-span used in this experiment were built by Coney [4] specifically for use inside the MIT water tunnel. The plexiglass model was mounted to an aluminum splitter plate which located the assembly 2 inches further into the center of the test section and allowed the developed boundary layer along the tunnel wall

to pass underneath the half body. The splitter plate was also designed such that it created an image plane effectively generating a symmetric configuration.

The half body profile matches a 4-digit NACA airfoil. It has a chord length of 16 inches and a span of 19.5 inches for ease of installation. The span of the half body did not extend the full height of the tunnel test section as modelled by the panel code. The maximum thickness to chord ratio is 0.2215. It has rounded corners of 1.75 inch radii. The semi-span is mounted to the half body by a 1.5 inch diameter steel shaft which is located at approximately the 28 percent chord point of the half body. This shaft allowed the semi-span to be adjusted to various angles of attack.

The hydrofoil has a span length of 8.06 inches. The root profile is that of a NACA 0018 foil with a 7.5 inch chord. The nominal tip is described by a NACA 0012 foil with a 4.905 inch chord. The actual tip is a half body of revolution whose diameter at each chordwise position matches the NACA 0012 profile. The steel shaft is inserted into the semi-span at the quarter chord point. The leading edge sweep angle is 9.23 degrees and the mean chord length is 6.2 inches.

There is fairing which matches the root profile of the semi-span foil, affixed to the half body. The span of the fairing was fabricated such that it did not extend beyond the maximum thickness of the half body. The fairing prevented a gap from forming between the semi-span and the half body. The computer model does not reflect this fixed angle fairing.

Turbulence stimulators 0.008 inches high were placed 0.1 inches apart spanwise along the 20 percent chord position, top and bottom. The positioning of the turbulence inducers was derived using a boundary layer code that predicted a displacement thickness of 0.008 inches at that location. No turbulence stimulators were placed on the half body.

4.2 Experimental Procedure

4.2.1 Test Conditions

The freestream velocity was set at 24 feet/sec and the average water temperature during the data collection was 80 degrees Fahrenheit, corresponding to a Reynold's number of approximately 1.5×10^6 with Reynold's number defined as

$$Re = \frac{U c_{mean}}{\nu} \quad (4.2)$$

where U is the freestream velocity, c_{mean} is the mean chord length, and ν is the kinematic viscosity of the water at 80 degrees. The splitter plate extends 7 inches forward of the leading edge of the half body. The turbulent boundary layer thickness due to the splitter plate is estimated using the $\frac{1}{7}$ th power law at 0.153 inches or about 73 percent of the fairing span.

4.2.2 Coordinate system

The coordinate directions of the laser control system are permanently established with the exception of the selection of the origin. The origin was selected to be at the outermost tip of the trailing edge of the semi-span hydrofoil. This allowed the laser to be realigned reliably and easily by direct observation on a repeatable basis. The x-axis is aligned opposite the freestream velocity vector. The y-axis is oriented such that it points outboard from the origin, away from the root of the semi-span. Using a right-hand convention, the z-axis is directed upward. A positive angle of attack is defined with the leading edge displacement upward (positive z).

Unfortunately the computer model of the experiment developed depicting the starboard side of the configuration and the direction of the y axis is reversed in the global sense, but remains pointing outboard. The z axis remains upward and the positive x direction is downstream. All of the comparisons of the results in Chapter 5 are corrected for this discrepancy.

The angle of attack was measured by several devices. Initially, the laser marked

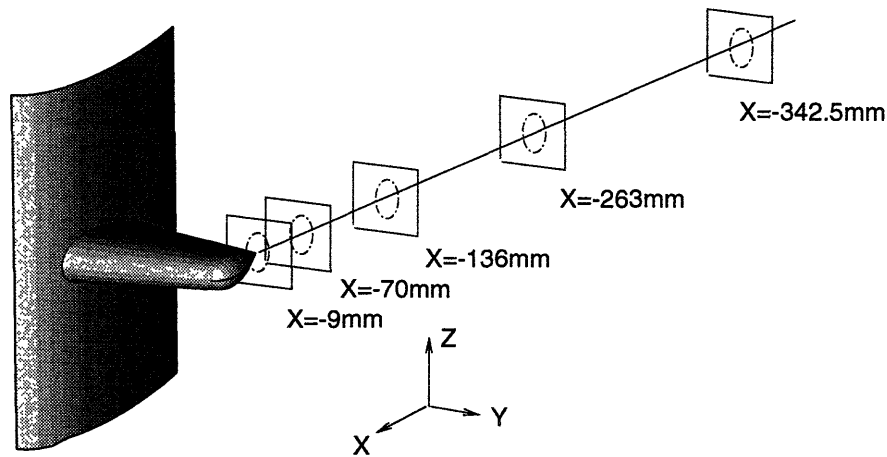


Figure 4-3: Velocity measurement grids for hydroplane in side configuration

the coordinates of the leading edge and the trailing edge, maintaining the laser's y position constant and the angle of attack was determined by the arctangent of the difference of the two coordinates. Additionally, the leading and trailing edges were measured relative to the tunnel walls using a caliper and the chord of the foil was measured at the same spanwise location. The two results were consistent. Once defined, the same angle of attack could be obtained repeatedly by a shaft encoder affixed to the stainless steel shaft of the semi-span foil. Also, the lift, measured by a dynamometer attached to the shaft, uniquely defines the angle of attack.

4.2.3 Velocity Measurements

The semi-span hydrofoil was set at a specific angle of attack, either positive or negative 5.36 degrees. The ambient pressure in the tunnel was reduced to a point where the tip vortex could easily be seen and its coordinates mapped out by the LDV. Five streamwise locations were chosen to measure the region about the tip vortex, specifically at 9 mm, 70 mm, 136 mm, 263 mm and 342.5 mm downstream from the origin (see Figure 4-3). This corresponds to x/Span coordinates of 0.044, 0.34, 0.66,

1.28 and 1.67, respectively. At each of these locations a grid of data points, 100 mm on a side, was measured by the LDV in a plane oriented normal to the longitudinal axis of the tunnel (See Figure 4-3). Initially the grid consisted of a coarse spacing of 5 mm. This allowed the fine grid of 0.5 mm spacing to be accurately positioned to obtain the maximum amount of information about the tip vortex.

Another grid of data was measured one half of the mean chord forward of the foil to record the inflow profile. To supplement this measurement, a single line of velocities was measured from the upper extreme to the lower extreme of the tunnel at the one half span position, limited by the laser interference with the frame of the tunnel. A line of data was also measured spanwise, at a height equal to the vertical position of the foil.

The time it took for the velocity at each point to be recorded varied from 15 seconds to several minutes. The sample time corresponded to the amount of turbulence in the region. The time necessary to complete one grid could thus vary from two to more than six hours.

As noted above, only two components of velocity could be measured at any point. To complete the study and obtain the third component, the entire assembly was rotated 90 degrees and placed in the top of the tunnel. This allowed the LDV to measure the y component of the velocity vector and use the x component to compare with the original orientation for consistency between measurements.

4.3 Experimental Results

The baseline measurement of variations in the inflow velocity field is shown in Figures 4-4 and 4-5. The grid was measured one half of the mean chord length forward of the foil. The standard deviations for the streamwise and spanwise velocities are presented in Figures 4-6 and 4-7.

Figures 4-8 and 4-9 show the results of the two one-dimensional traverses across the test section of the tunnel in the vertical and spanwise directions, respectively. Both lines were taken one half of a mean chord length forward of the leading edge

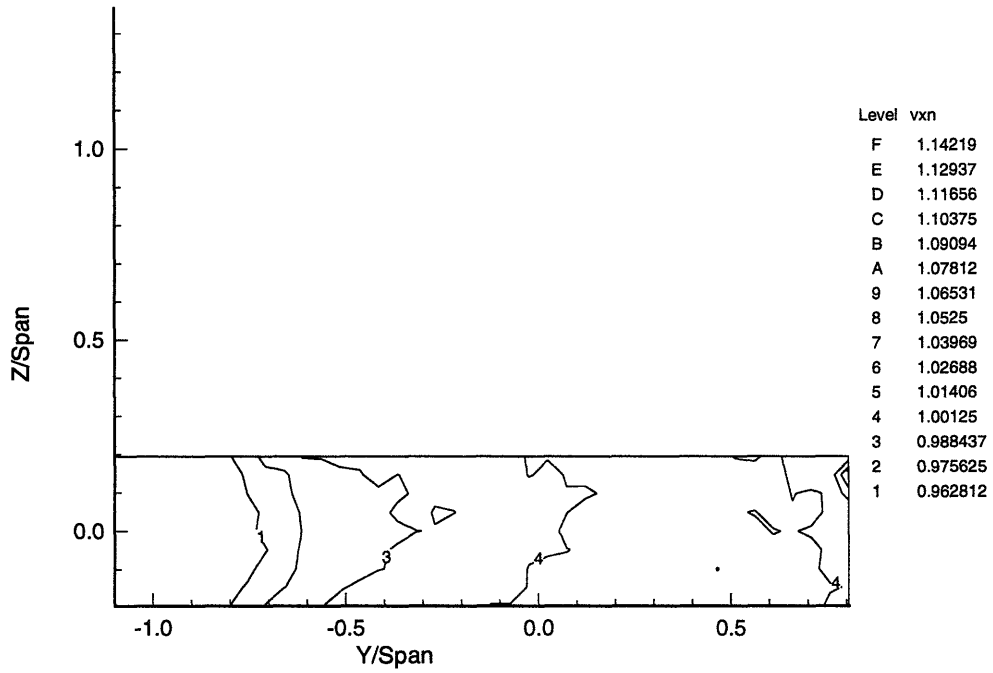


Figure 4-4: Streamwise velocity of inflow at $X/Span = +1.06$. (coarse grid).

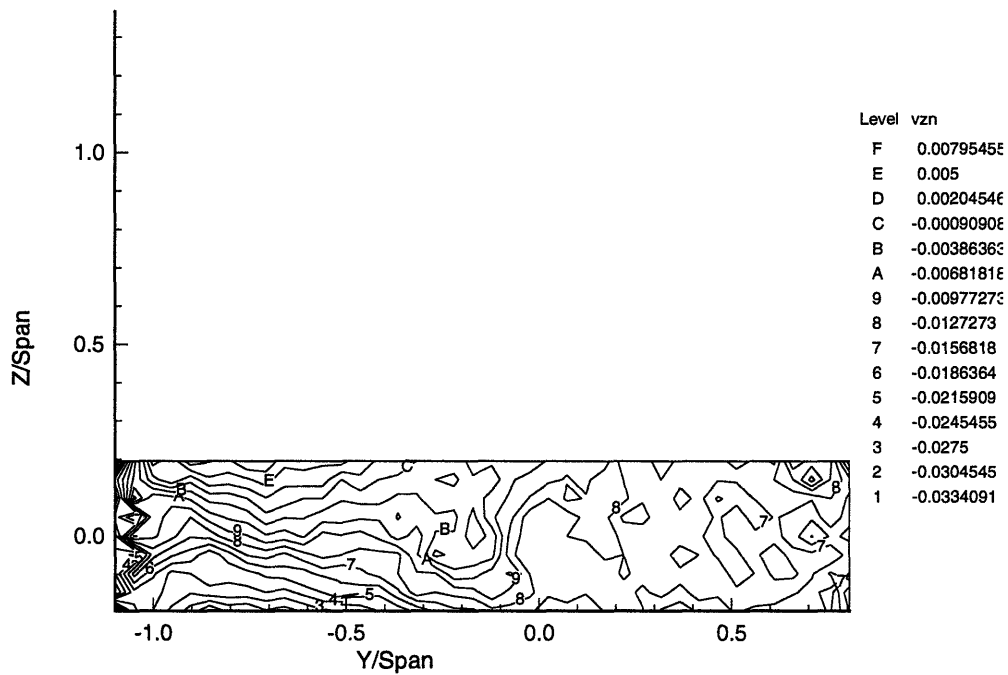


Figure 4-5: Vertical velocity of inflow at $X/Span = +1.06$. (coarse grid).

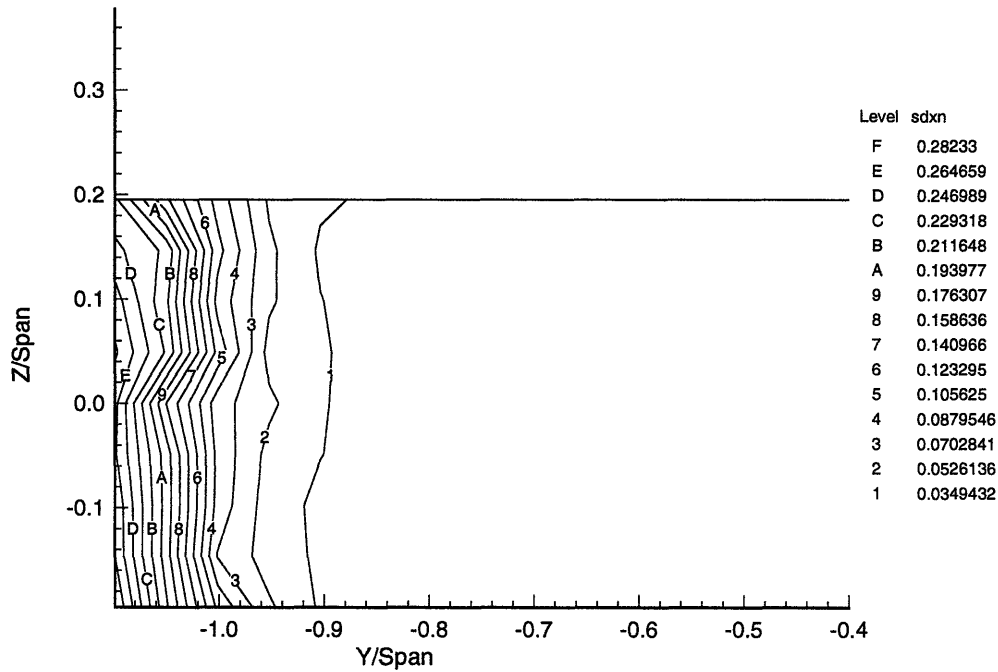


Figure 4-6: Standard deviation of streamwise velocity of inflow at $X/Span = +1.06$. (coarse grid).

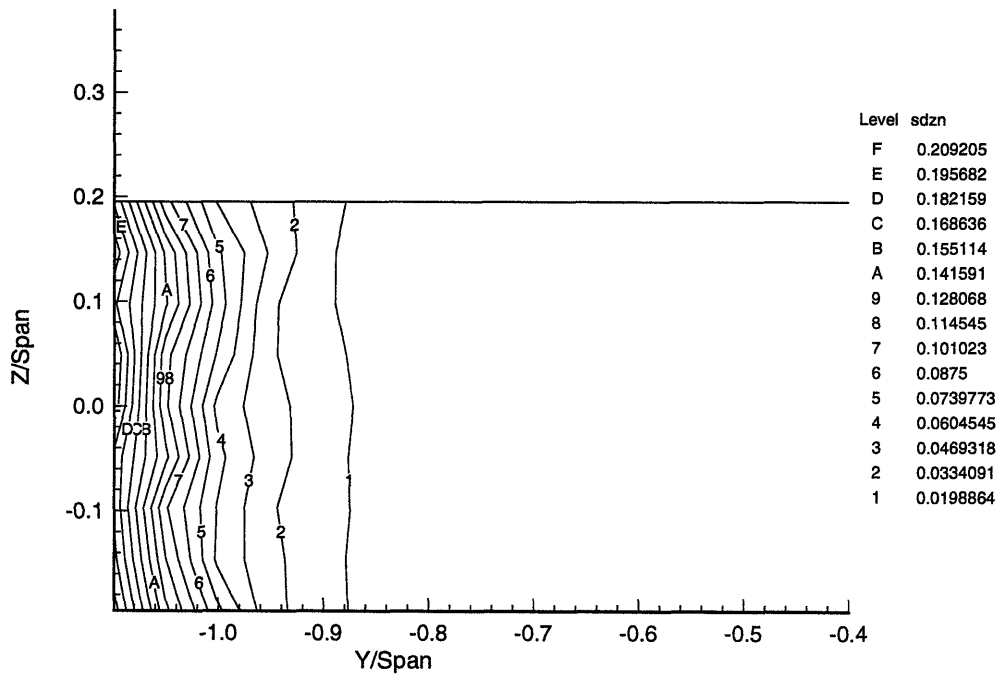


Figure 4-7: Standard deviation of vertical velocity of inflow at $X/Span = +1.06$. (coarse grid).

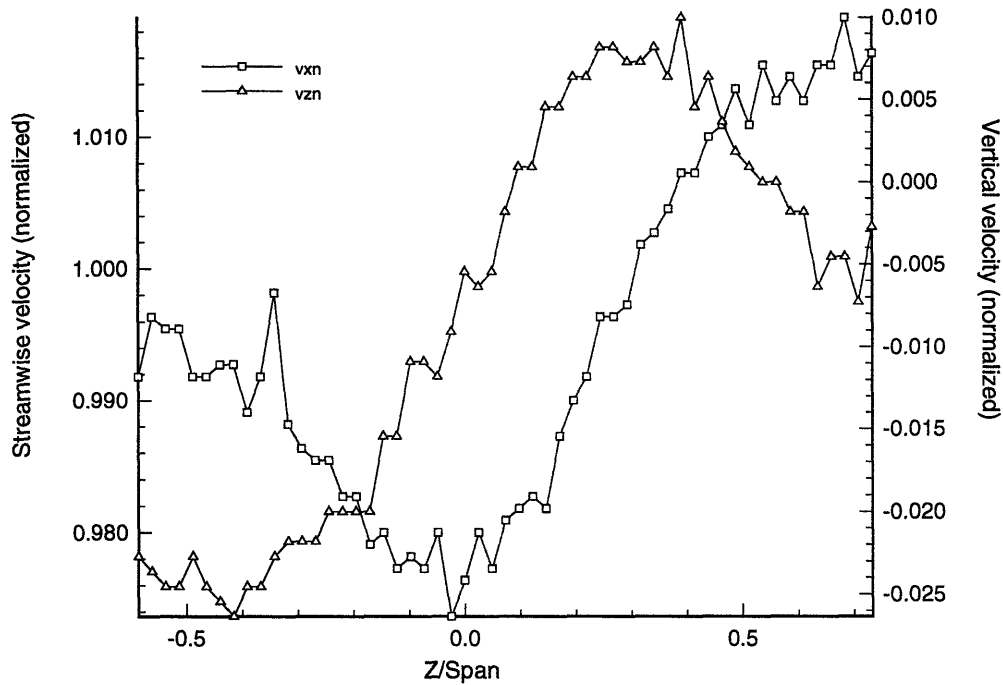


Figure 4-8: Velocities from vertical traverse of test section at $X/\text{Span} = +1.06$. (coarse grid).

of the hydrofoil. Note in the spanwise plot that the tunnel-wall boundary layer is distinctly visible on the left side of Figures 4-4 and 4-9. The standard deviations associated with these inflow velocities are shown in Figure 4-10.

The velocity data between the side orientation of the assembly and the top orientation were checked for consistency and merged to obtain all three components of the fluid's velocity. All the values were normalized to the magnitude of the steady stream velocity measured by the differential pressure cell. The freestream velocity as measured by the anemometer was approximately 90 percent of that measured by the LDV.

Figures 4-11 through 4-15 show the hydrofoil's wake deficit as it changes in the downstream direction. Note the shape of the wake can be visualized through the wake deficit. The tip vortex can be seen distinctly separating from the remainder of the wake and moving slightly inboard and upward as it travels downstream. The upward motion of the tip vortex in the near field will be checked as the wake sheet rolls up into two concentrated tip vortices further downstream; the downwash associated with one

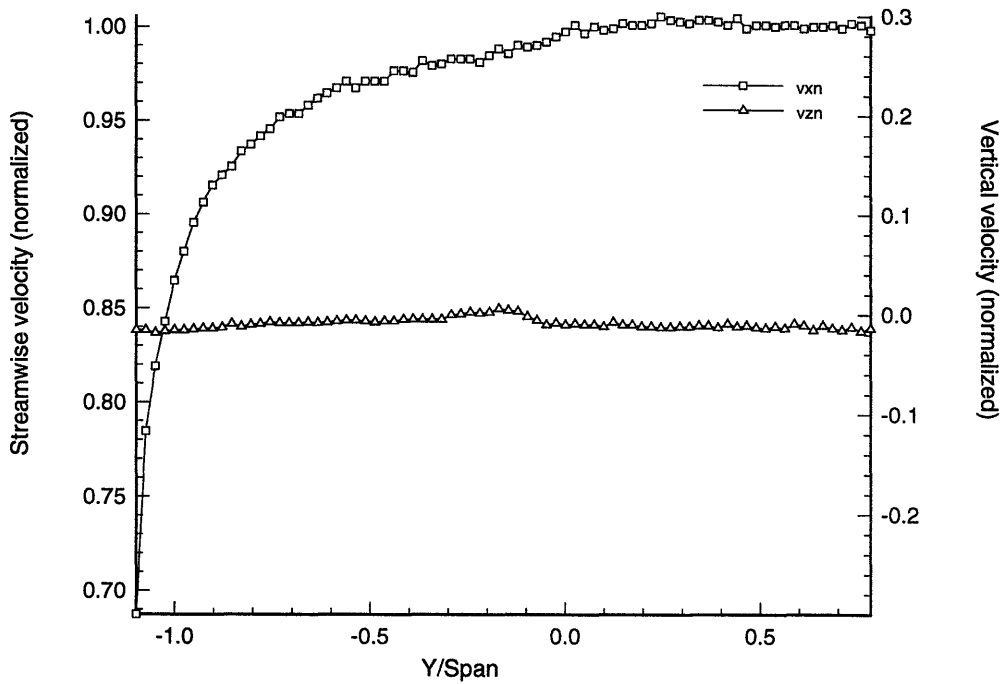


Figure 4-9: Velocities from spanwise traverse of test section at $X/Span = +1.06$. (coarse grid).

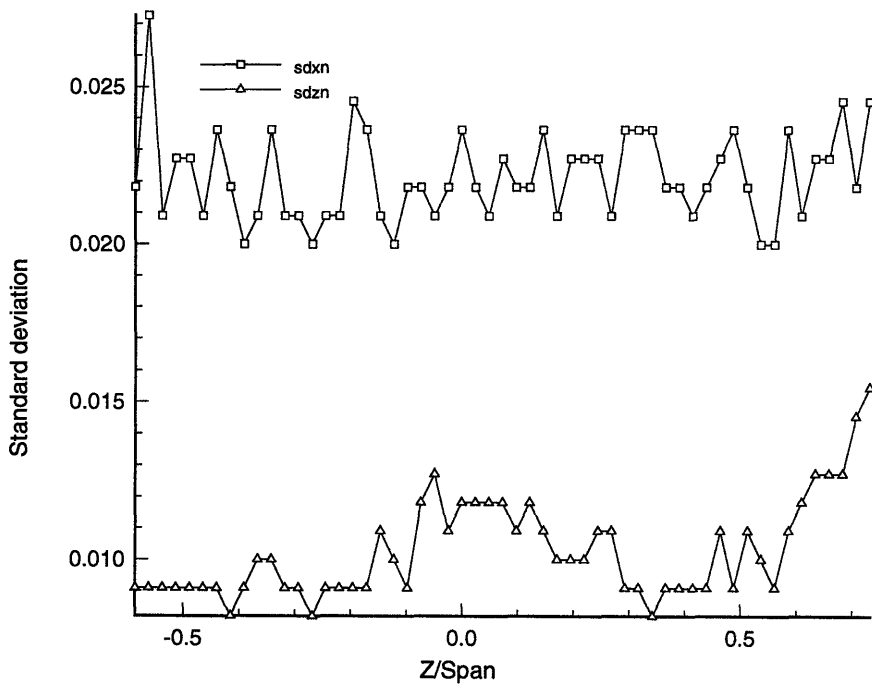


Figure 4-10: Standard deviations of velocities of vertical traverse of test section at $X/Span = +1.06$ mm. (coarse grid).

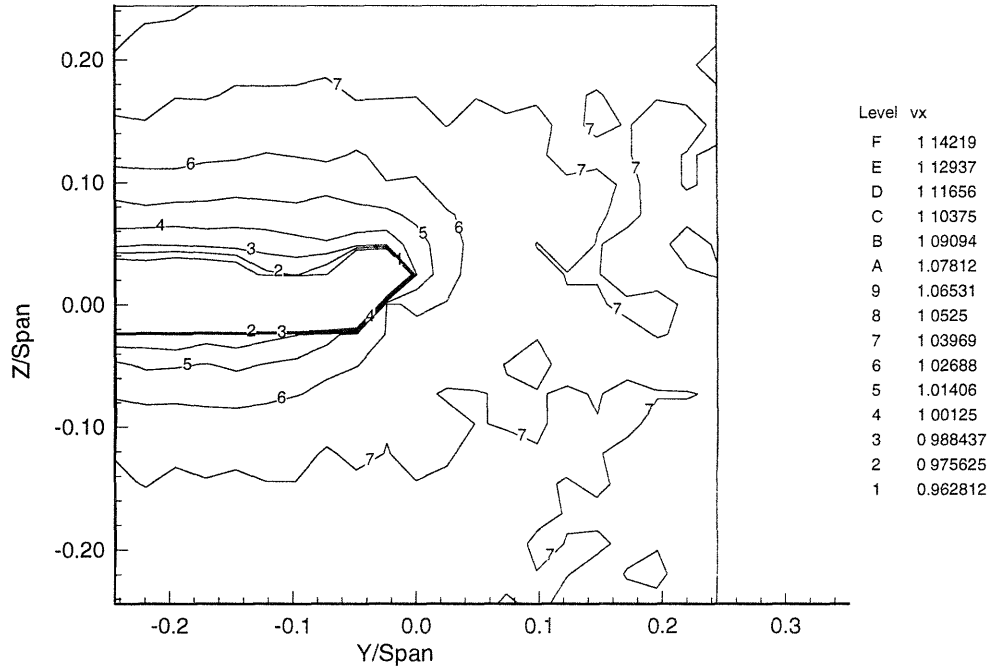


Figure 4-11: Streamwise velocity at $X/Span = -0.044$. Angle of attack is $+5.36$ degrees (side orientation/coarse grid).

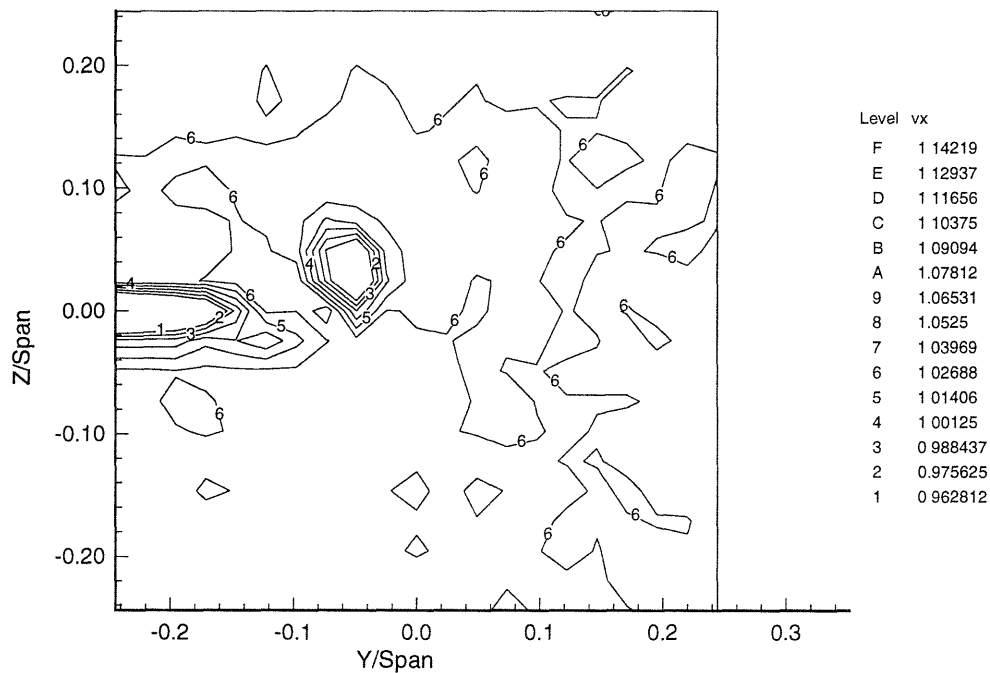


Figure 4-12: Streamwise velocity at $X/Span = -0.34$. Angle of attack is $+5.36$ degrees (side orientation/coarse grid).

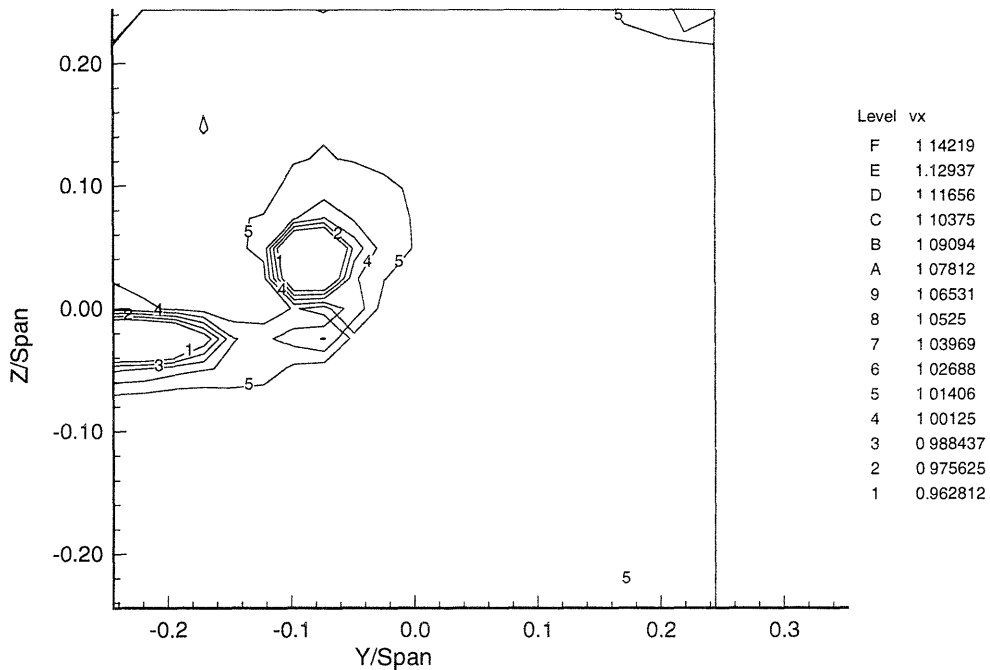


Figure 4-13: Streamwise velocity at $X/Span = -0.66$. Angle of attack is $+5.36$ degrees (side orientation/coarse grid).

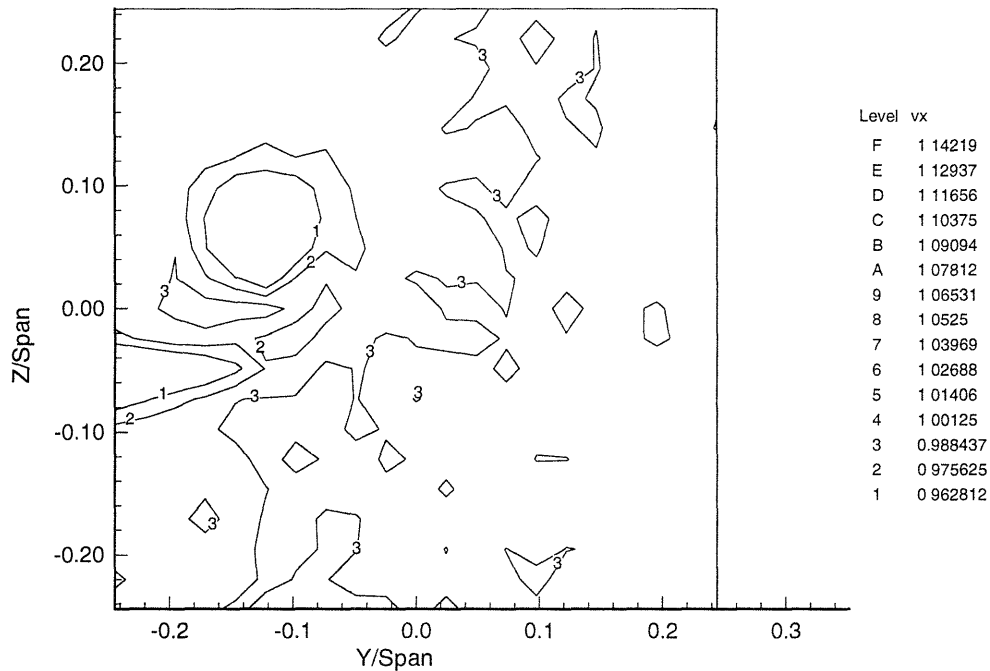


Figure 4-14: Streamwise velocity at $X/Span = -1.28$. Angle of attack is $+5.36$ degrees (side orientation/coarse grid).

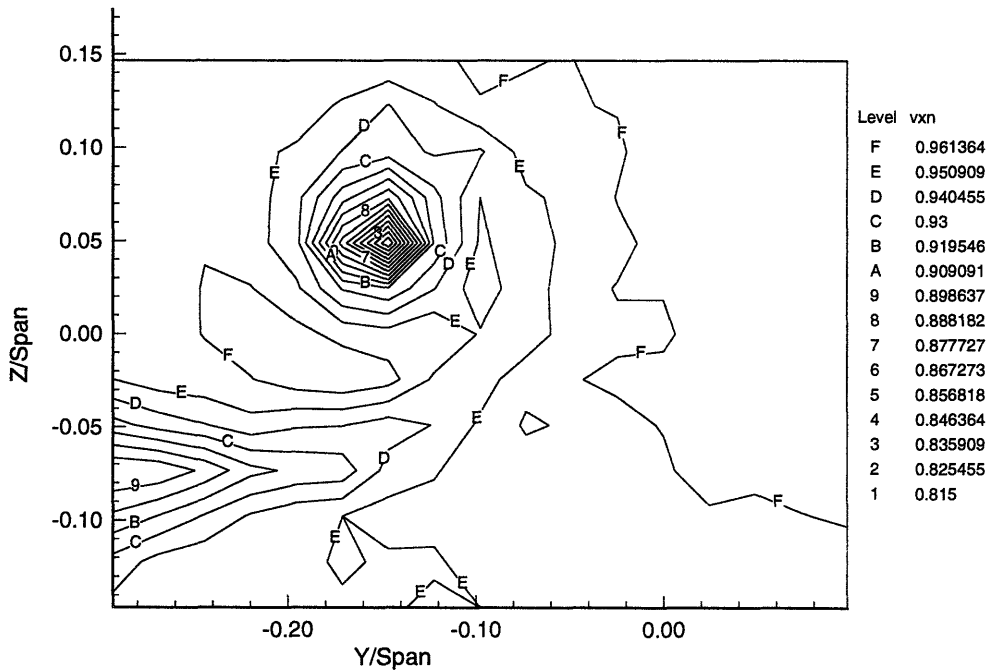


Figure 4-15: Streamwise velocity at $X/\text{Span} = -1.67$. Angle of attack is $+5.36$ degrees (side orientation/coarse grid).

concentrated tip vortex will influence the other [11]. The LDV measurements taken in this survey were limited to a few spanlengths downstream which precluded observing the fully developed path of the tip vortex. Takahashi and McAlister [16] also show the vertical rise in the tip vortex in their LDV measurements of a NACA 0015 airfoil, but their results also only take near field effects into account.

The true workings of the tip vortex are better seen by examining the vertical and spanwise velocity components. Figures 4-16 through 4-20 map out the vertical velocity of the tip vortex as it travels downstream and figures 4-21 through 4-23 show the spanwise component of velocity. As described above, the vertical velocity was extracted with the foil in the side configuration and the spanwise velocity was obtained using the top configuration. In the plots that follow, however, the grid has been rotated so that all velocity components are shown for the side orientation.

After the vertical and spanwise velocities were merged, a numerical approximation of the vorticity was computed using a five-point Eulerian scheme. Figures 4-24 to 4-25 show the results.

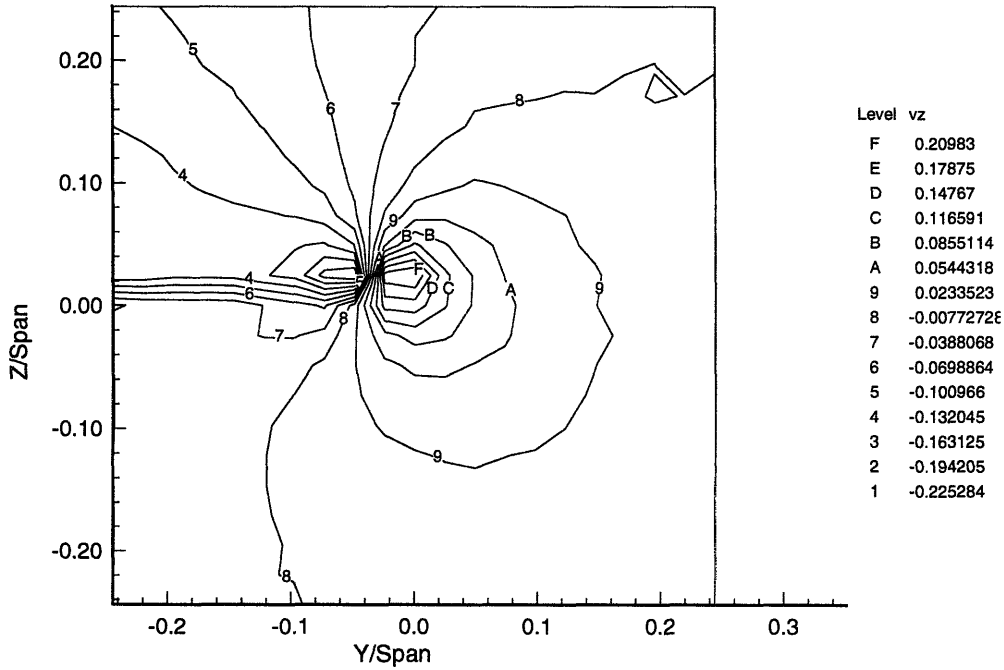


Figure 4-16: Vertical velocity at $X/Span = -0.044$. Angle of attack is $+5.36$ degrees (side orientation/coarse grid).

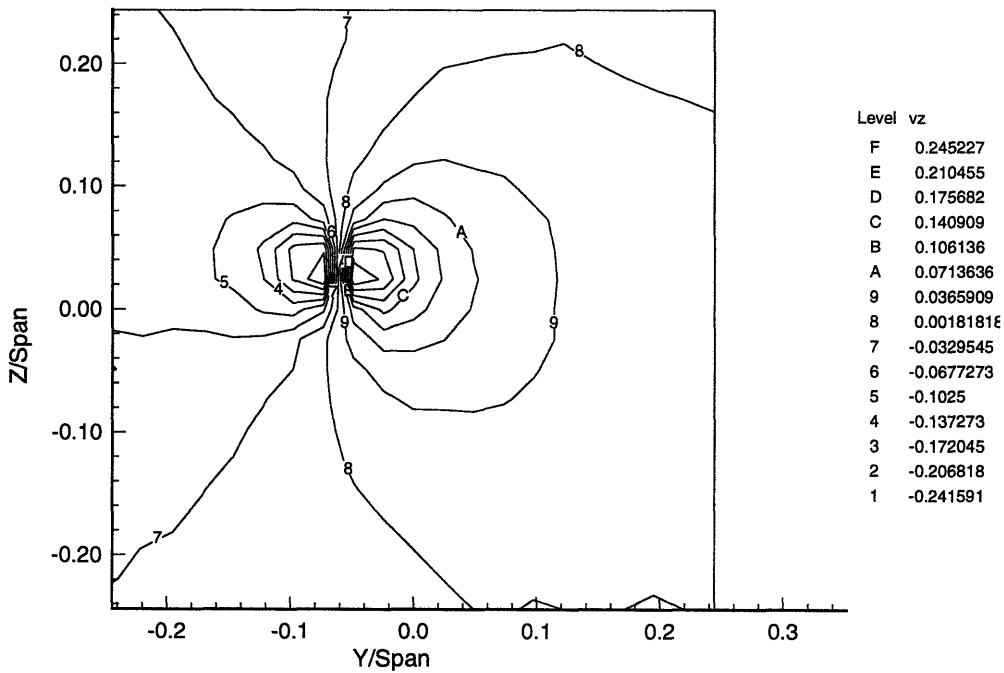


Figure 4-17: Vertical velocity at $X/Span = -0.34$. Angle of attack is $+5.36$ degrees (side orientation/coarse grid).

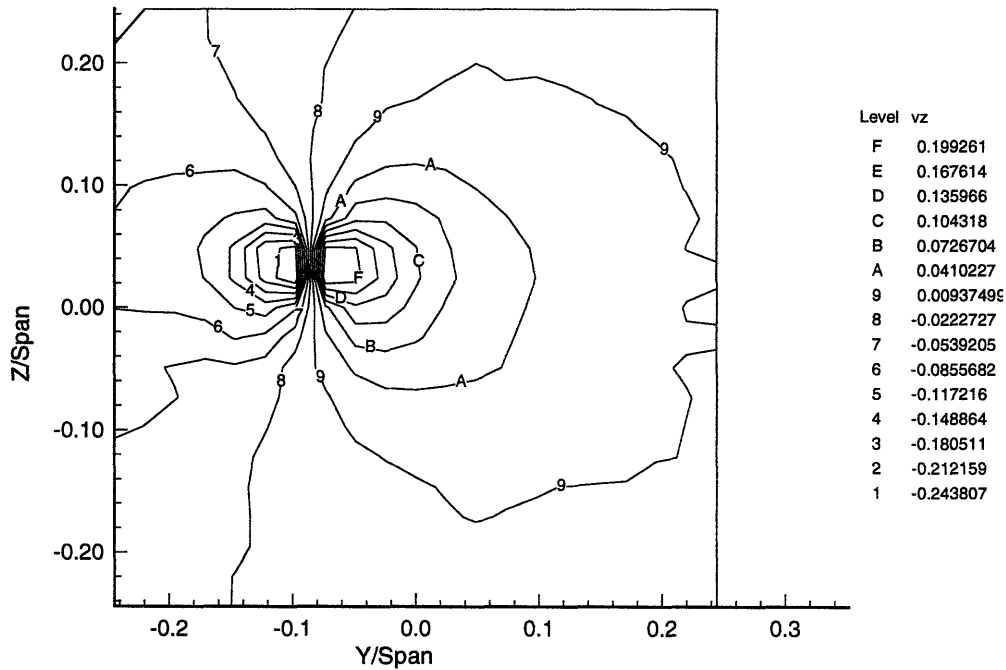


Figure 4-18: Vertical velocity at $X/Span = -0.66$. Angle of attack is $+5.36$ degrees (side orientation/coarse grid).

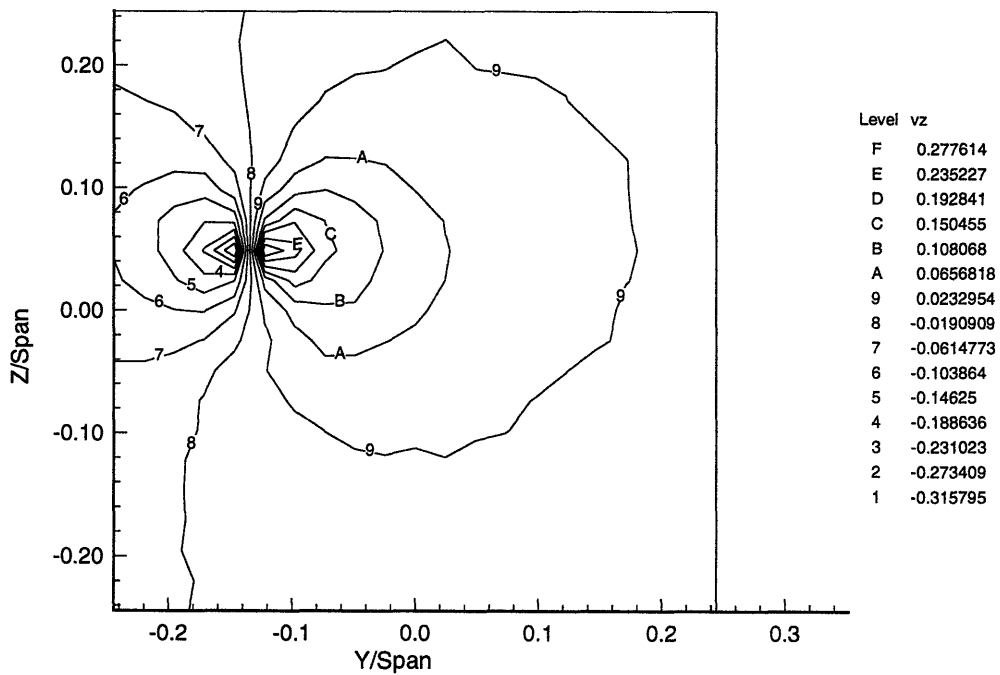


Figure 4-19: Vertical velocity at $X/Span = -1.28$. Angle of attack is $+5.36$ degrees (side orientation/coarse grid).

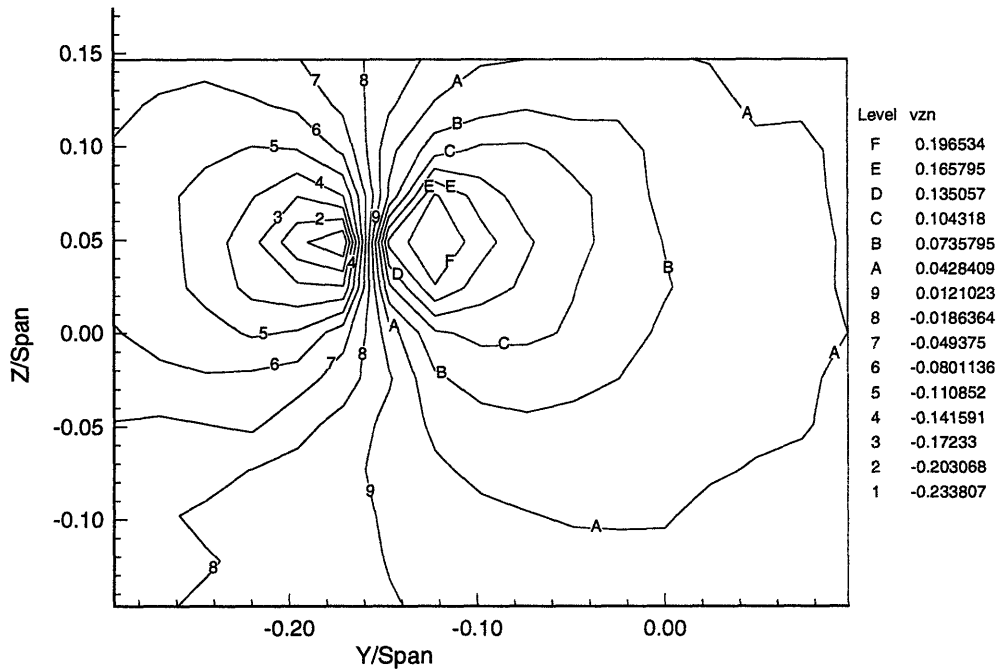


Figure 4-20: Vertical velocity at $X/Span = -1.67$. Angle of attack is $+5.36$ degrees (side orientation/coarse grid).

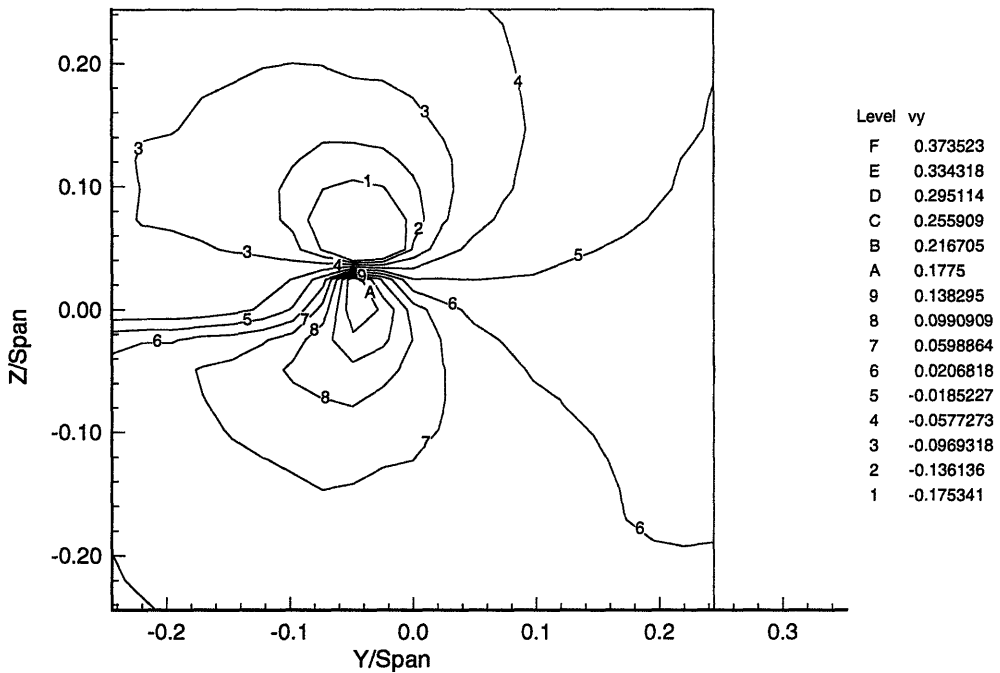


Figure 4-21: Spanwise velocity at $X/Span = -0.34$. Angle of attack is $+5.36$ degrees (top orientation/coarse grid).

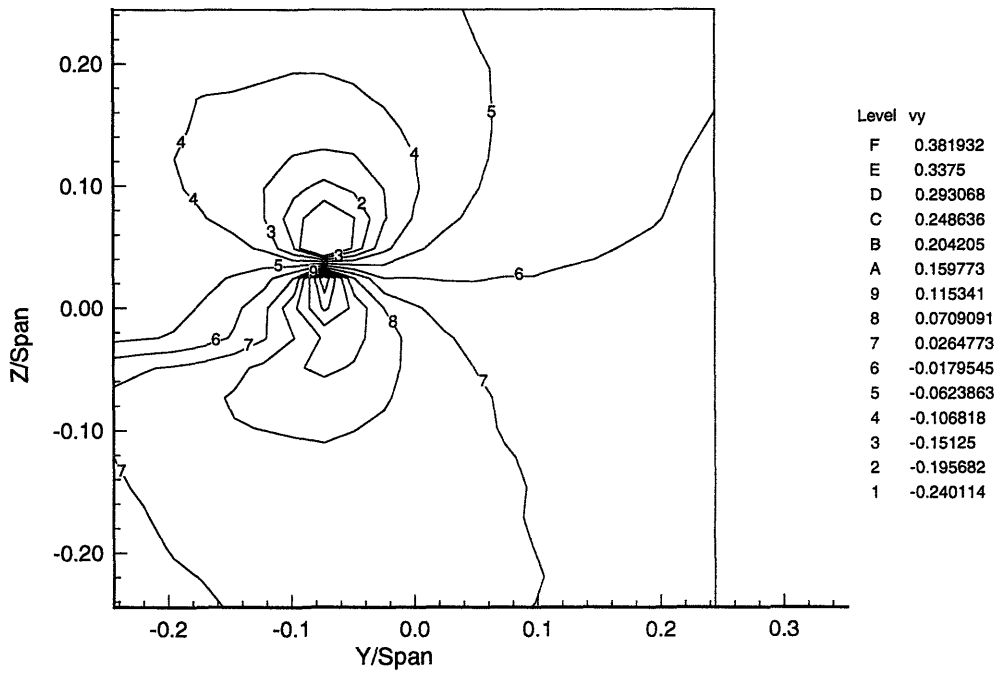


Figure 4-22: Spanwise velocity at $X/Span = -0.66$. Angle of attack is $+5.36$ degrees (top orientation/coarse grid).

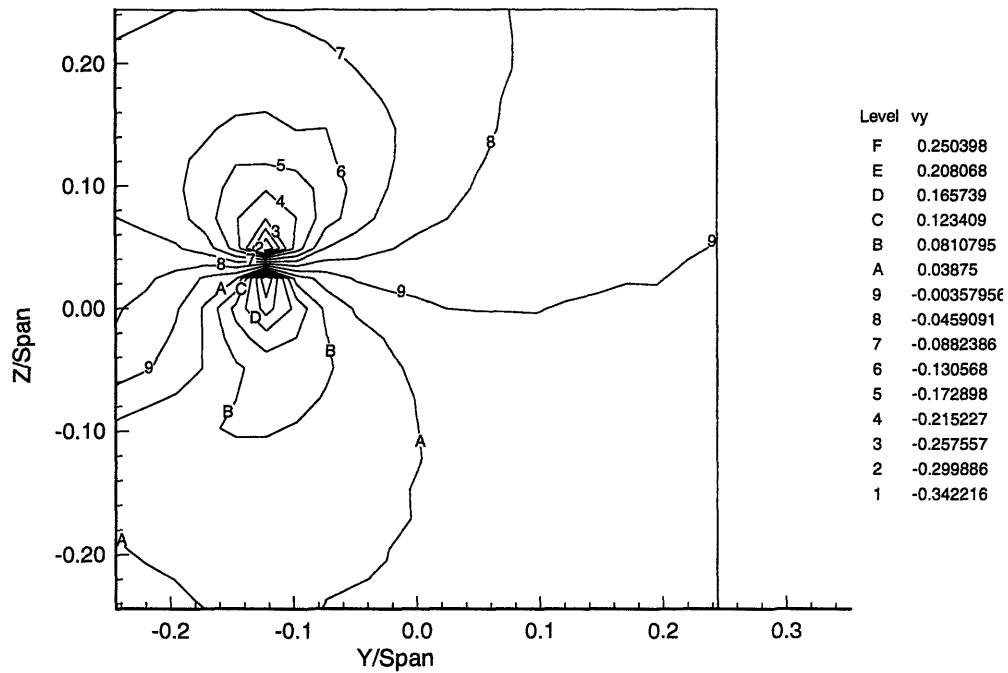


Figure 4-23: Spanwise velocity at $X/Span = -1.28$. Angle of attack is $+5.36$ degrees (top orientation/coarse grid).

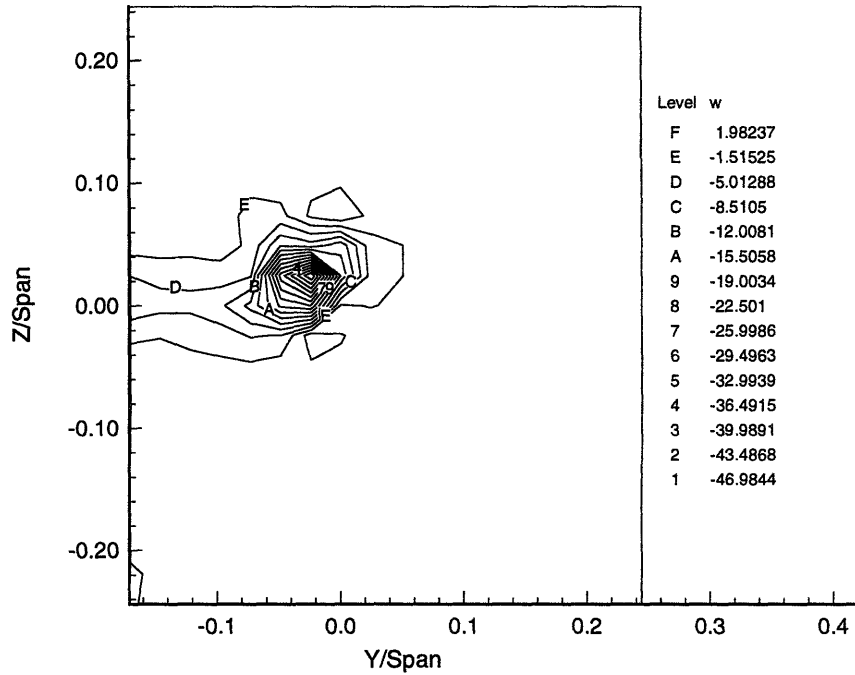


Figure 4-24: Axial vorticity at $X/Span = -0.044$. Angle of attack is $+5.36$ degrees (coarse grid).

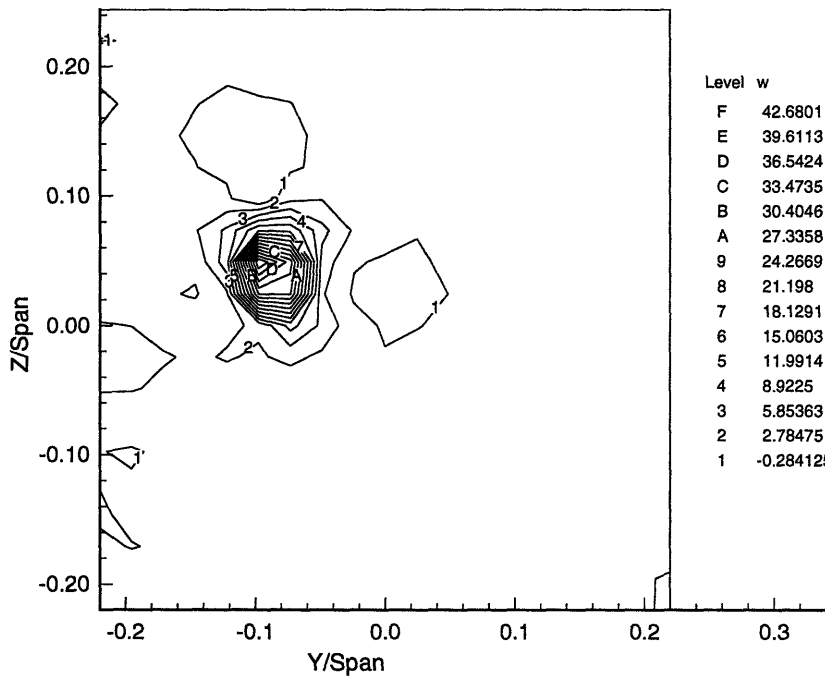


Figure 4-25: Axial vorticity at $X/Span = -0.66$. Angle of attack is $+5.36$ degrees (coarse grid).

During the second phase of testing there was insufficient time to shift the assembly to the top orientation, therefore vorticities could not be calculated because spanwise velocity components were not obtained. However, the hydrofoil was positioned to a -5.36 degree angle of attack and a set of velocity profiles were measured. Figures 4-26 through 4-29 show some of the results. Note the symmetry of the model is reflected when comparing these plots to figures of the positive angle of attack above.

For more precise validation of the computer code and to study the effects of vortex core wandering, a detailed mapping of the tip vortex core was performed. At this level of detail the effects of time averaging the samples are more significant. The vortex core wanders in a random motion about a mean longitudinal line. This causes the contour plots of the core size and geometry to appear larger and more symmetric than might actually be the case for a snapshot in time. Figures 4-30 through 4-37 show the detailed view of the tip vortex core using a fine grid of 0.5 mm spacing between sampling points. Detailed mapping of the vortex was also attempted at the planes furthest downstream, but the data rate was so reduced that it became infeasible to obtain an accurate plot.

Standard deviations calculated for the velocities presented in this chapter are included in the appendix.

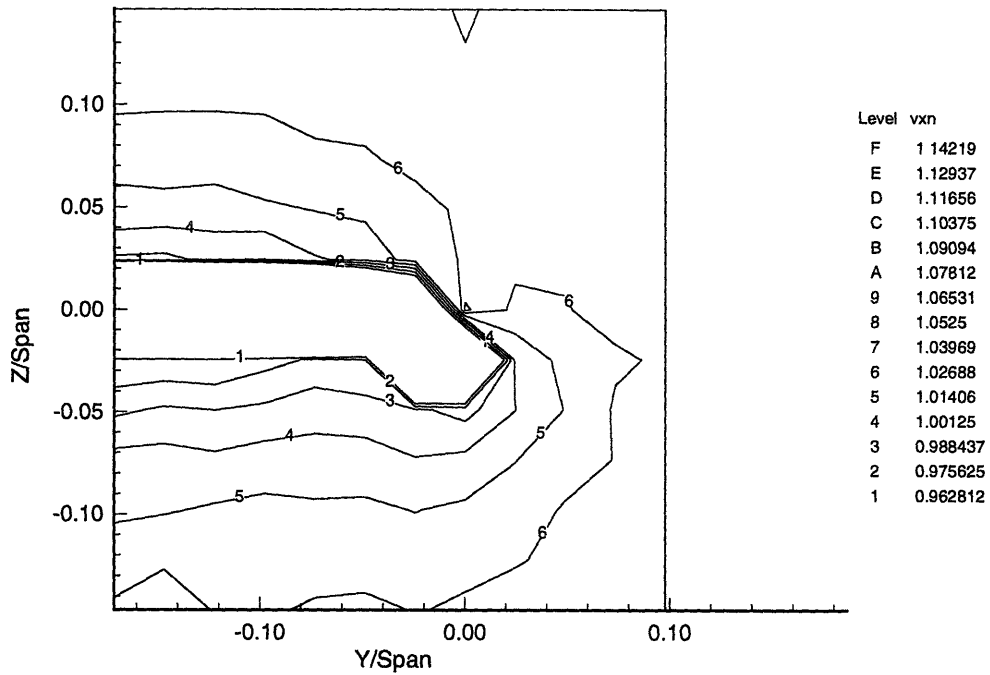


Figure 4-26: Streamwise velocity at $X/Span = -0.044$. Angle of attack is -5.36 degrees (side orientation/coarse grid).

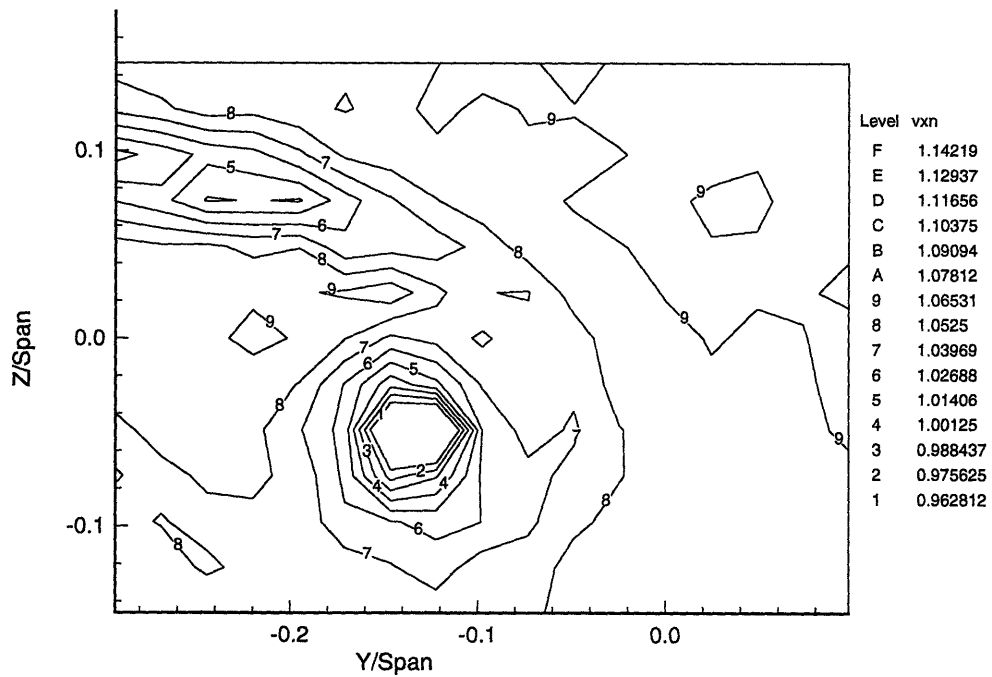


Figure 4-27: Streamwise velocity at $X/Span = -1.67$. Angle of attack is -5.36 degrees (side orientation/coarse grid).

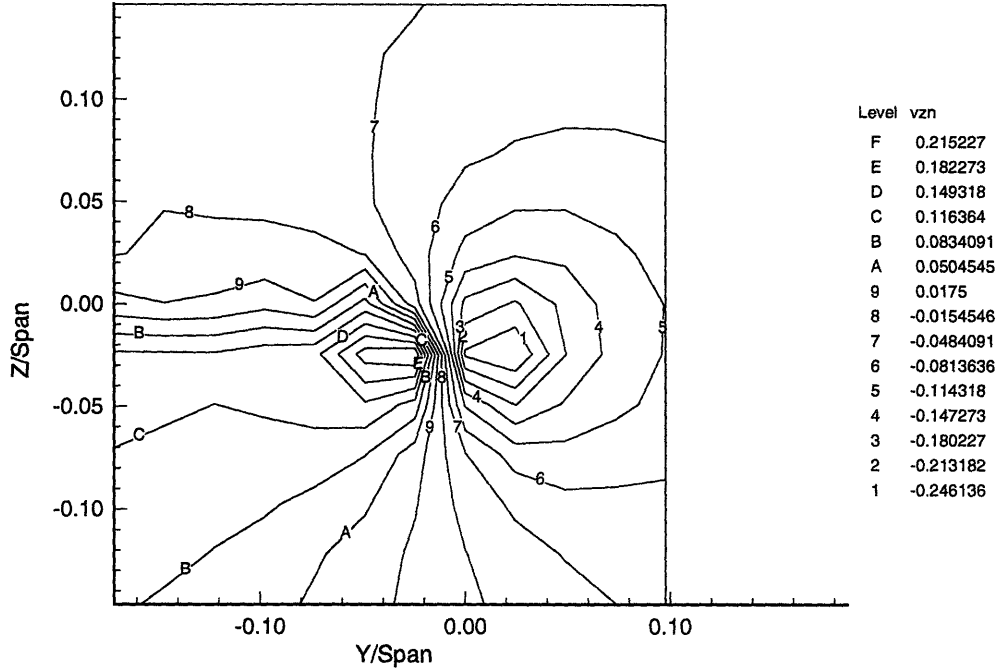


Figure 4-28: Vertical velocity at $X/Span = -0.044$. Angle of attack is -5.36 degrees (side orientation/coarse grid).

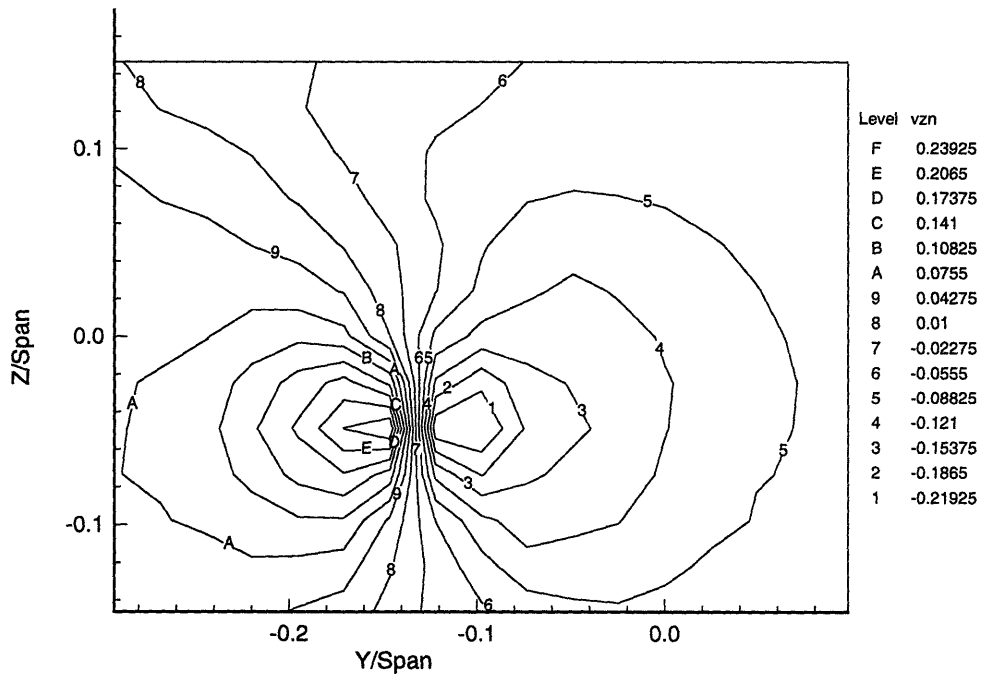


Figure 4-29: Vertical velocity at $X/Span = -1.67$. Angle of attack is -5.36 degrees (side orientation/coarse grid).

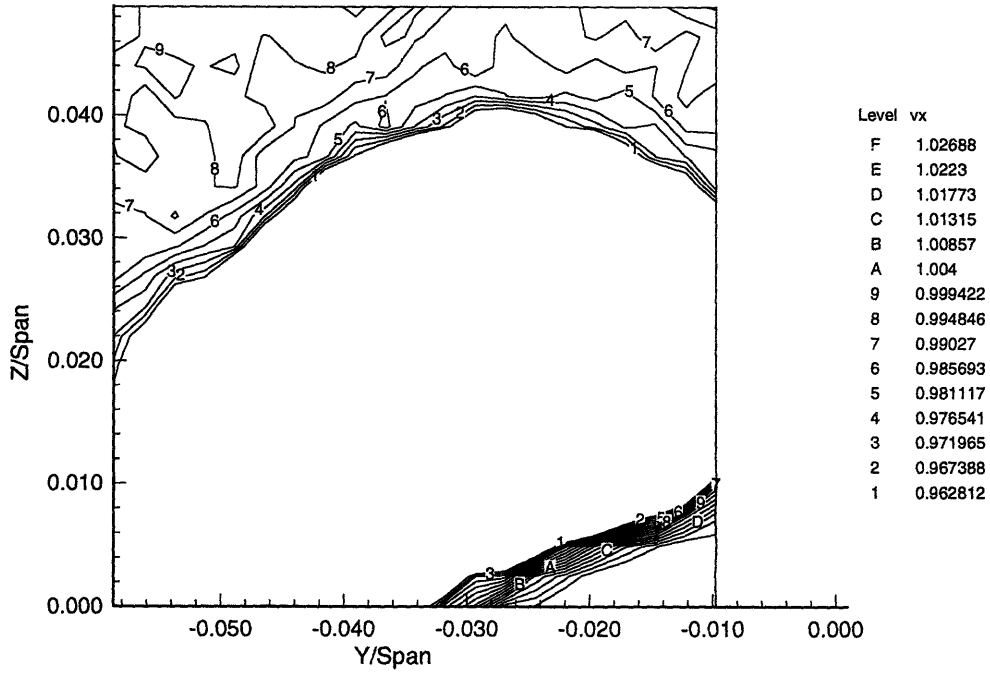


Figure 4-30: Streamwise velocity at $X/Span = -0.044$. Angle of attack is $+5.36$ degrees (side orientation/fine grid).

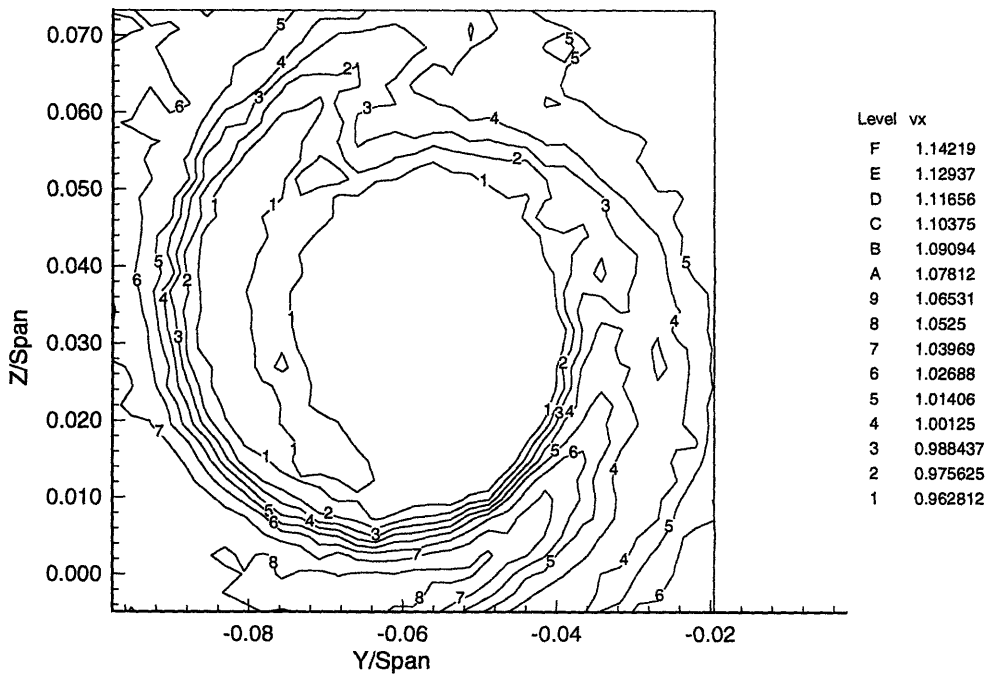


Figure 4-31: Streamwise velocity at $X/Span = -0.34$. Angle of attack is $+5.36$ degrees (side orientation/fine grid).

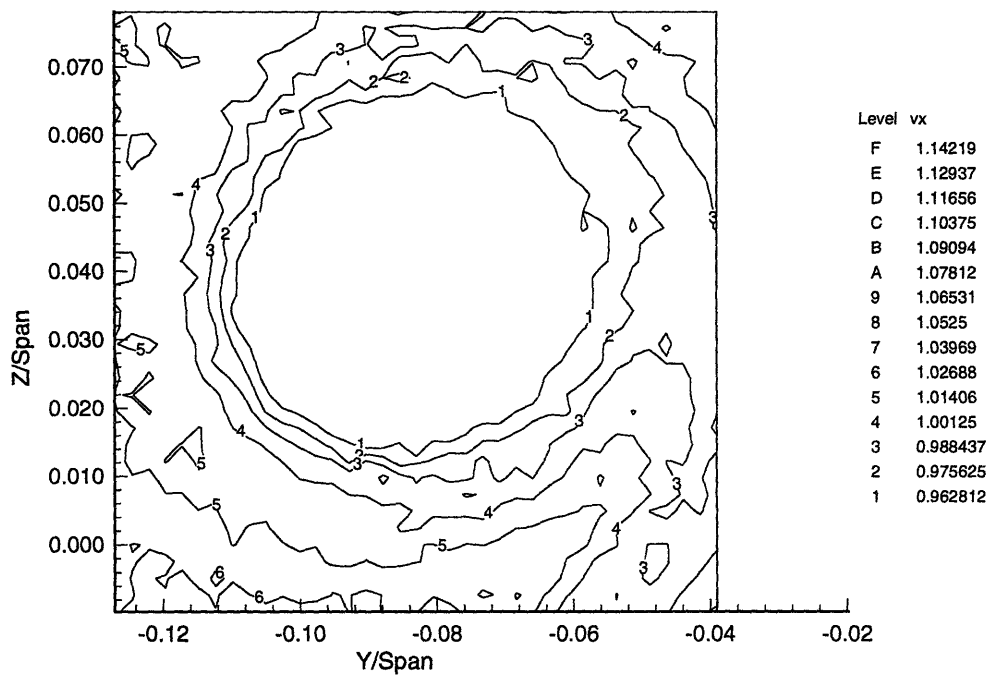


Figure 4-32: Streamwise velocity at $X/Span = -0.66$. Angle of attack is $+5.36$ degrees (side orientation/fine grid).

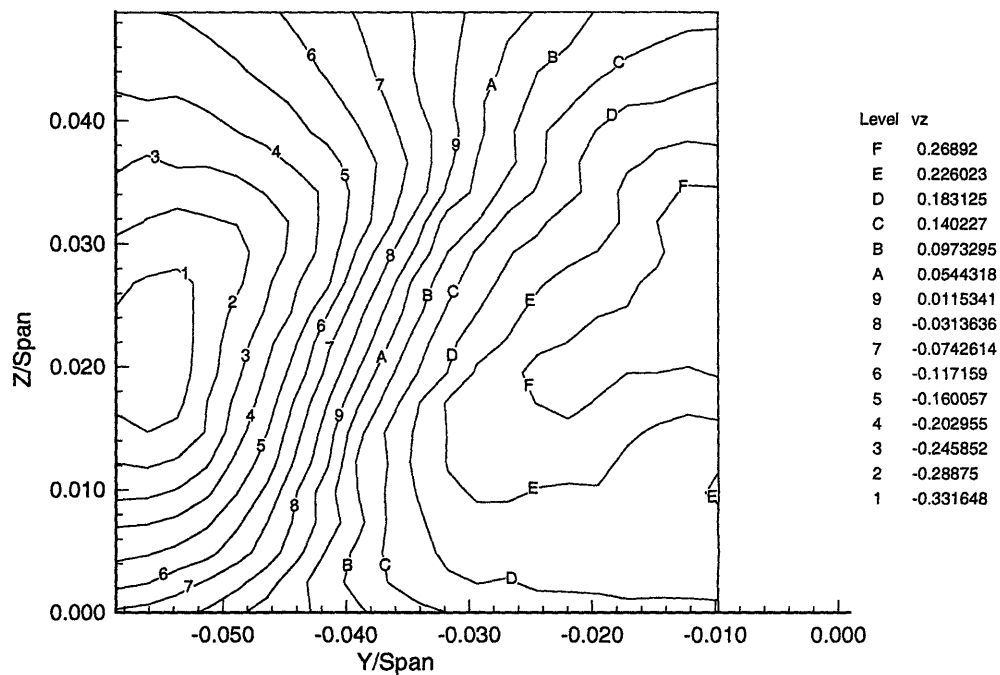


Figure 4-33: Vertical velocity at $X/Span = -0.044$. Angle of attack is $+5.36$ degrees (side orientation/fine grid).

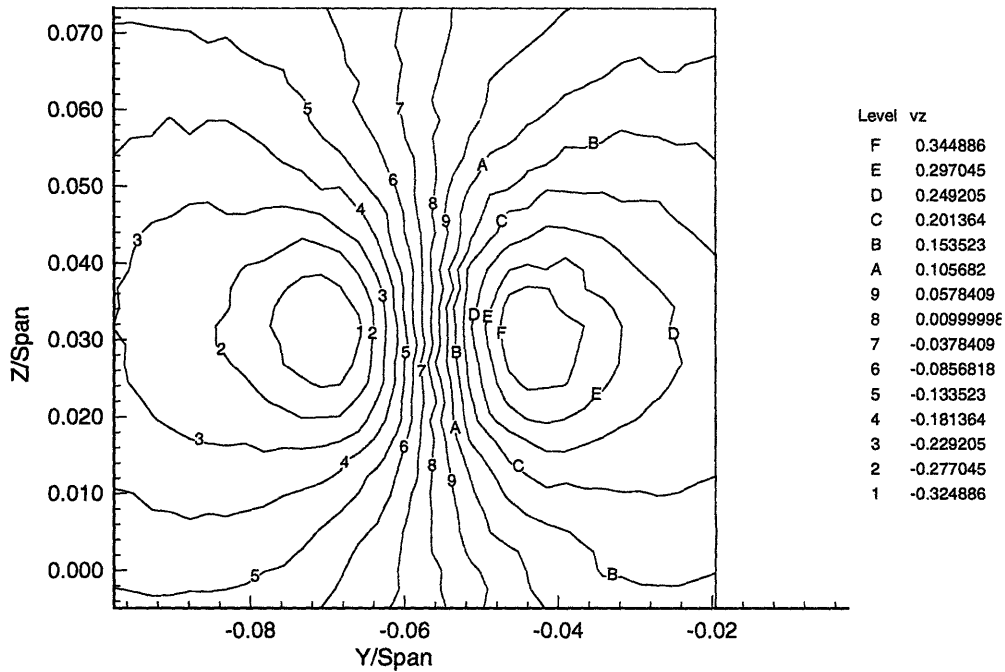


Figure 4-34: Vertical velocity at $X/Span = -0.34$. Angle of attack is $+5.36$ degrees (side orientation/fine grid).

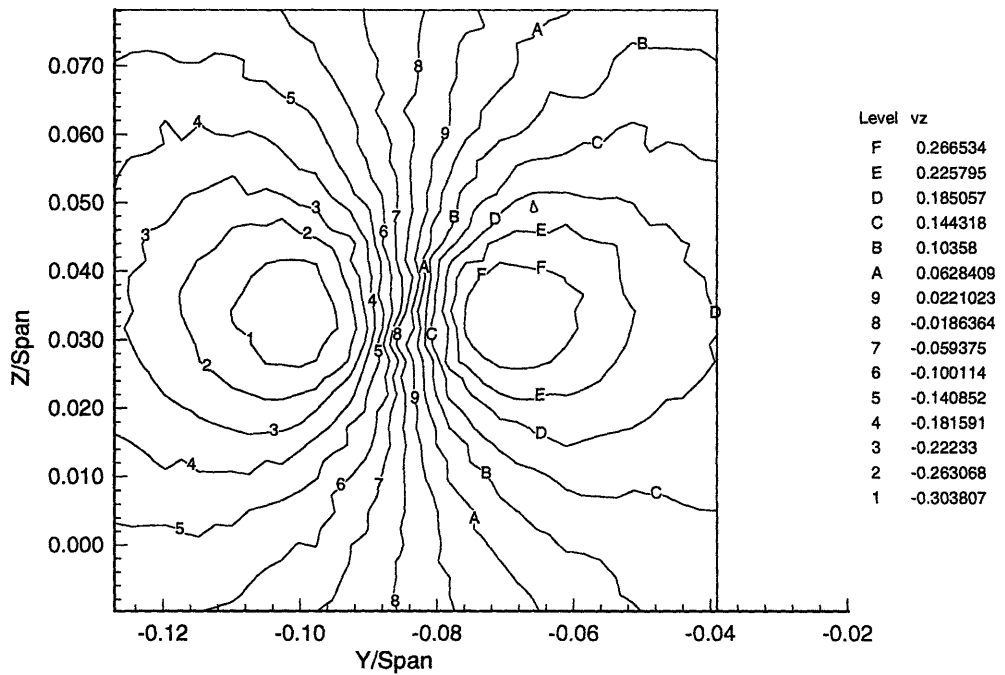


Figure 4-35: Vertical velocity at $X/Span = -0.66$. Angle of attack is $+5.36$ degrees (side orientation/fine grid).

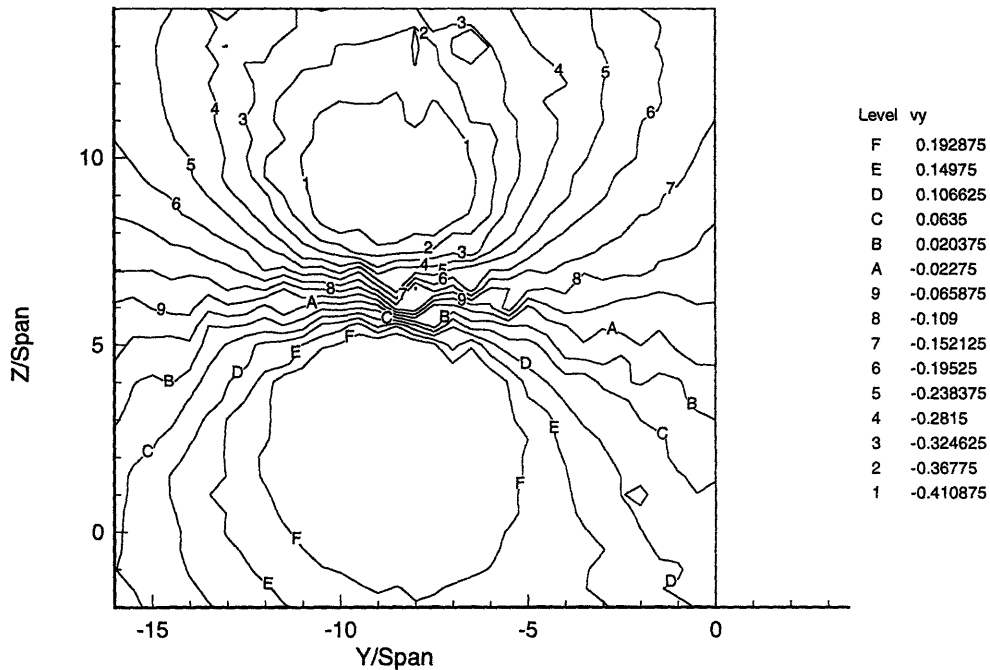


Figure 4-36: Spanwise velocity at $X/\text{Span} = -0.34$. Angle of attack is $+5.36$ degrees (top orientation/fine grid).

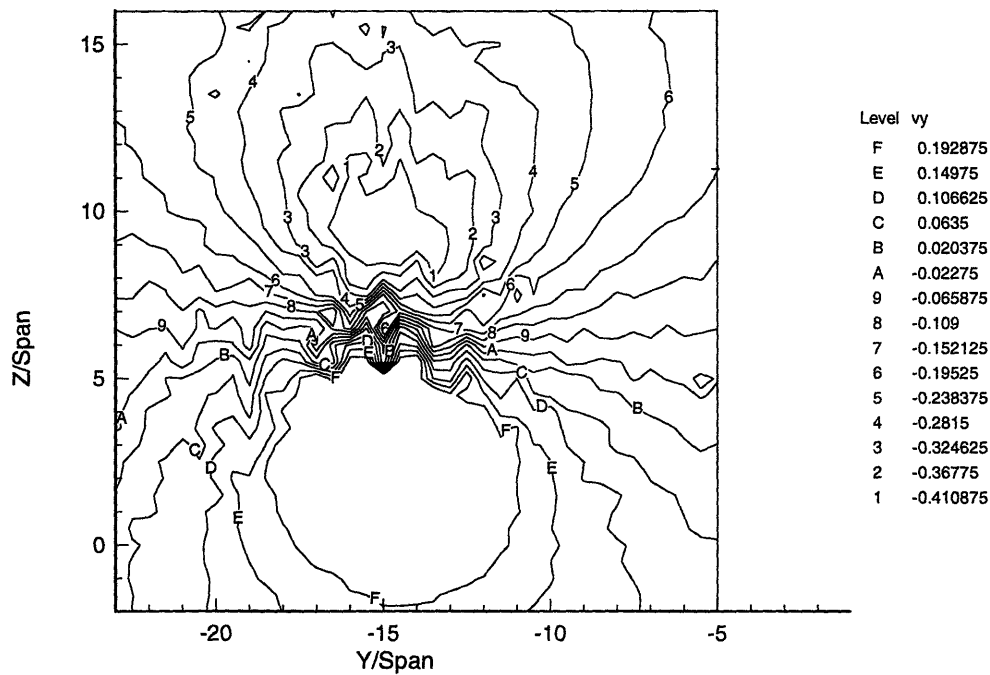


Figure 4-37: Spanwise velocity at $X/\text{Span} = -0.66$. Angle of attack is $+5.36$ degrees (top orientation/fine grid).

Chapter 5

Calculations

The results of the numerical model developed earlier are presented in this chapter. The first section will focus on convergence studies and the second portion will compare the numerical results to the experimental data.

5.1 Convergence Studies

There are essentially three criteria used to examine the convergence of the code. The first involves the number of iterations used for the wake to become aligned with the local velocity vector. Essentially, the program will continue iterating until each individual wake panel pitch angle is within 0.1 percent of the pitch angle of the local velocities. Once this is achieved, both the circulation distribution on the hydrofoil and the position of the wake are in agreement. Presumably, this is a unique state for a given angle of attack. All of the variations presented in this chapter met this convergence criterion. The other two tests include convergence by increasing the number of panels and convergence by lengthening the downstream portion of the tunnel.

The number of panels located spanwise on the hydrofoil was increased from four to 16, with the same number of panels chordwise. The maximum number of panels was chosen at 16 because of time limitations only. Figure 5-1 shows the spanwise circulation distribution as the number of panels is increased. There is a significant

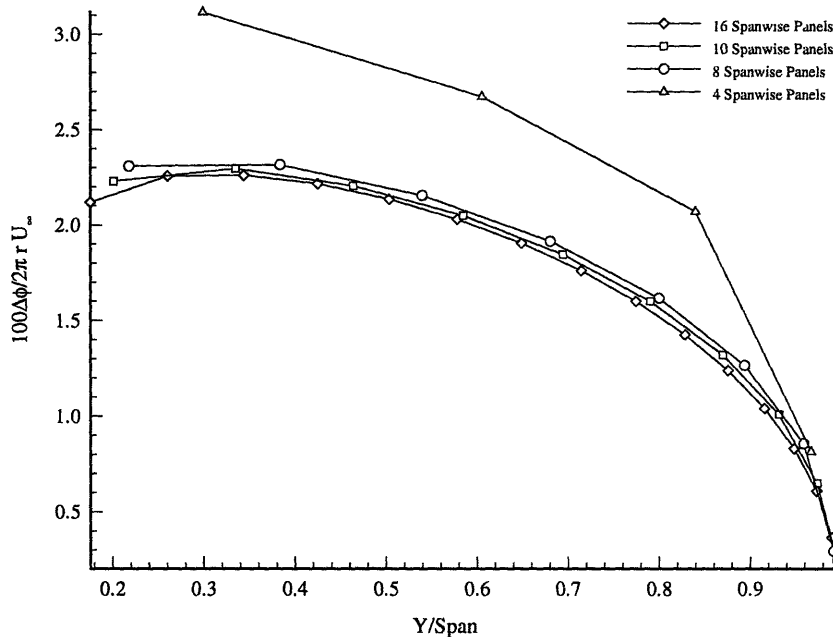


Figure 5-1: Comparison of spanwise circulation distribution by increasing the number of spanwise panels

improvement in the profile going from four to eight panels. The decrease in circulation in the proximity of the root is due to the foil's interaction with the half body. Overall, it appears that the circulation values readily converge.

Figures 5-2 through 5-4 show a spanwise cross section of the wake as it varies downstream. When $X/Span$ is 1.01 there is quite a discrepancy in the treatment of the tip vortex. With increased panelling and cosine spacing the number of panels located near the foil tip increases. The smaller tip panels are more susceptible to the complex velocity field near the tip. The tip behavior exhibited with the higher number of panels is due to the effects of crossflow around the tip and due to a tendency for these panels to simulate the vortex roll-up.

As the wake progresses downstream, the errant tip behavior of Figure 5-2 begins to straighten out. A crease appears to develop, though, between the two adjacent outboard panels. The strength of the interior wake discrete vortices is equal to the difference in circulation between two adjoining panels. The tip vortex strength is equated to the circulation associated with the very last panel only. As the panels

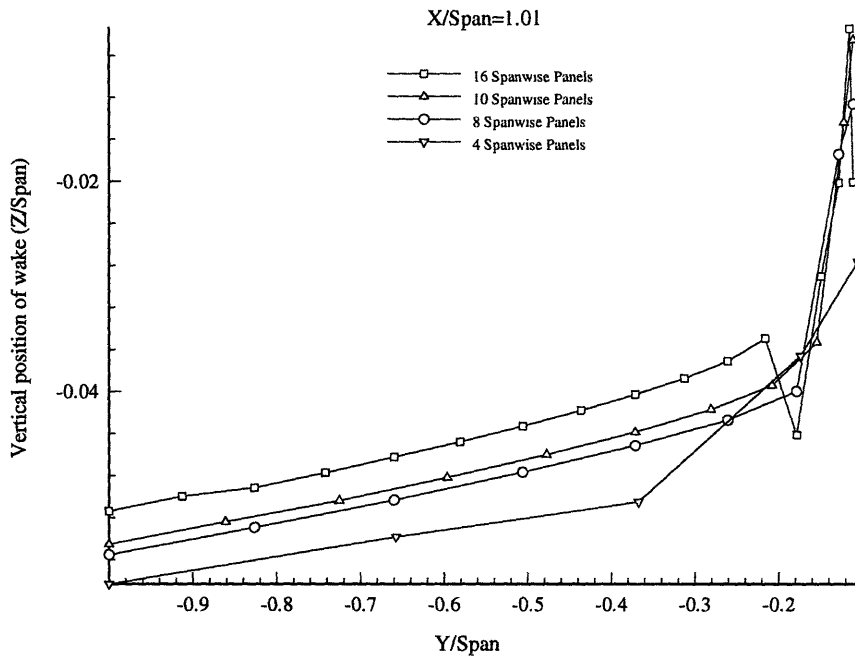


Figure 5-2: Comparison of vertical position of wake sheet by increasing the number of spanwise panels

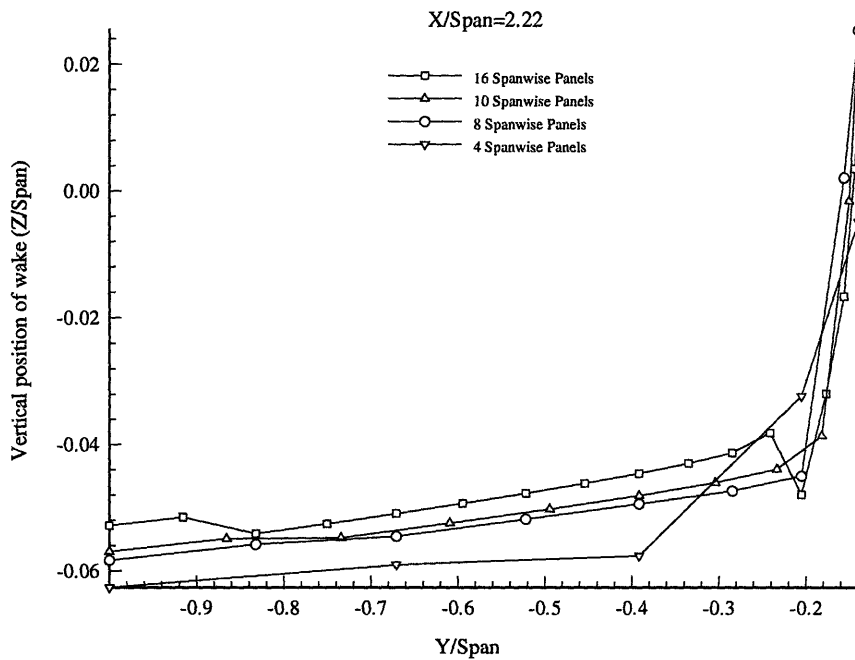


Figure 5-3: Comparison of vertical position of wake sheet by increasing the number of spanwise panels

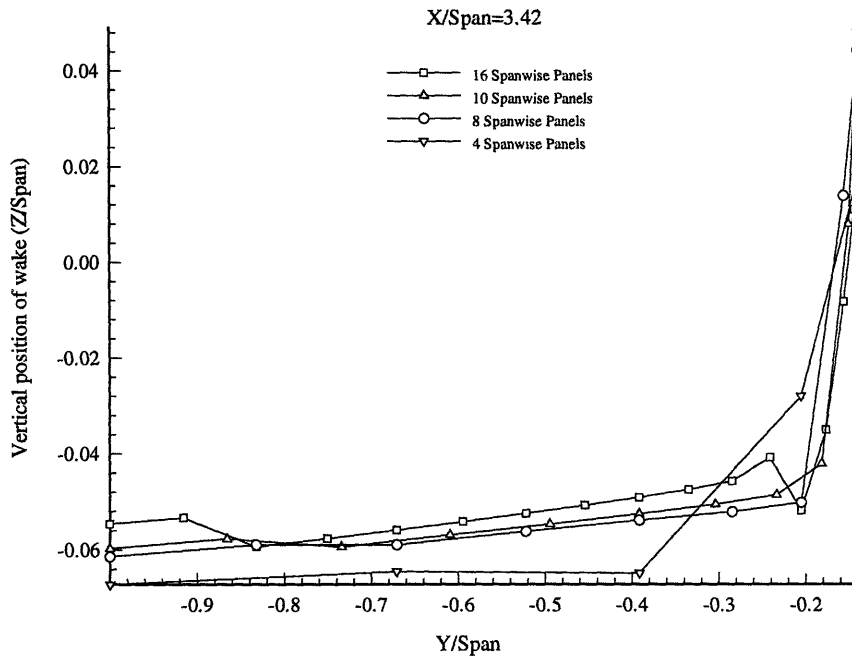


Figure 5-4: Comparison of vertical position of wake sheet by increasing the number of spanwise panels

become smaller near the tip, a situation occurs where the strength of the tip vortex is more than the influence of the nearest vortices forcing the panel boundary downward and creating the crease. Note also that the decrease in circulation distribution near the root of the foil is reflected in the downstream wake geometry for the higher panel case.

Recall that the panels are not free to move in the spanwise direction. The tip vortex roll-up therefore most evident by examining the slope of the outboard edge of the wake. At $X/Span$ of 3.42, the outer edge is almost vertical as the wake attempts to roll over on itself. As the number of panels increases the vertical position of the outboard edge of the wake will rise.

Chapter two discussed concern that modelling the tunnel with a finite length might lead to incorrect results. The effects of tunnel length are examined in Figures 5-6 through 5-9. For consistency, the eight spanwise panel case was selected and the length of the tunnel downstream of the foil was increased from the baseline of three spanlengths to a maximum of 12 spanlengths. As a reminder, in addition to the

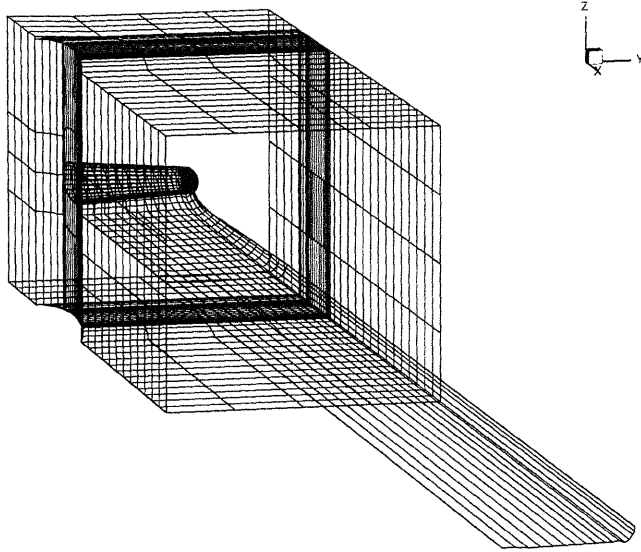


Figure 5-5: Complete panelling scheme for 16 spanwise panels. (Downstream looking forward.)

length of the downstream portion of the tunnel, a final row of wake panels is attached downstream, extending beyond the end of the tunnel (See Figure 5-5). These panels are 10 spans long and are used to simulate the effects of the starting vortex. Figure 5-6 shows the convergence of the circulation distribution. The seeming discrepancy which occurs between the eight and 12 span lengths is due to an unexplained premature pruning of the results for the 12 panel case by the computer. Figures 5-7 through 5-9 show the convergence of the spanwise wake shape with increasing tunnel length. With the exception of X/Span of 3.42, there is virtually no difference in the local flow velocities of the wake as the tunnel length is increased. Examining the behavior of the root vortex (Figure 5-10) and the tip vortex (Figure 5-11), it seems that the increased tunnel length has little bearing on the geometry of the wake.

5.2 Comparison to experimental data

The output of the code is also validated by comparing it not only to the experimental data, but also to what might be expected analytically from potential flow theory.

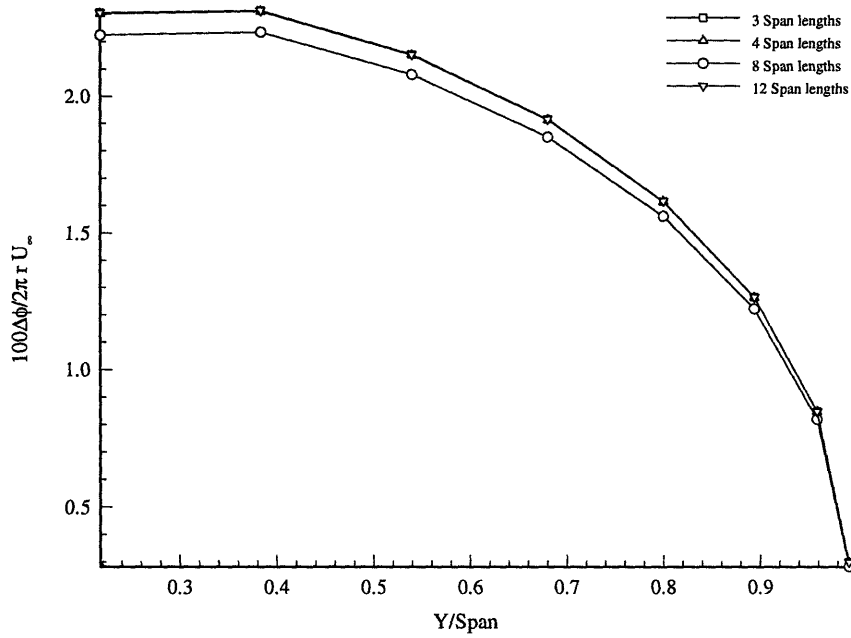


Figure 5-6: Comparison of spanwise circulation distribution by increasing downstream tunnel length

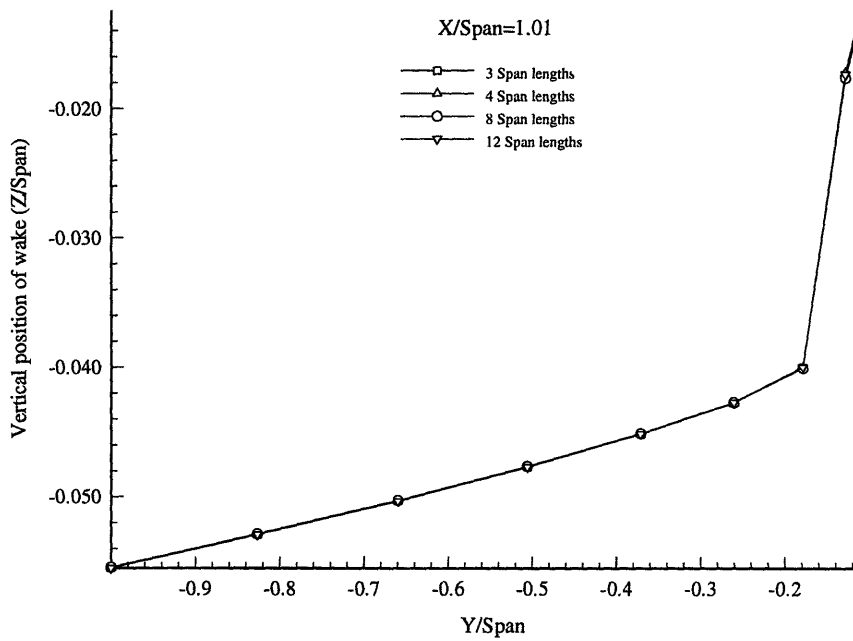


Figure 5-7: Comparison of spanwise wake shape by increasing downstream tunnel length

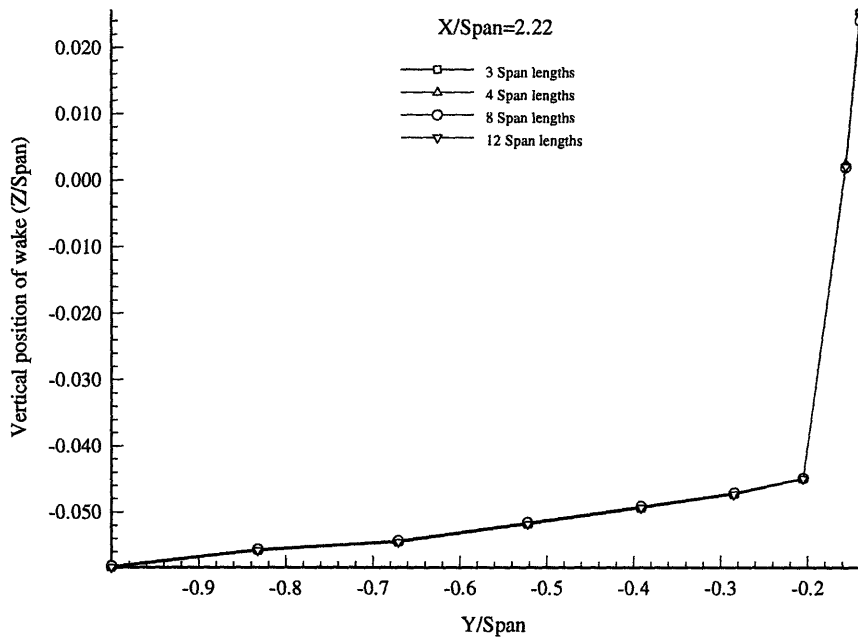


Figure 5-8: Comparison of spanwise wake shape by increasing downstream tunnel length

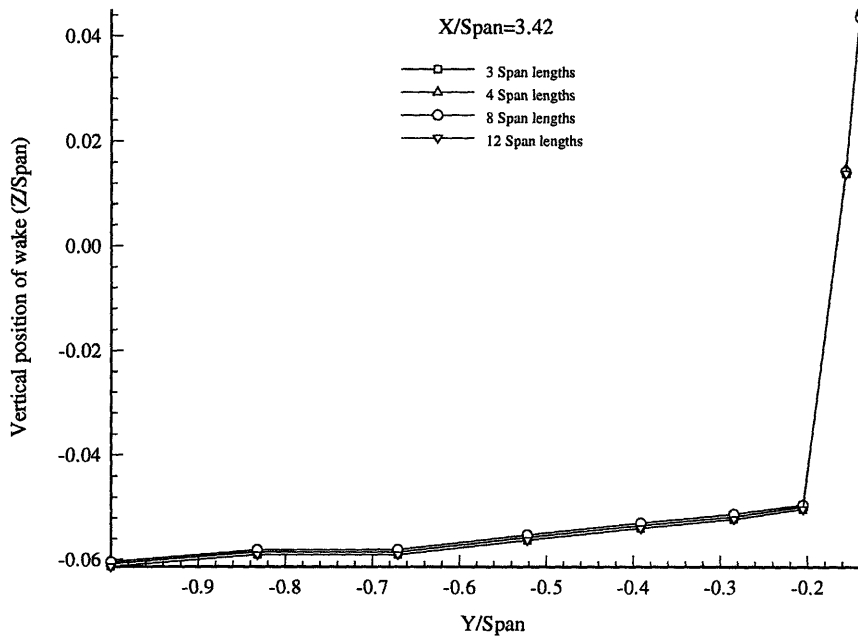


Figure 5-9: Comparison of spanwise wake shape by increasing downstream tunnel length

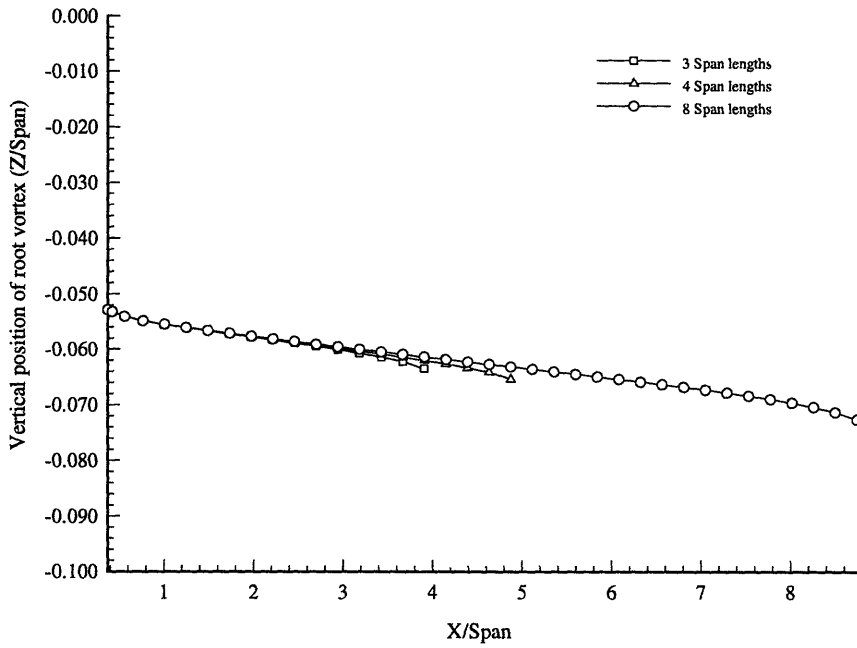


Figure 5-10: Comparison of tip vortex position by increasing downstream tunnel length

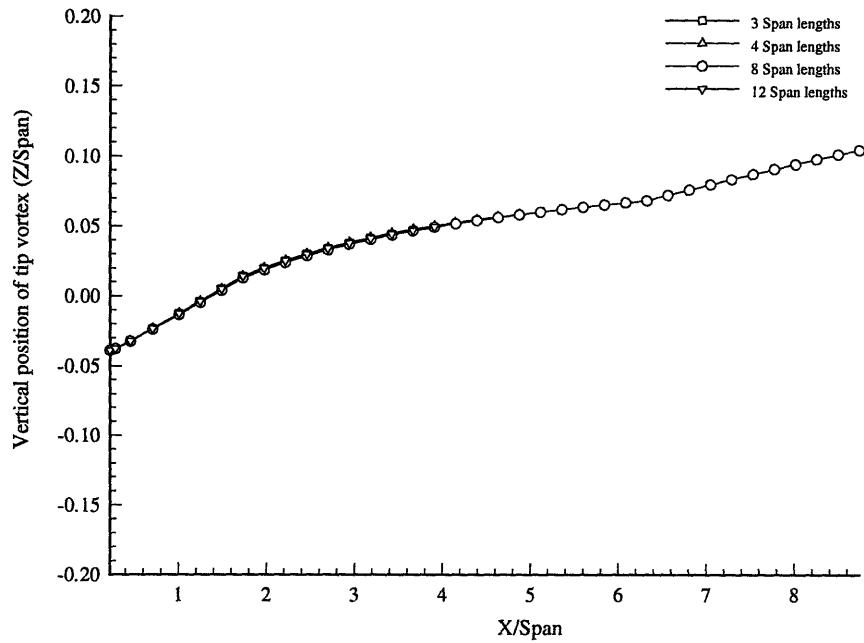


Figure 5-11: Comparison of root vortex position by increasing downstream tunnel length

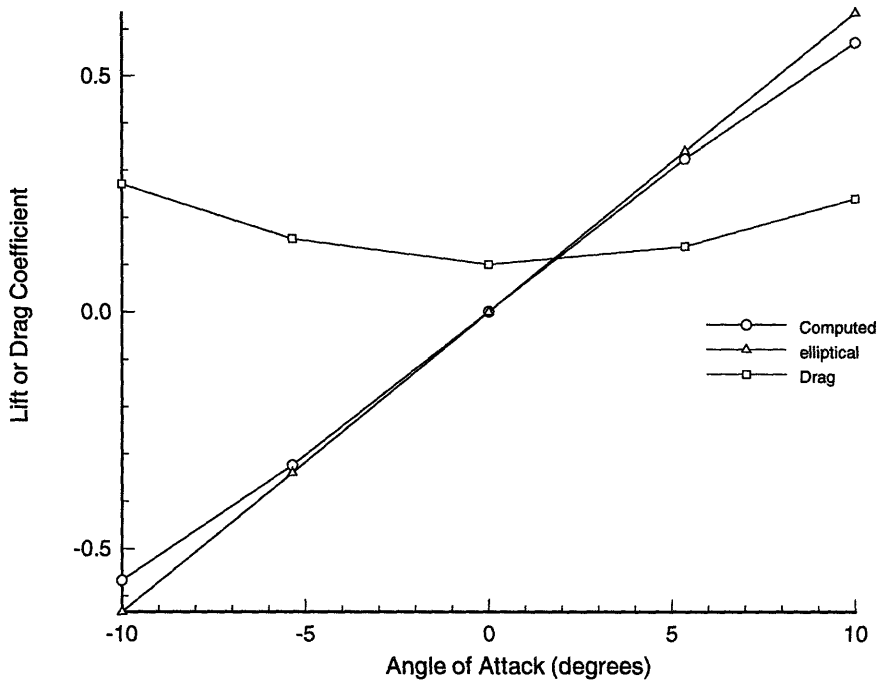


Figure 5-12: Calculated lift and drag coefficients

This latter, often ignored comparison is essential to the development of an accurate code. To be useful, a code must be able to handle the rigors of the analytical limits of the problem. A program which can only predict the results of the given experimental conditions is self-defeating. There would be no reason to rely on a code if experimental results are available.

The non-dimensional lift coefficient for an elliptical wing is given by

$$\bar{C}_L = \frac{2\pi\alpha}{1 + 2/\mathcal{A}} \quad (5.1)$$

where \bar{C}_L is the total lift coefficient, α is the angle of attack, and \mathcal{A} is the aspect ratio of the wing,

$$\mathcal{A} = \frac{4(\text{span})}{\pi c_o}. \quad (5.2)$$

The lift coefficient for the elliptical wing is shown against the lift coefficient calculated by the code in Figure 5-12. The difference may be attributed partly to the presence of the halfbody and partly due to the fact that the semi-span is not elliptical. The computed drag coefficient is also presented for reference.

For an elliptical wing in an infinite domain, the sectional lift coefficient may be regarded as equal to the total lift coefficient \bar{C}_L [8] and the spanwise circulation distribution is

$$\Gamma(y) = \frac{1}{2} \bar{C}_L U_\infty c(y) \quad (5.3)$$

where $c(y)$ is the chord length. This equation is only valid for the elliptical wing, but it gives a reasonable estimate of the maximum value of circulation for the semi-span, which when non-dimensionalized by the freestream velocity and the span length, is 2.53.

Turning next to the experimental data, the circulation distribution was measured by Coney for the same model [4], however he calculated values for $\alpha = 7.5$ degrees. His maximum measured value of circulation at the root of the semi-span equates to a value near 2.9. Although the spanwise circulation was not measured in the present testing, an approximate estimate of the the total circulation can be obtained by assuming that all of the wake's free vorticity is concentrated in the tip vortex at the $\mathbf{X}/\text{Span} = 1.67$ point. The velocity data from this grid may be numerically integrated to give a total circulation value of 3.625 when non-dimensionalised as above.

With the circulation data verified, the velocity output is examined. An important difference between the computer model and the actual experiment is that the free vorticity in the real wake will quickly roll up into the concentrated tip vortex. In the model, the vorticity remains constant streamwise and only varies in the spanwise direction, reflecting the circulation on the foil. The velocities due to a line vortex comes from Biot-Savart

$$\mathbf{V} = \frac{\Gamma}{4\pi} \oint \frac{\mathbf{s} \times \mathbf{r}}{r^3} dl \quad (5.4)$$

If the vortex filament is sufficiently long enough the velocities induced by the vortex are similar to that of a semi-infinite two-dimensional vortex [8]

$$w(y) = \frac{\Gamma}{4\pi y}. \quad (5.5)$$

From the equation above, estimates of the velocities in the proximity of the tip vortex

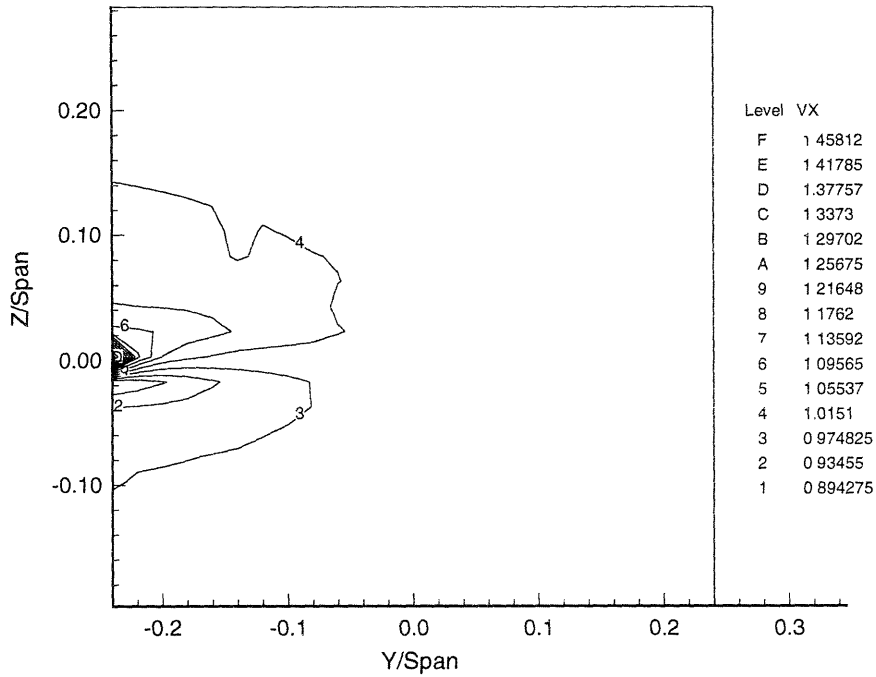


Figure 5-13: Computed streamwise velocity at $X/Span=-0.044$. Angle of attack is $+5.36$ degrees (coarse grid).

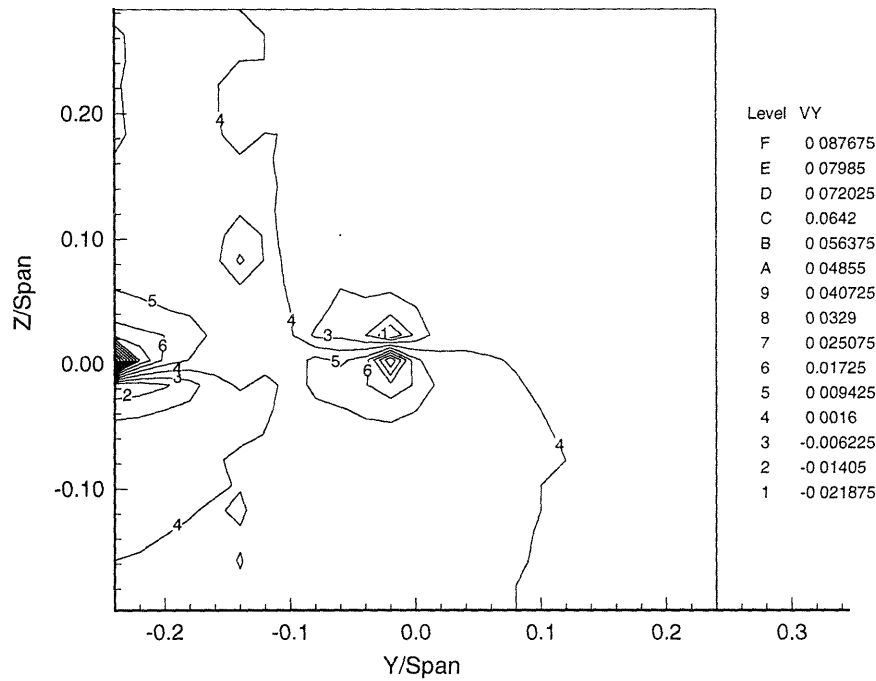


Figure 5-14: Computed spanwise velocity at $X/Span=-0.044$. Angle of attack is $+5.36$ degrees (coarse grid).

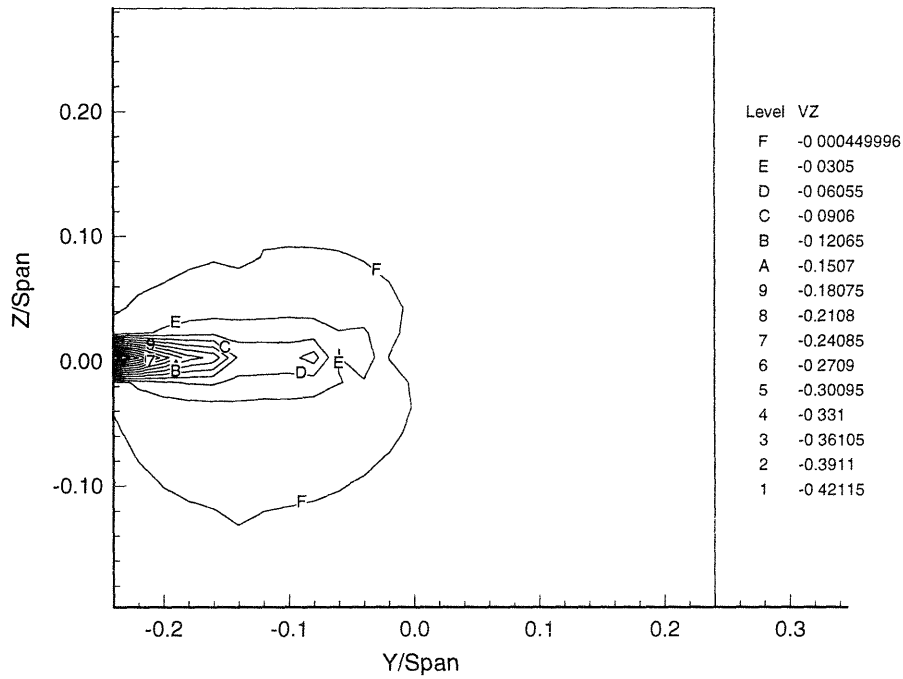


Figure 5-15: Computed vertical velocity at $X/Span=-0.044$. Angle of attack is $+5.36$ degrees (coarse grid).

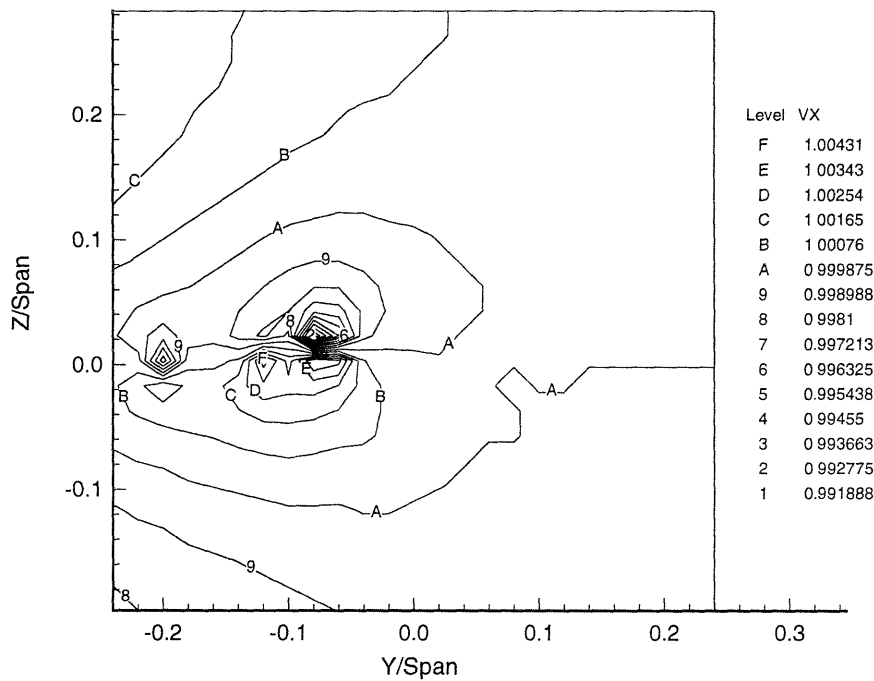


Figure 5-16: Computed streamwise velocity at $X/Span=-0.34$. Angle of attack is $+5.36$ degrees (coarse grid).

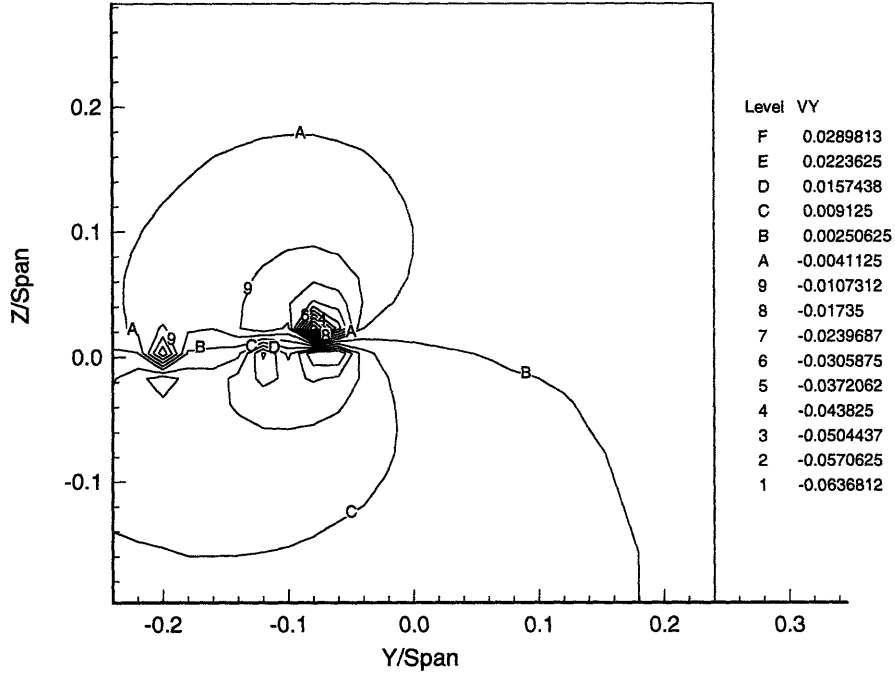


Figure 5-17: Computed spanwise velocity at $X/Span=-0.34$. Angle of attack is $+5.36$ degrees (coarse grid).

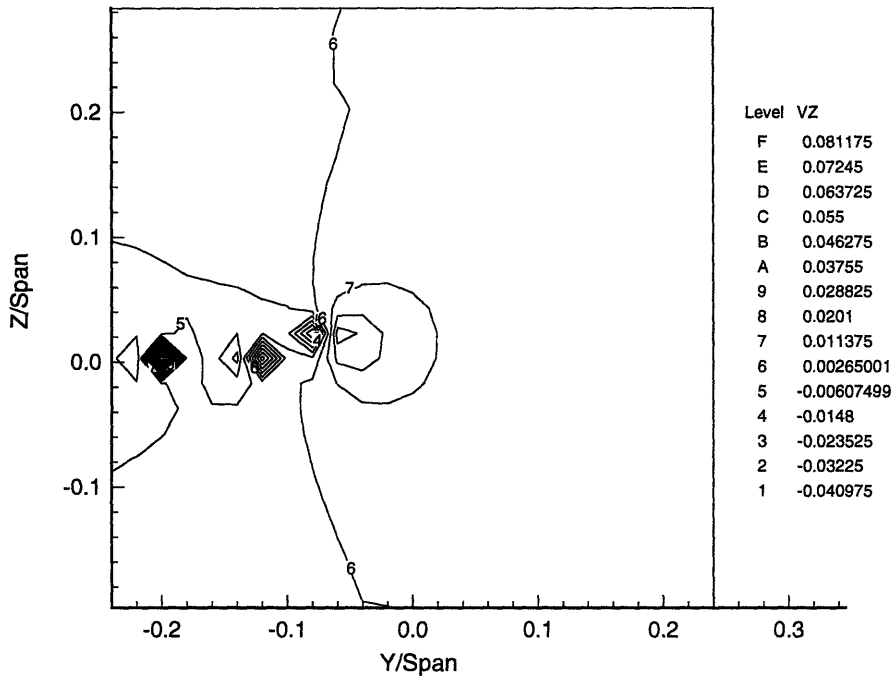


Figure 5-18: Computed vertical velocity at $X/Span=-0.34$. Angle of attack is $+5.36$ degrees (coarse grid).

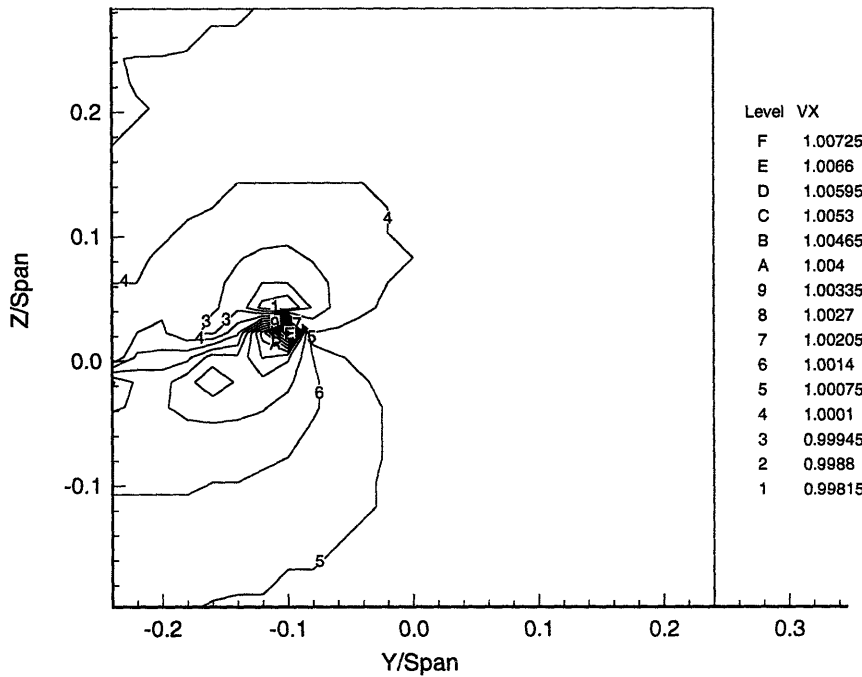


Figure 5-19: Computed streamwise velocity at $X/Span=-0.66$. Angle of attack is $+5.36$ degrees (coarse grid).

may be estimated, assuming that the strength of the vortex is equal to the Γ determined above. It is at this point where a discrepancy lies between the panel code and the experimental data, causing the induced velocities to be roughly 10 times smaller than the measured values. It is postulated that the velocities shown in Figures 5-13 through 5-27 are only due to the tip vortex of the wake, instead of the sum of the wake vortices. Since the strength of each vortex is fixed in the streamwise direction, the tip vortex never increases in strength, as the actual tip vortex does, to induce higher velocities.

As another comparison, the panel code calculated the velocities across the surface of the semi-span. Unlike the velocities calculated above, the surface velocities were calculated using a central difference formula to differentiate the potential of the hydrofoil panels. The potentials are only known at the panel centroids giving Figures 5-28, 5-29, and 5-30 an irregular outline. These surface velocities are compared to the two dimensional values presented by Abbot and Von Doenhoff [1] in Figure 5-31. The maximum velocity across the semi-span is higher due to the half body reducing

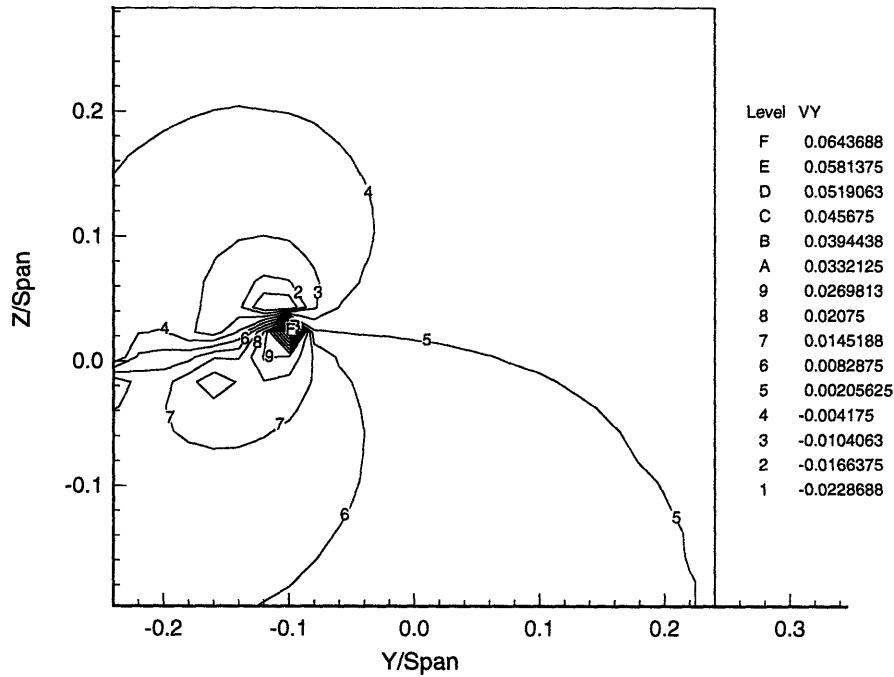


Figure 5-20: Computed spanwise velocity at $X/Span=-0.66$. Angle of attack is $+5.36$ degrees (coarse grid).

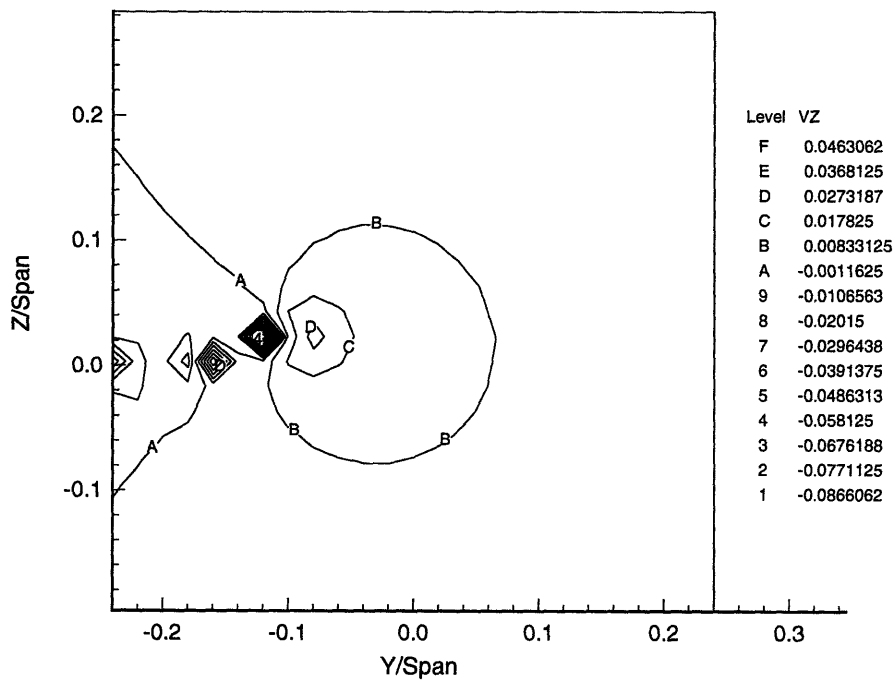


Figure 5-21: Computed vertical velocity at $X/Span=-0.66$. Angle of attack is $+5.36$ degrees (coarse grid).

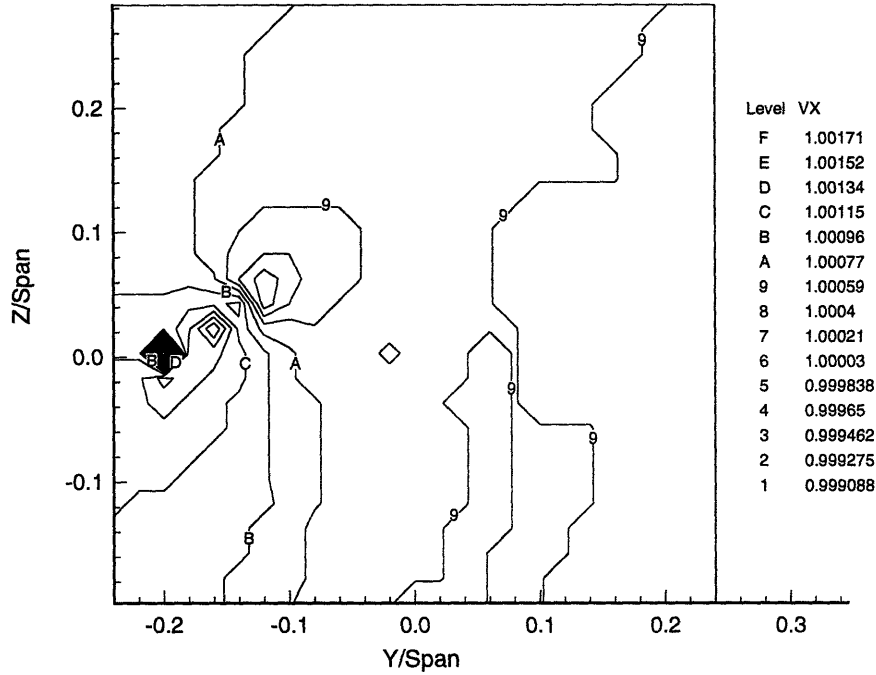


Figure 5-22: Computed streamwise velocity at $X/Span=-1.28$. Angle of attack is $+5.36$ degrees (coarse grid).

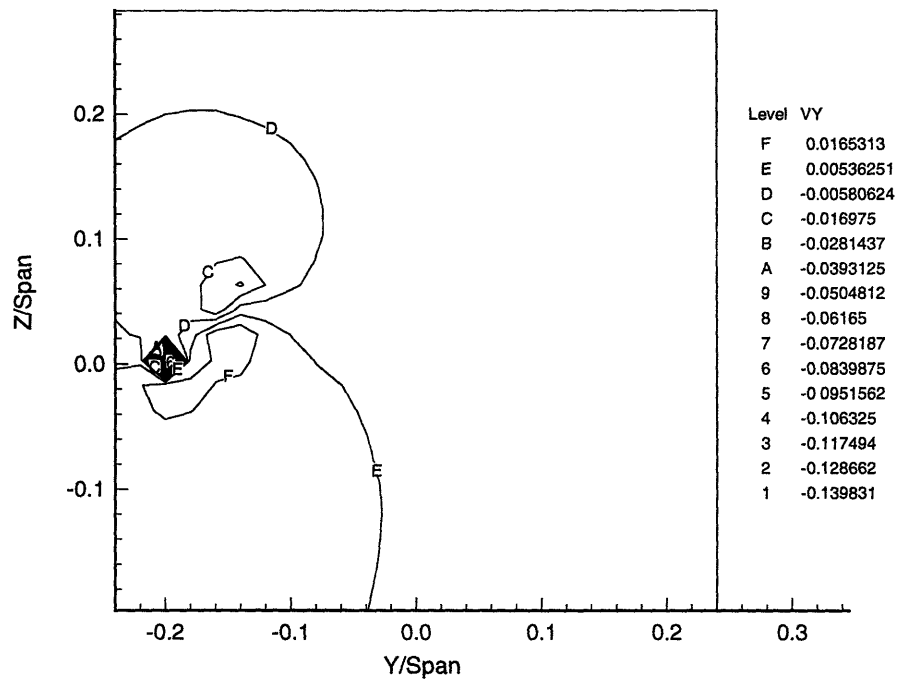


Figure 5-23: Computed spanwise velocity at $X/Span=-1.28$. Angle of attack is $+5.36$ degrees (coarse grid).

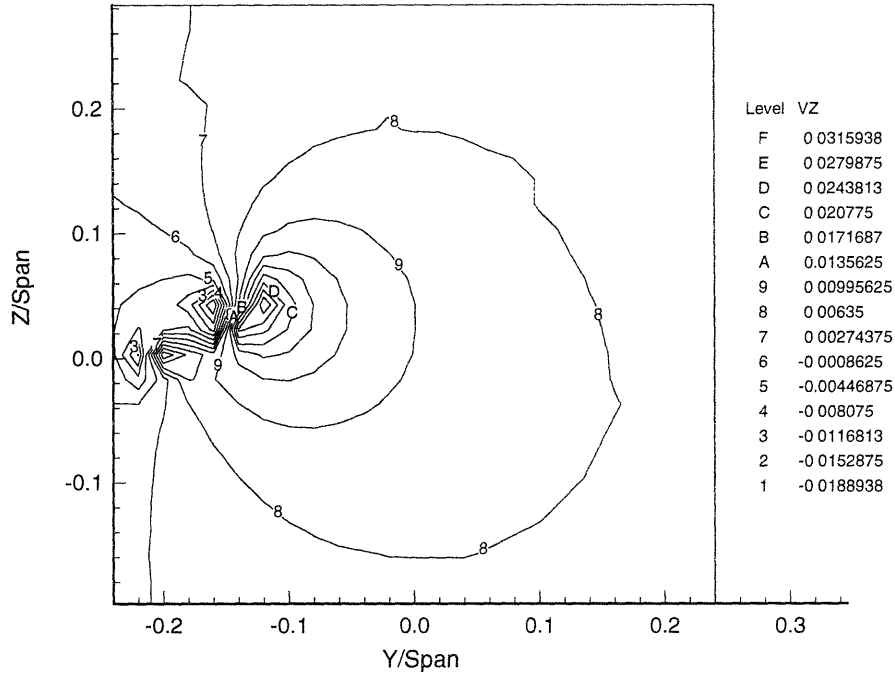


Figure 5-24: Computed vertical velocity at $X/Span=-1.28$. Angle of attack is $+5.36$ degrees (coarse grid).

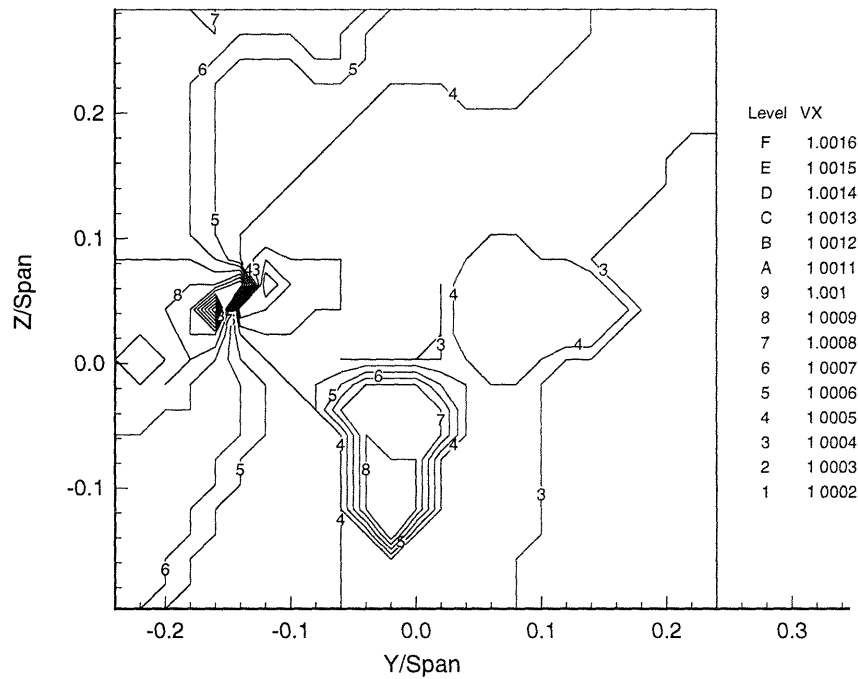


Figure 5-25: Computed streamwise velocity at $X/Span=-1.67$. Angle of attack is $+5.36$ degrees (coarse grid).

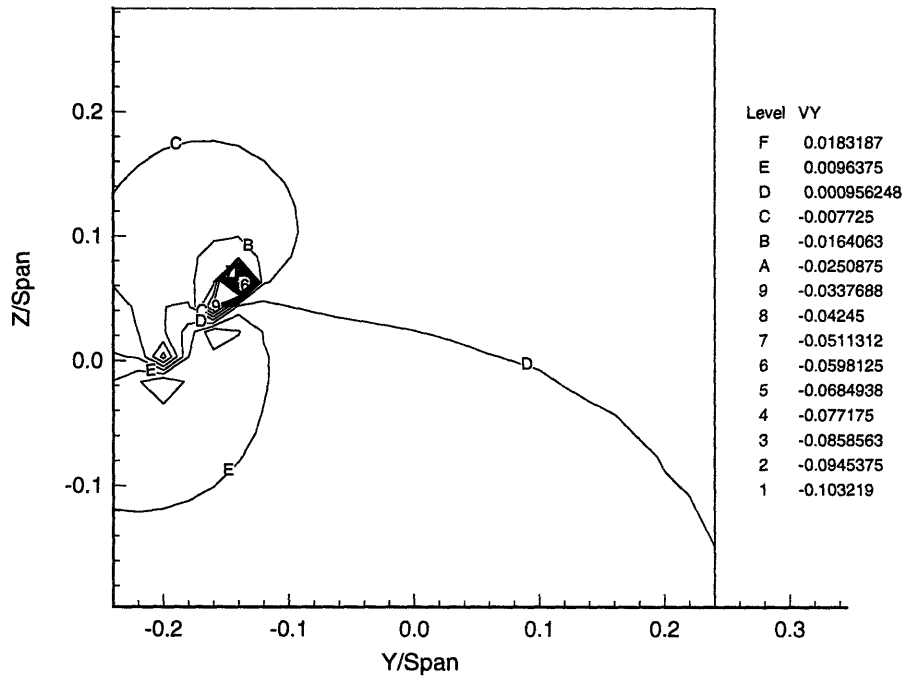


Figure 5-26: Computed spanwise velocity at $X/Span=-1.67$. Angle of attack is $+5.36$ degrees (coarse grid).

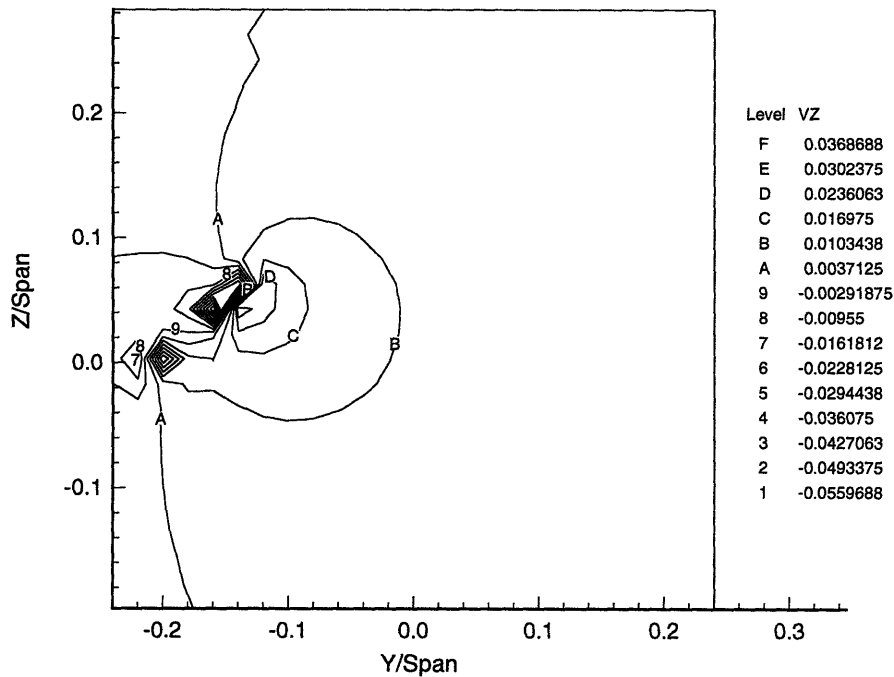


Figure 5-27: Computed vertical velocity at $X/Span=-1.67$. Angle of attack is $+5.36$ degrees (coarse grid).

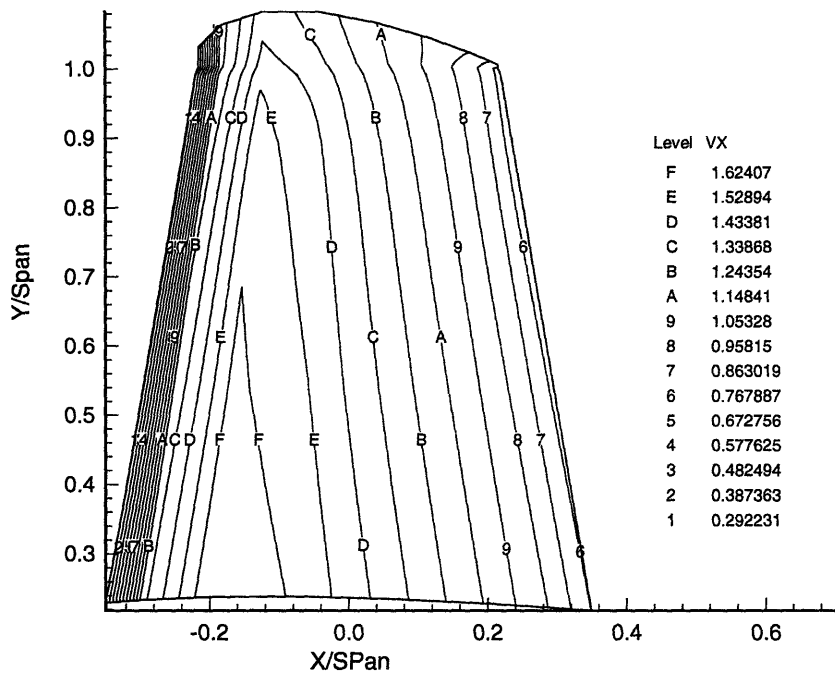


Figure 5-28: Comparison of streamwise velocities across the surface of the hydrofoil at 0 degree angle of attack

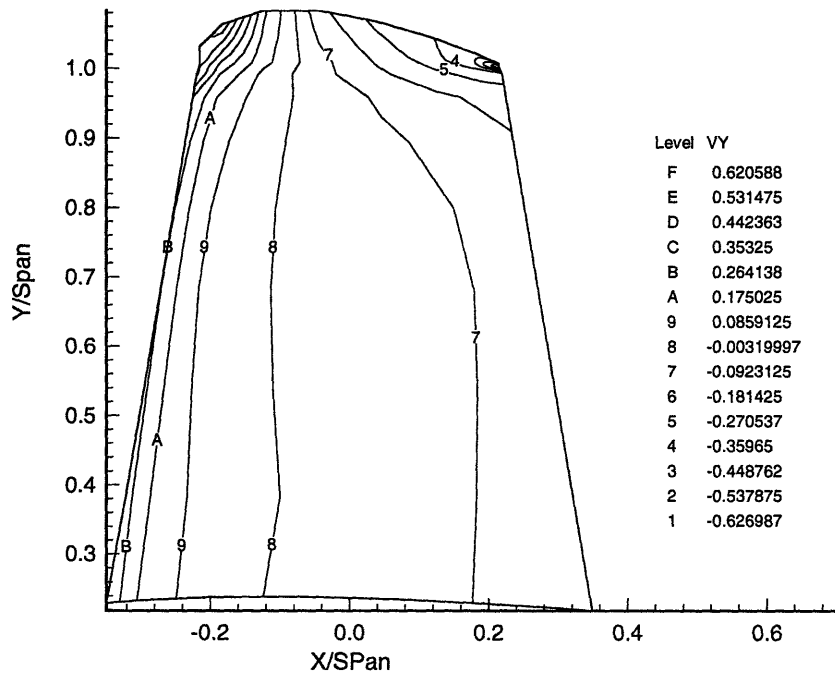


Figure 5-29: Comparison of spanwise velocities across the surface of the hydrofoil at 0 degree angle of attack

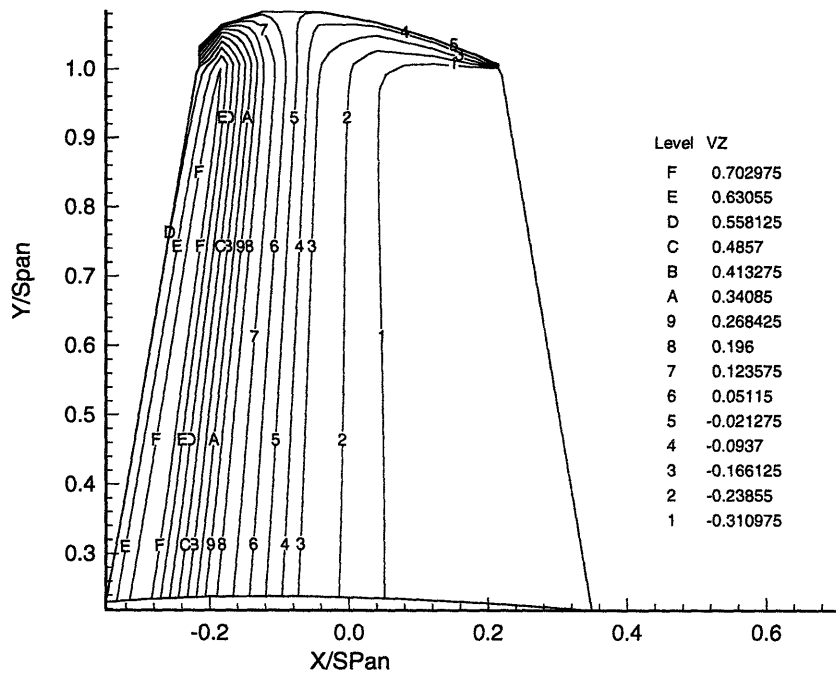


Figure 5-30: Comparison of vertical velocities across the surface of the hydrofoil at 0 degree angle of attack

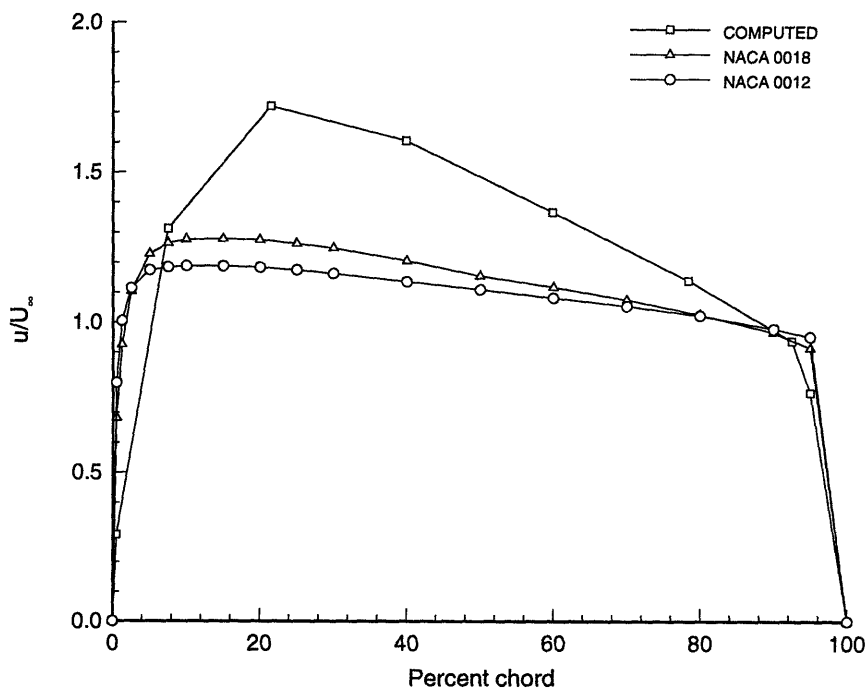


Figure 5-31: Comparison of streamwise velocities across the surface of the hydrofoil at 0 degree angle of attack

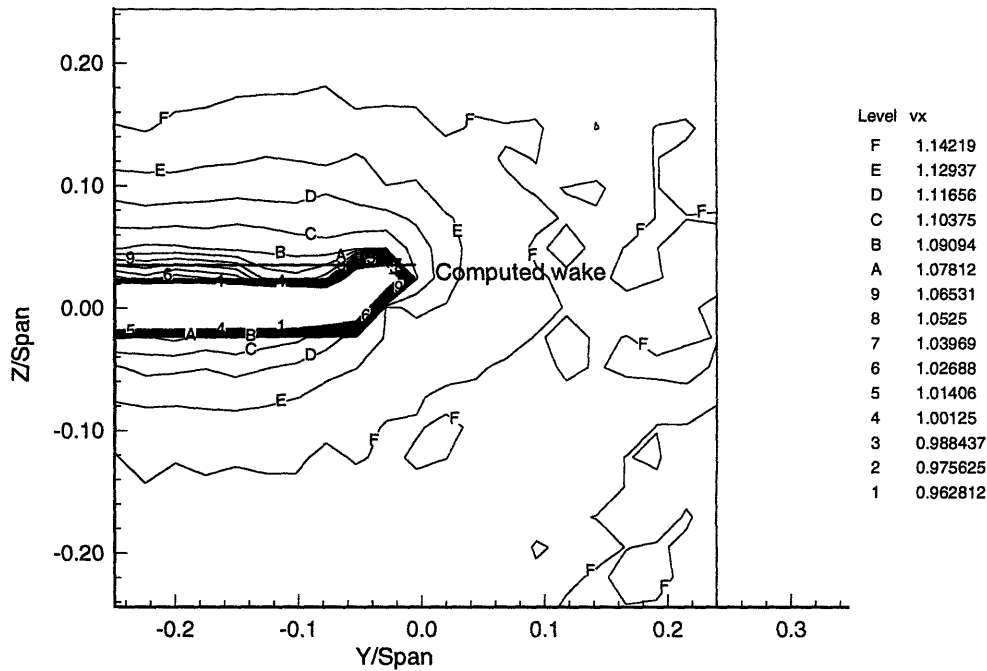


Figure 5-32: Experimental wake shape with panel code predicted wake shape superimposed. ($X/Span = -0.044$)

the tunnel's cross-sectional area at that point. The resulting velocity may be thought of as a product of the effects the two joining hydrofoils.

The shape of the wake predicted by the panel code is quite similar to that observed in the experiment. Although this experiment focused on the wake behavior nearest the tip vortex, Coney's work included measurements of the complete wake. He used a negative 7.5 degree angle of attack and did not present detailed plots of the coordinates of the measured wake, but the overall shape of his baseline case resembles the output of the panel code. The position of the computer-generated wake is superimposed on the graphs of experimental data in Figures 5-32 through 5-36. The location of the tip vortex, represented by the outboard edge of the wake, is reasonably close to the experimental data.

The panel code predicts the circulation distribution, wake shape and wake position reasonably well. Still, the error in calculating the induced velocities is not trivial. It would appear to be localized to the routine which computes the local velocity vector for a given field point, however, it could just as easily be a larger error which pervades

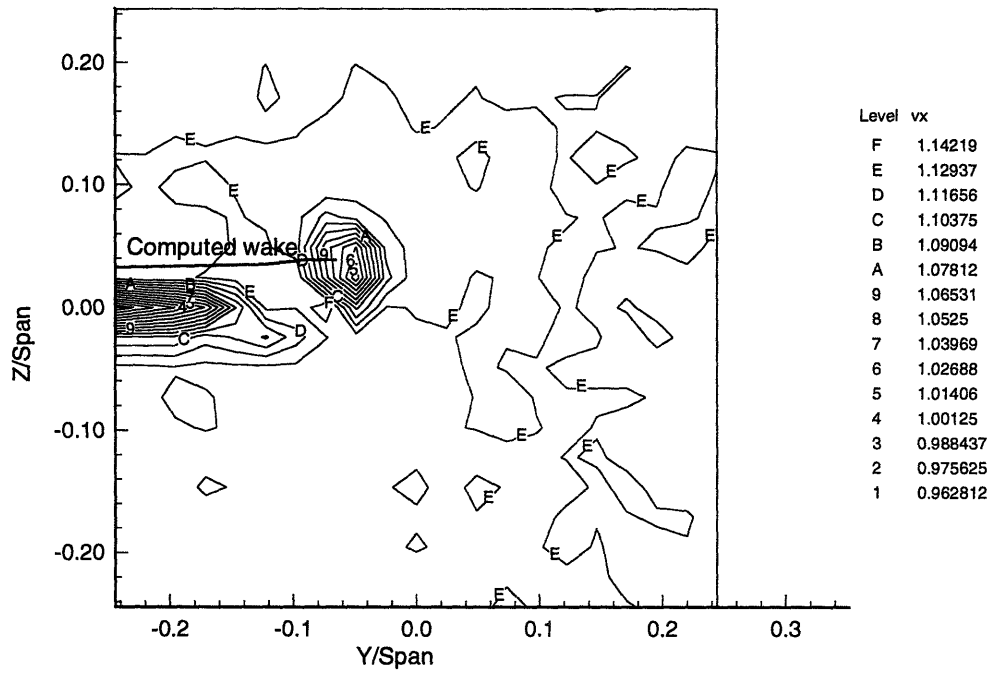


Figure 5-33: Experimental wake shape with panel code predicted wake shape superimposed. ($X/Span = -0.34$)

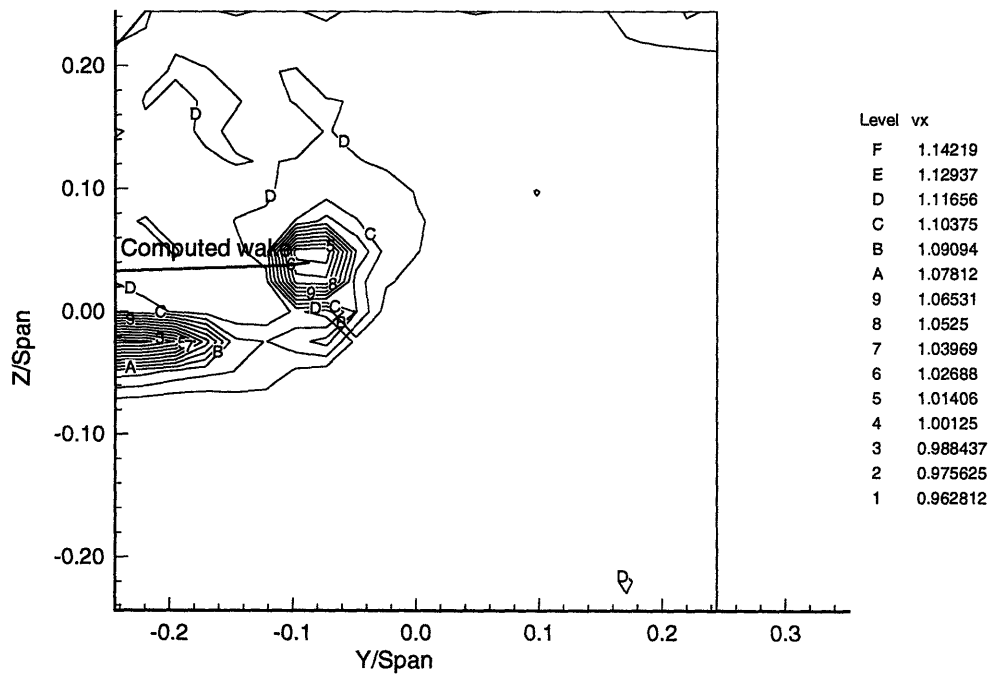


Figure 5-34: Experimental wake shape with panel code predicted wake shape superimposed. ($X/Span = -0.66$)

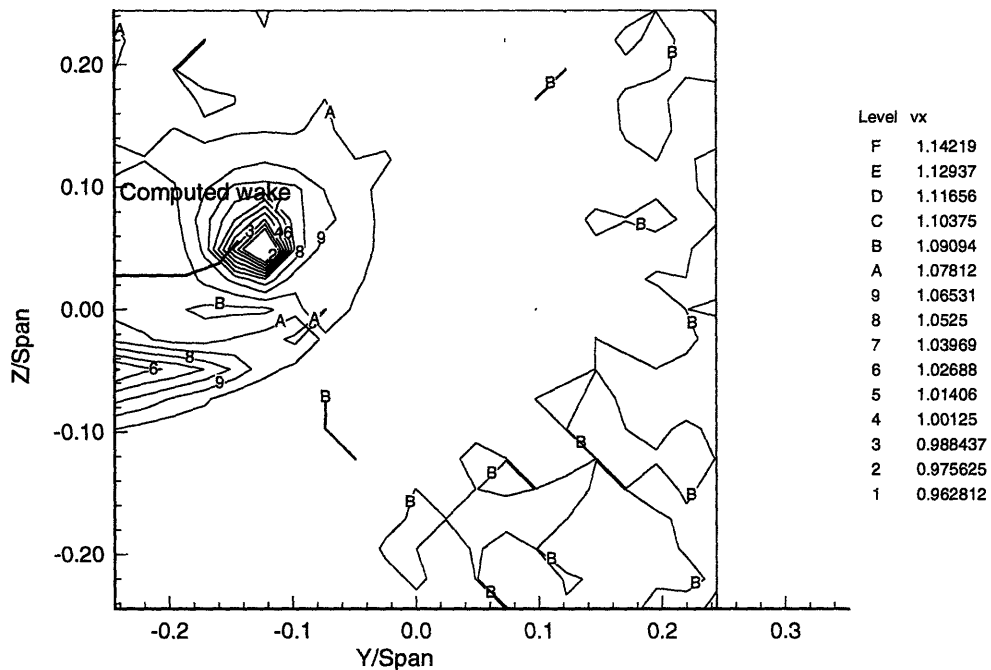


Figure 5-35: Experimental wake shape with panel code predicted wake shape superimposed. ($X/Span=-1.28$)

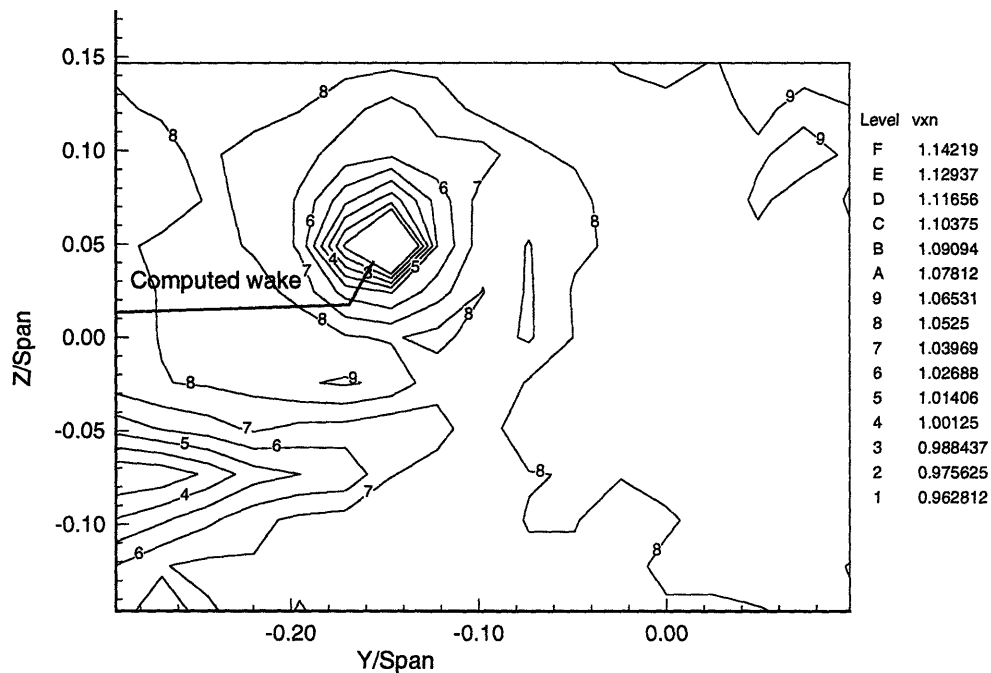


Figure 5-36: Experimental wake shape with panel code predicted wake shape superimposed. ($X/Span=-1.67$)

the entire wake alignment procedure. The panel code presented here is a rudimentary, first approximation. Further revision will be required to ensure that the program can be exercised to its limits.

Chapter 6

Conclusions

A perturbation potential panel code has been modified for use on a semi-span hydrofoil attached to a half body within a water tunnel. In doing so, the panel code has been revised to address problems not normally encountered in its common usage as a propeller code. Specifically, panelling the model walls in an attempt to gain additional insight into their effects on the semi-span geometry is a complicated problem even in potential flow. The addition of viscous effects and a developing boundary layer on the walls introduces another dimension of complexity which has received much attention from aerodynamic researchers. The code has also implemented a revised method of modelling and aligning the wake, combining both a vortex lattice routine for wake-induced velocities and relying on differentiation of the panel potentials to calculate the effects of the semi-span, half body and tunnel. After several iterations of the process, an independent prediction of the steady state wake geometry is obtained.

Several features could be added to this code to enhance its accuracy. Coupling it to a viscous model is an obvious, but hardly a simple choice. In addition to the boundary layer development along the tunnel walls and hydrofoils, the effects within the wake sheet would also make a significant difference in the results. The tip vortex separation would also be effected. Another clear choice would be to better simulate the tip vortex roll up. This becomes especially difficult to panel as the they must change in size and direction in three dimensions without penetrating one another. A code which addresses this difficulty is currently under development at MIT and could

easily be attached to this modified panel code. The gap at the root of the semi-span foil is also not treated in the present program. Much of the work that was done to simulate the effects of the clearance gap for ducted propellers could be utilized here. Finally, treatment of the random wandering of the tip vortex may be added for more precise predictions of the tip vortex behavior.

The output of the modified panel code gives encouraging results. While there remains an error in the velocity calculation, computation of the circulation distribution and the wake geometry is validated by the experimental data. With implementation of the above features, this relatively simple code, based on fundamental principles of potential flow, could be used to predict various semi-span geometries without expending the time and money to build scale models for water tunnel testing. This code may also be used as a cross check for one of the more complex Reynolds averaged Navier-Stokes (RANS) codes which have been developed in recent years such as "DTNS3D", used at the David Taylor Model Basin [17]. The treatment given here leaves open the opportunity to advance this panel code to an even more useful and accurate predictor of tip vortex behavior.

Chapter 7

Appendix

This appendix contains plots of the standard deviations associated with the LDV velocity measurements discussed in Chapter 4.

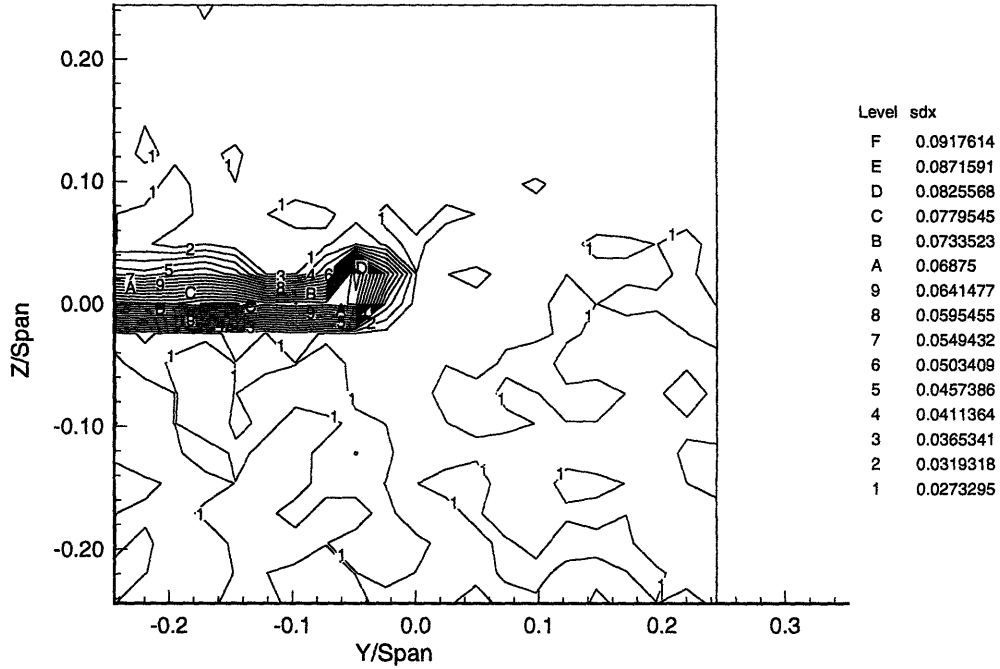


Figure 7-1: Standard deviation of streamwise velocity at $X/Span = -0.044$. Angle of attack is $+5.36$ degrees (side orientation/coarse grid).

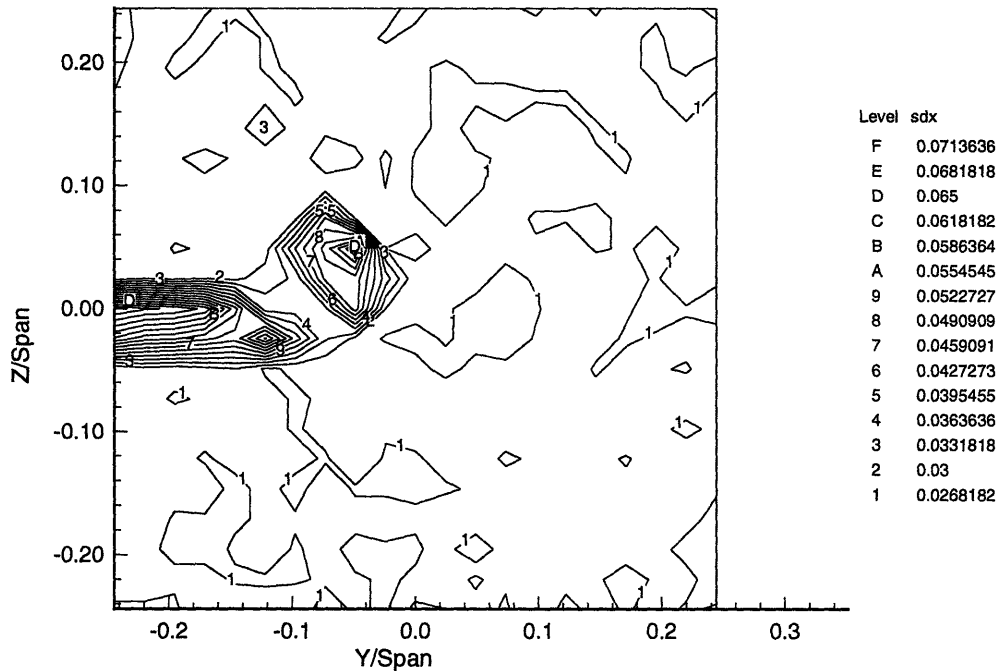


Figure 7-2: Standard deviation of streamwise velocity at $X/Span = -0.34$. Angle of attack is $+5.36$ degrees (side orientation/coarse grid).

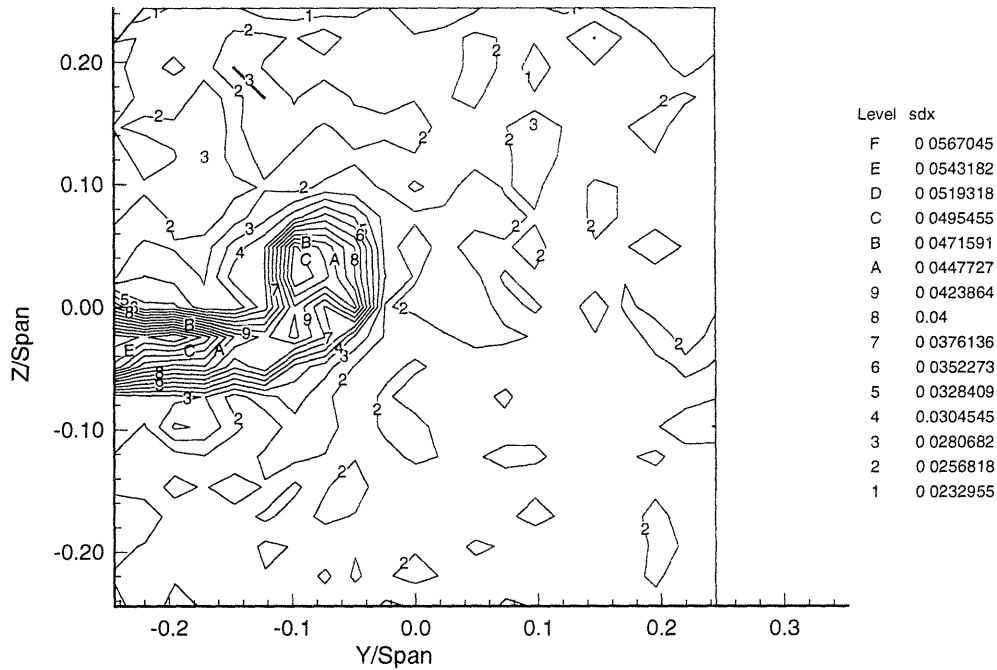


Figure 7-3: Standard deviation of streamwise velocity at $X/Span = -0.66$. Angle of attack is $+5.36$ degrees (side orientation/coarse grid).

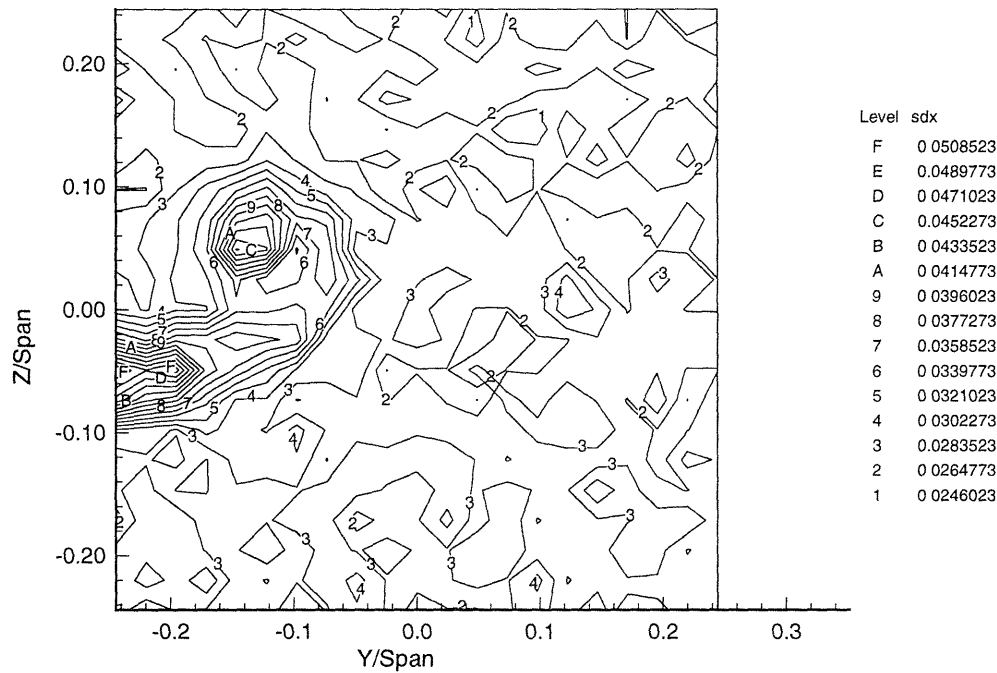


Figure 7-4: Standard deviation of streamwise velocity at $X/Span = -1.28$. Angle of attack is $+5.36$ degrees (side orientation/coarse grid).

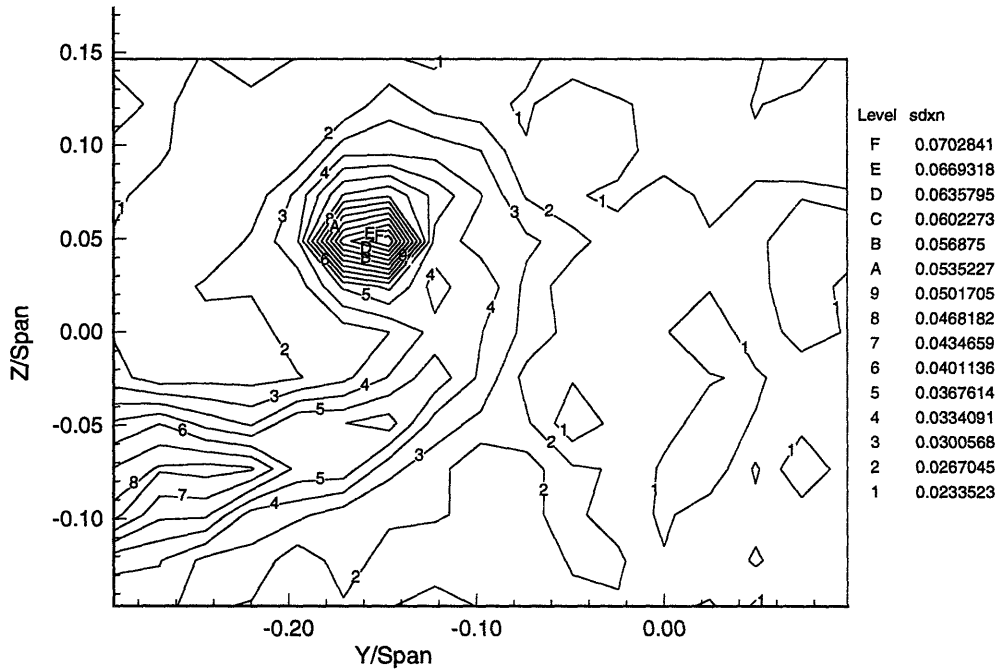


Figure 7-5: Standard deviation of streamwise velocity at $X/Span = -1.67$. Angle of attack is $+5.36$ degrees (side orientation/coarse grid).

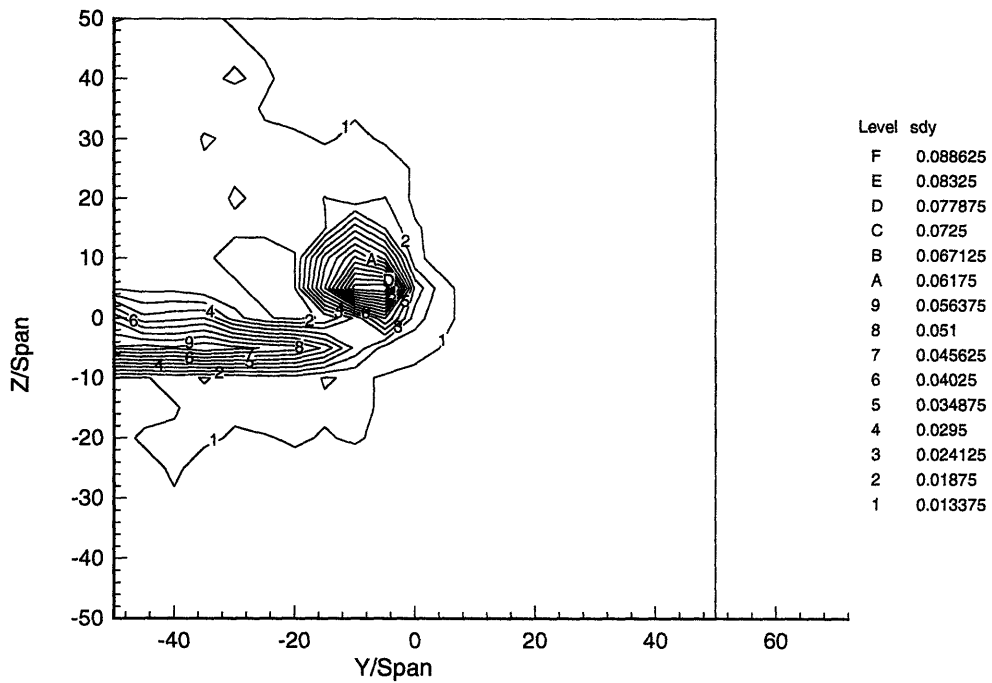


Figure 7-6: Standard deviation of spanwise velocity at $X/Span = -0.34$. Angle of attack is $+5.36$ degrees (top orientation/coarse grid).

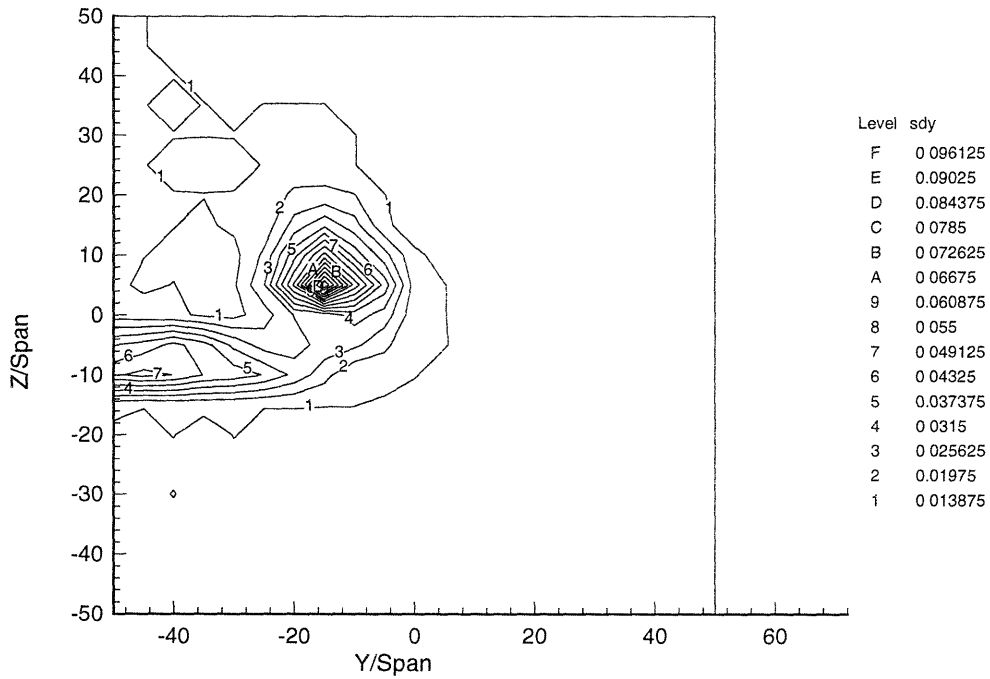


Figure 7-7: Standard deviation of spanwise velocity at $X/Span = -0.66$. Angle of attack is $+5.36$ degrees (top orientation/coarse grid).

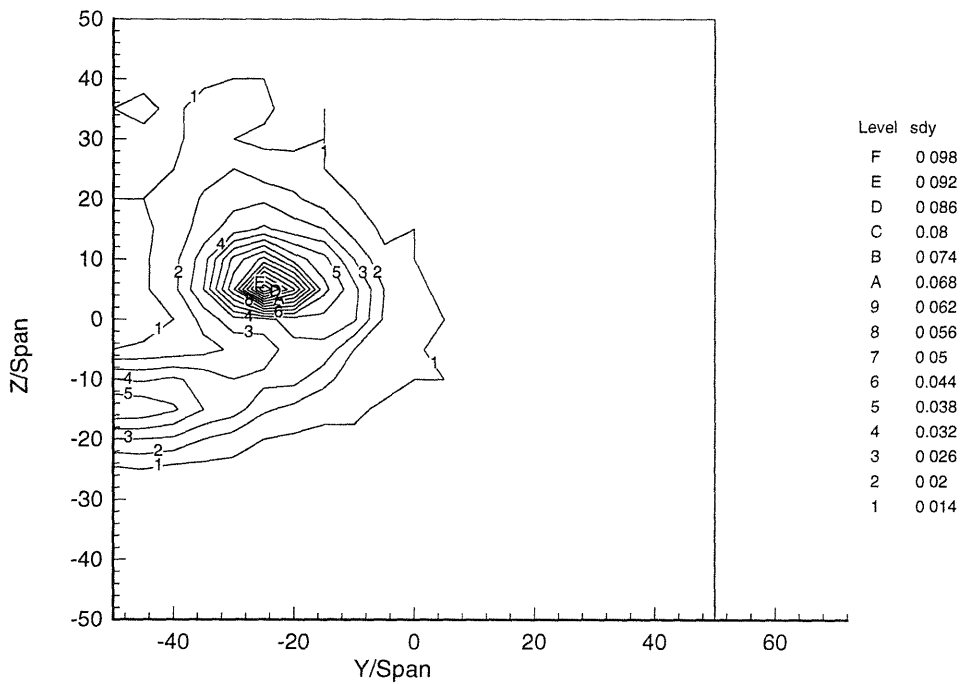


Figure 7-8: Standard deviation of spanwise velocity at $X/Span = -1.28$. Angle of attack is $+5.36$ degrees (top orientation/coarse grid).

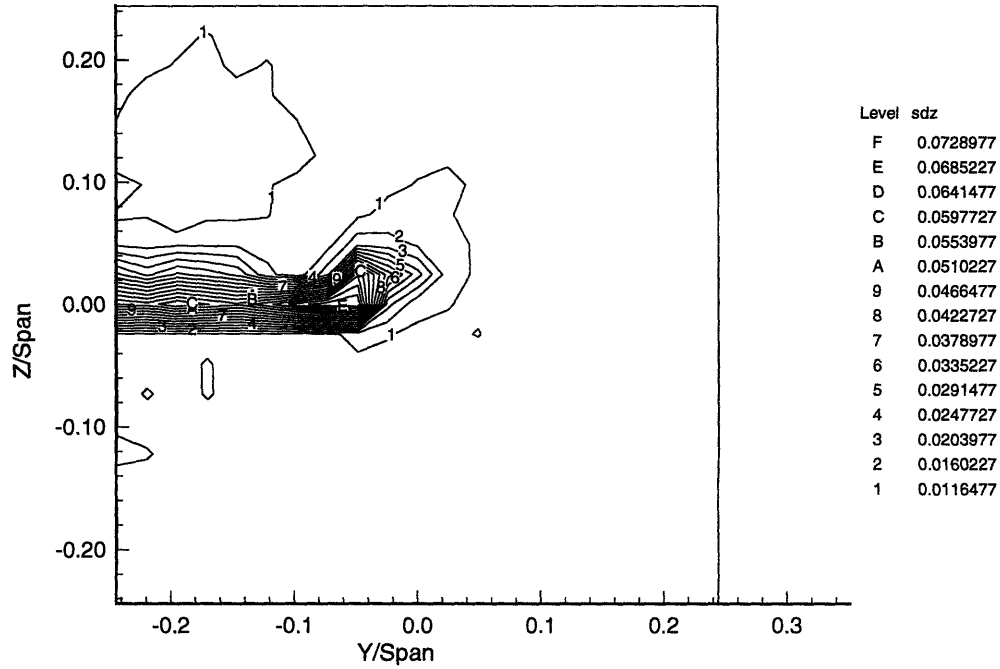


Figure 7-9: Standard deviation of vertical velocity at $X/Span = -0.044$. Angle of attack is $+5.36$ degrees (side orientation/coarse grid).

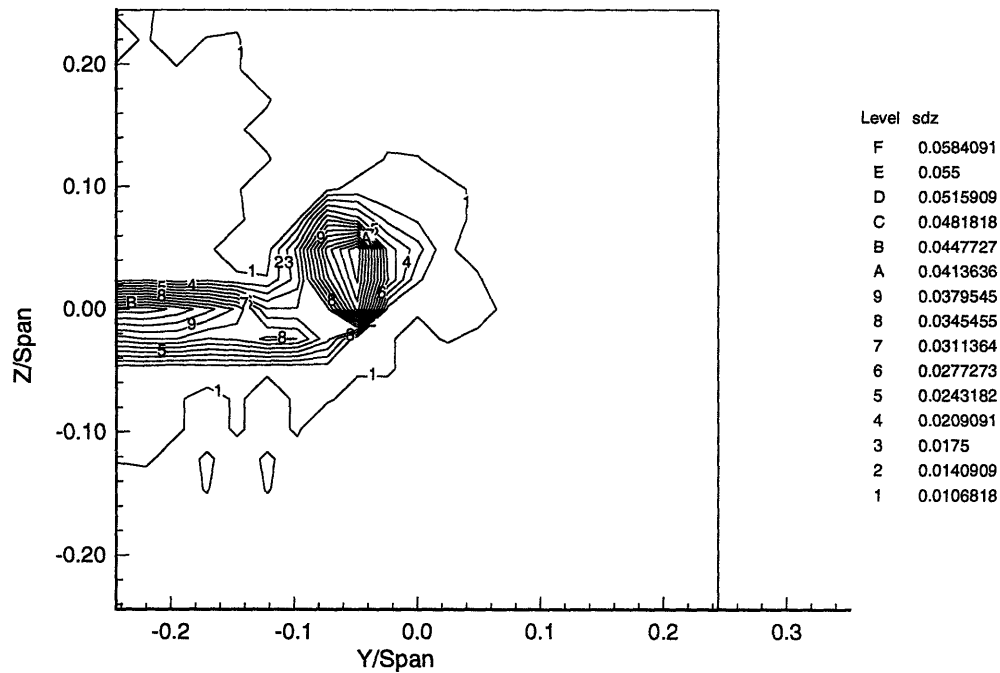


Figure 7-10: Standard deviation of vertical velocity at $X/Span = -0.34$. Angle of attack is $+5.36$ degrees (side orientation/coarse grid).

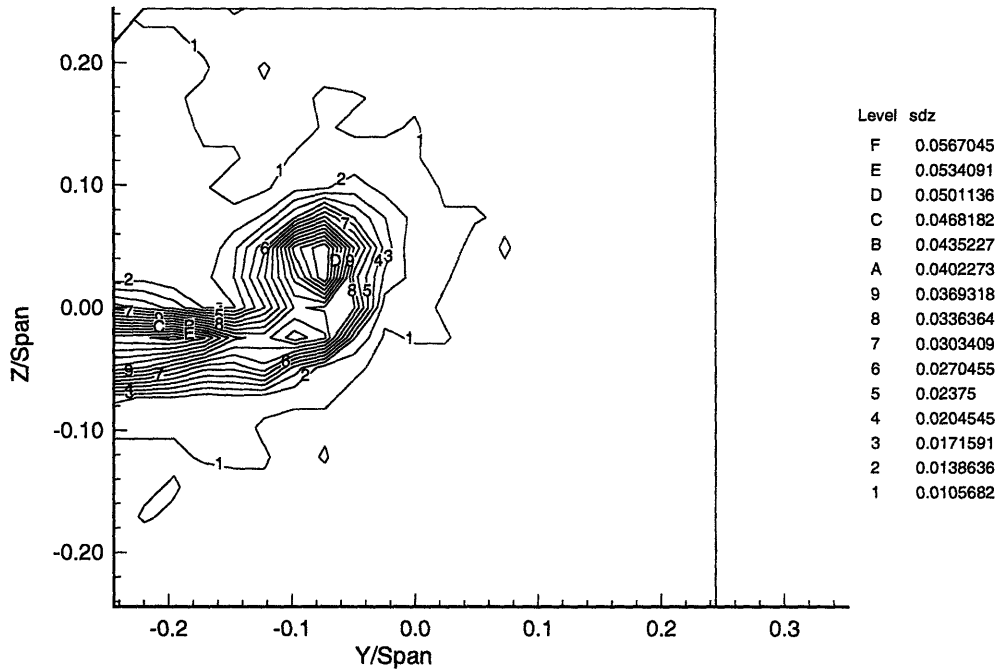


Figure 7-11: Standard deviation of vertical velocity at $X/Span = -0.66$. Angle of attack is $+5.36$ degrees (side orientation/coarse grid).

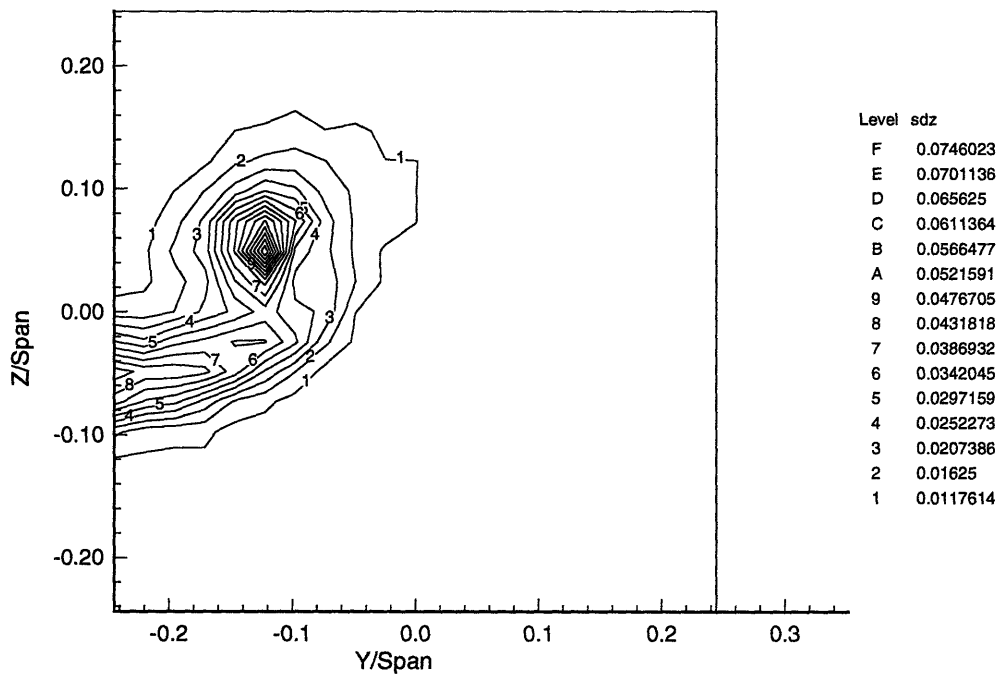


Figure 7-12: Standard deviation of vertical velocity at $X/Span = -1.28$. Angle of attack is $+5.36$ degrees (side orientation/coarse grid).

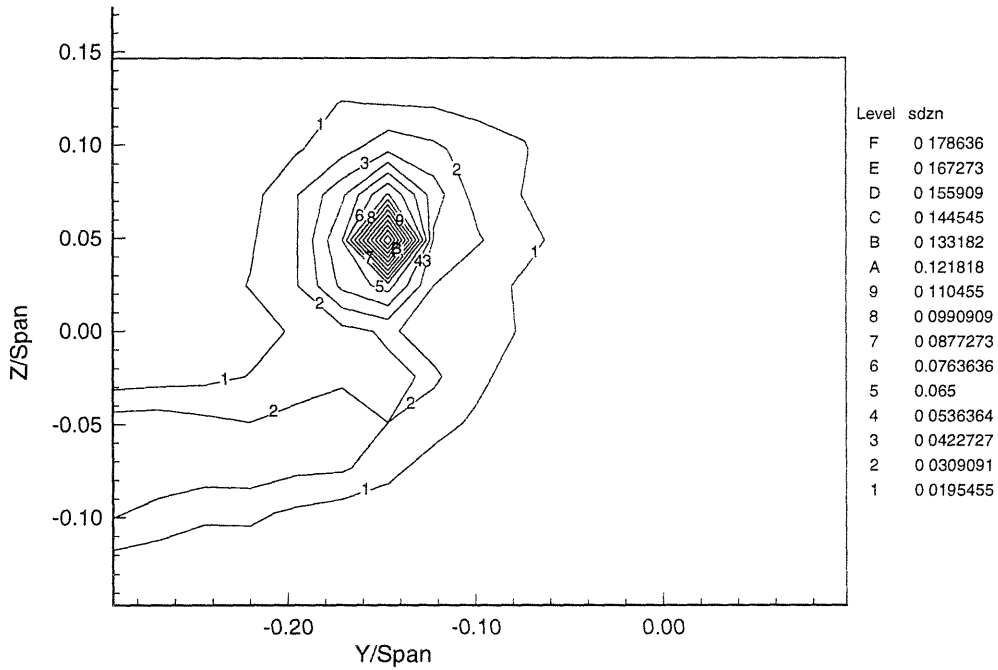


Figure 7-13: Standard deviation of vertical velocity at $X/Span = -1.67$. Angle of attack is $+5.36$ degrees (side orientation/coarse grid).

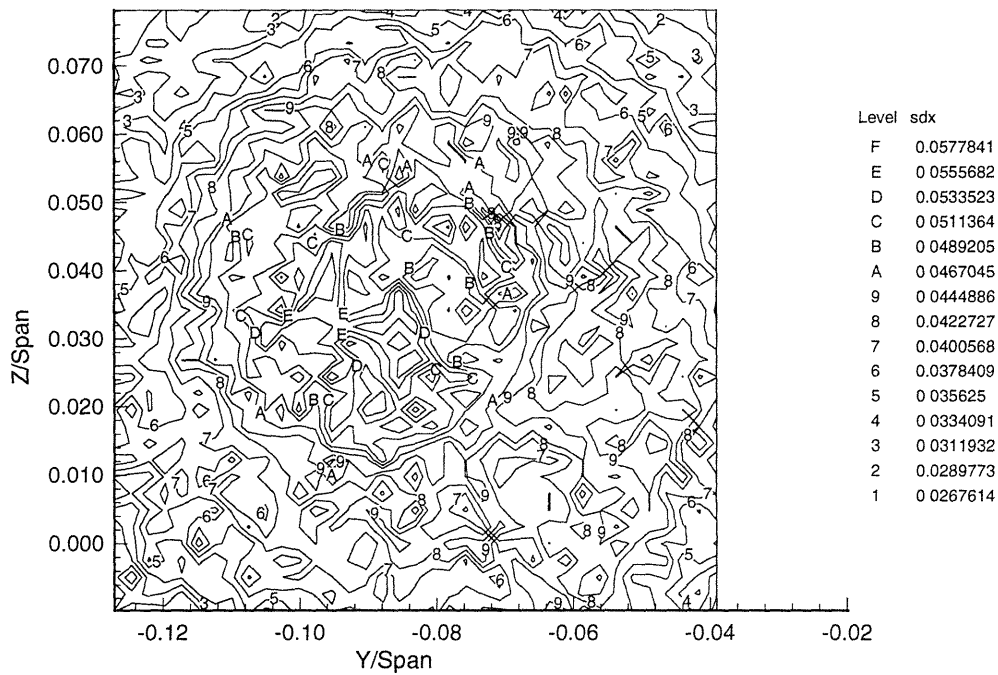


Figure 7-14: Standard deviation of streamwise velocity at $X/Span = -0.66$. Angle of attack is $+5.36$ degrees (side orientation/fine grid).

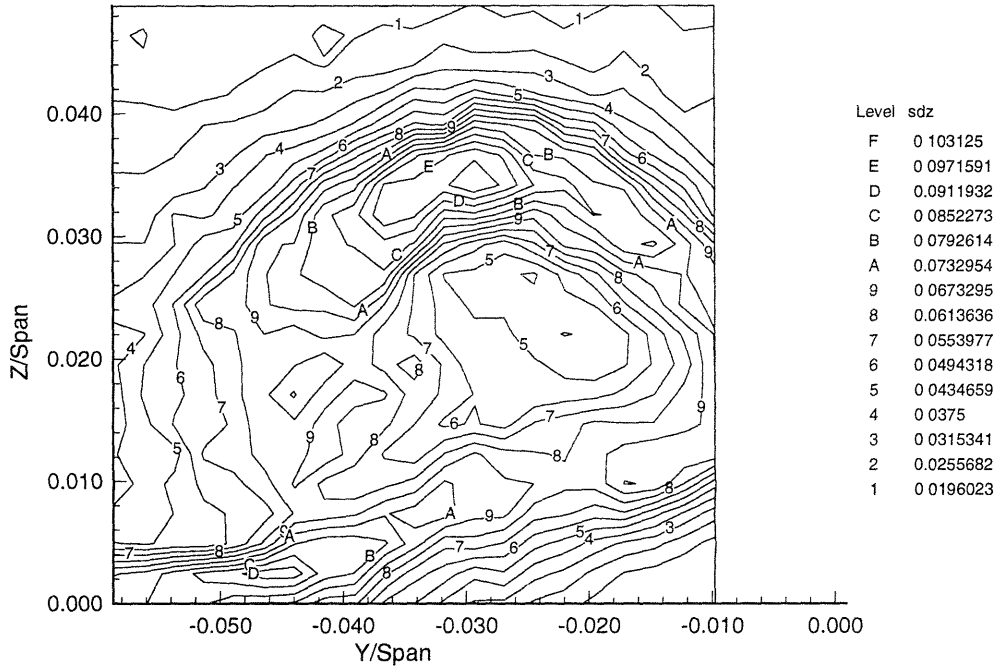


Figure 7-15: Standard deviation of vertical velocity at $X/Span = -0.044$. Angle of attack is $+5.36$ degrees (side orientation/fine grid).

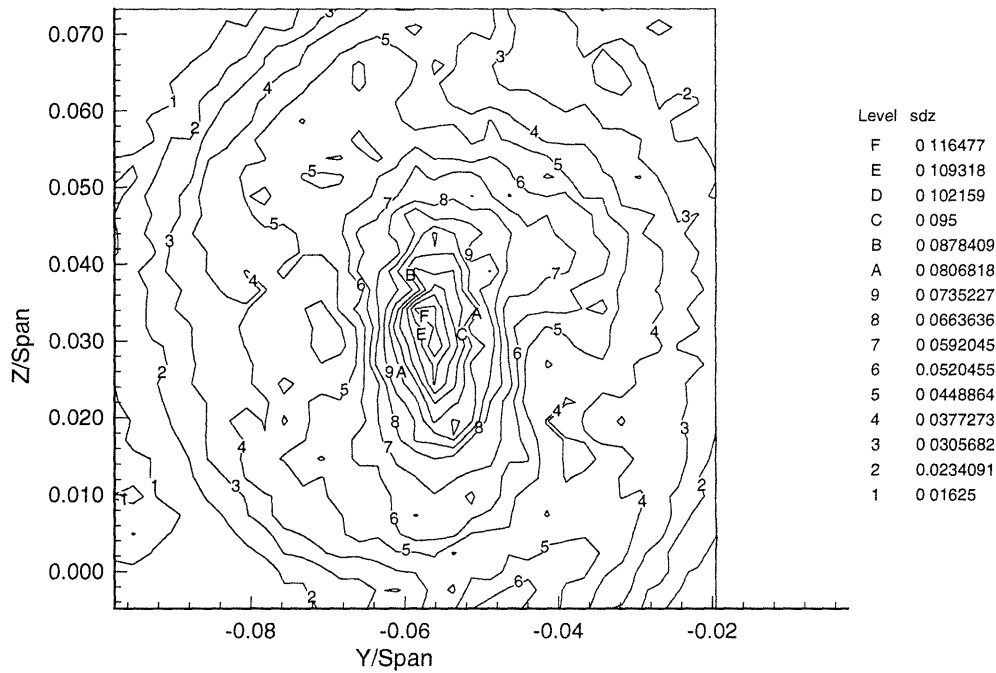


Figure 7-16: Standard deviation of vertical velocity at $X/Span = -0.34$. Angle of attack is $+5.36$ degrees (side orientation/fine grid).

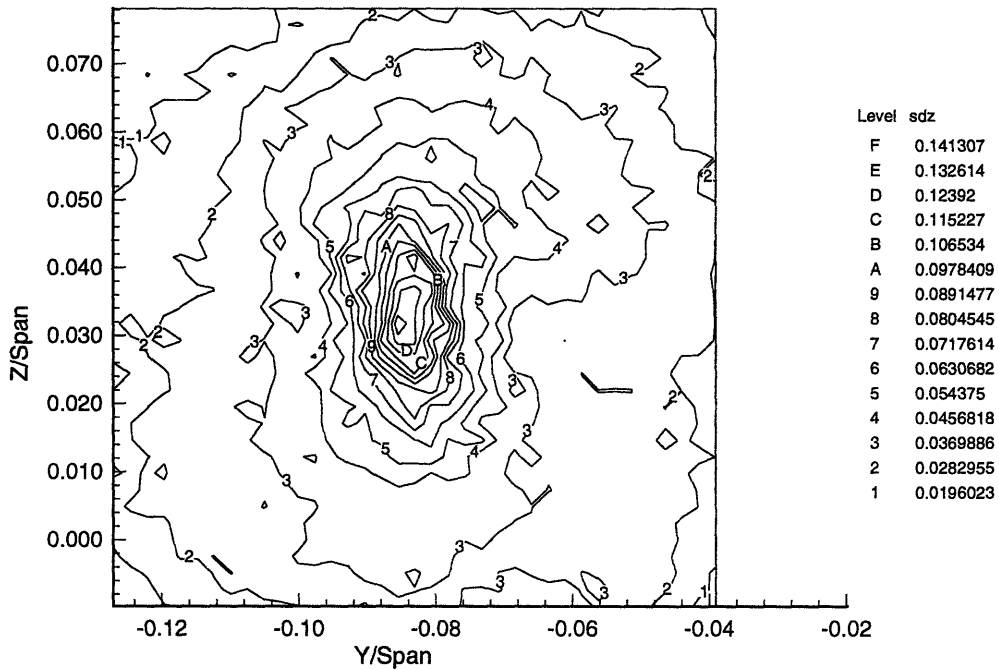


Figure 7-17: Standard deviation of vertical velocity at $X/Span = -0.66$. Angle of attack is $+5.36$ degrees (side orientation/fine grid).

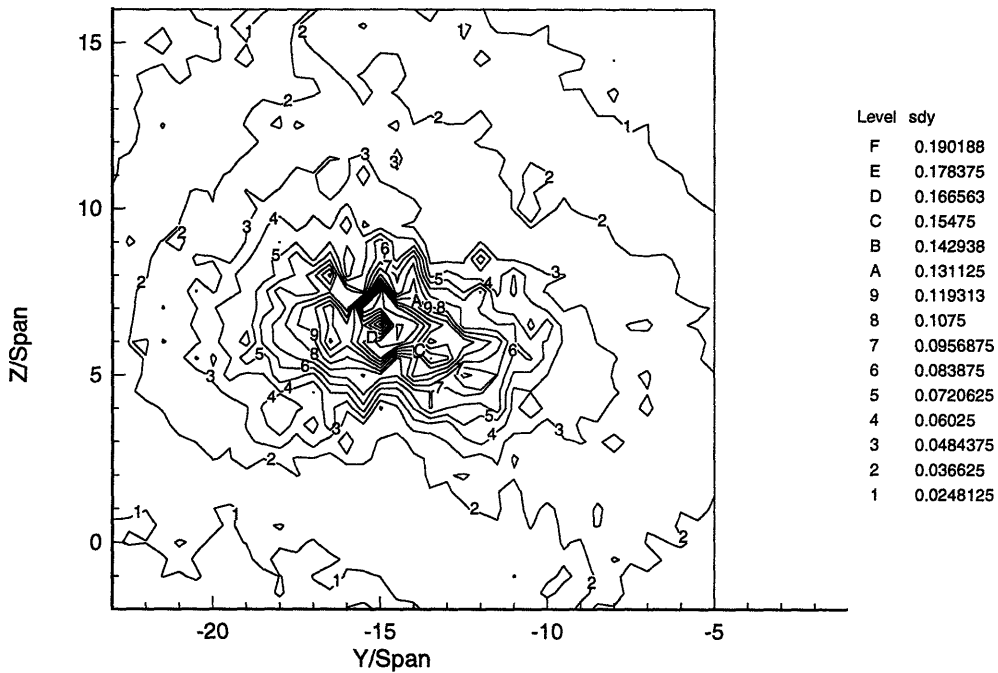


Figure 7-18: Standard deviation of spanwise velocity at $X/Span = -0.66$. Angle of attack is $+5.36$ degrees (top orientation/fine grid).

Bibliography

- [1] I. H. Abbot and A. E. Von Doenhoff. *Theory of Wing Sections*. Dover Publications, New York, 1959.
- [2] N. A. Chigier and V. R. Corsiglia. Tip vortices-velocity distributions. Technical Report TM X-62, NASA, 1971.
- [3] R. W. Clark. A new iterative matrix solution procedure for three dimensional panel methods. *AIAA 23rd Aerospace Sciences Meeting*, January 1985.
- [4] W. B. Coney. Spanwise circulation measurements about a semi-span wing. Technical Report 7785, BBN Systems and Technologies, December 1992.
- [5] D. S. Greeley and J. E. Kerwin. Numerical methods for propeller design and analysis in steady flow. *SNAME Transactions*, (90), 1982.
- [6] C. Y. Hsin. Development and analysis of panel methods for propellers in unsteady flow. Technical Report 91-1, Department of Ocean Engineering, Massachusetts Institute of Technology, January 1991.
- [7] B. Hunt. *Numerical Methods in Applied Fluid Dynamics*, chapter The Mathematical Basis and Numerical Principles of the Boundary Integral Method for Incompressible Potential Flow over 3-D Aerodynamic Configurations. Academic Press, London, 1980.
- [8] J. E. Kerwin. Hydrofoils and propellers. Lecture Notes for M.I.T. Course 13.04, February 1994.

- [9] J. E. Kerwin. The MIT hydrodynamics water tunnel - a 53rd anniversary celebration. *Marine Technology*, 31(3), July 1994.
- [10] J. E. Kerwin, S. A. Kinnas, J. T. Lee, and W. Z. Shih. A surface panel method for the hydrodynamic analysis of ducted propellers. *SNAME Transactions*, (95), 1987.
- [11] Robert Krasny. Computation of vortex sheet roll-up in the trefftz plane. *Journal of Fluid Mechanics*, 184, 1987.
- [12] Sir Horace Lamb. *Hydrodynamics*. Dover Publications, New York, sixth edition, 1932.
- [13] J. T. Lee. A potential based panel method for the analysis of marine propellers in steady flow. Technical Report 87-13, Department of Ocean Engineering, Massachusetts Institute of Technology, July 1987.
- [14] D. K. Lezius. Water tank study of the decay of trailing vortices. *AIAA Journal*, 12(8), August 1974.
- [15] J. N. Newman. Distributions of sources and normal dipoles over a quadrilateral panel. *Journal of Engineering Mathematics*, 20:113–126, 1986.
- [16] R. K. Takahashi and K. W. McAlister. Preliminary study of a wing-tip vortex using laser velocimetry. Technical Report TM 88343, NASA, January 1987.
- [17] J. G. Telste and R. M. Coleman. DTNS3D computer code simulation of tip-vortex formation: RANS code validation. Preliminary Draft of CDNSWC Technical Report, November 1994.